U.S. Department
of Transportation
**Federal Railroad
Administration**

**Office of Research,
Development and Technology
Washington, DC 20590**

Feasibility Study of Raman Piezo-Spectroscopy as a Mobile Method for Measuring Longitudinal Rail Stress

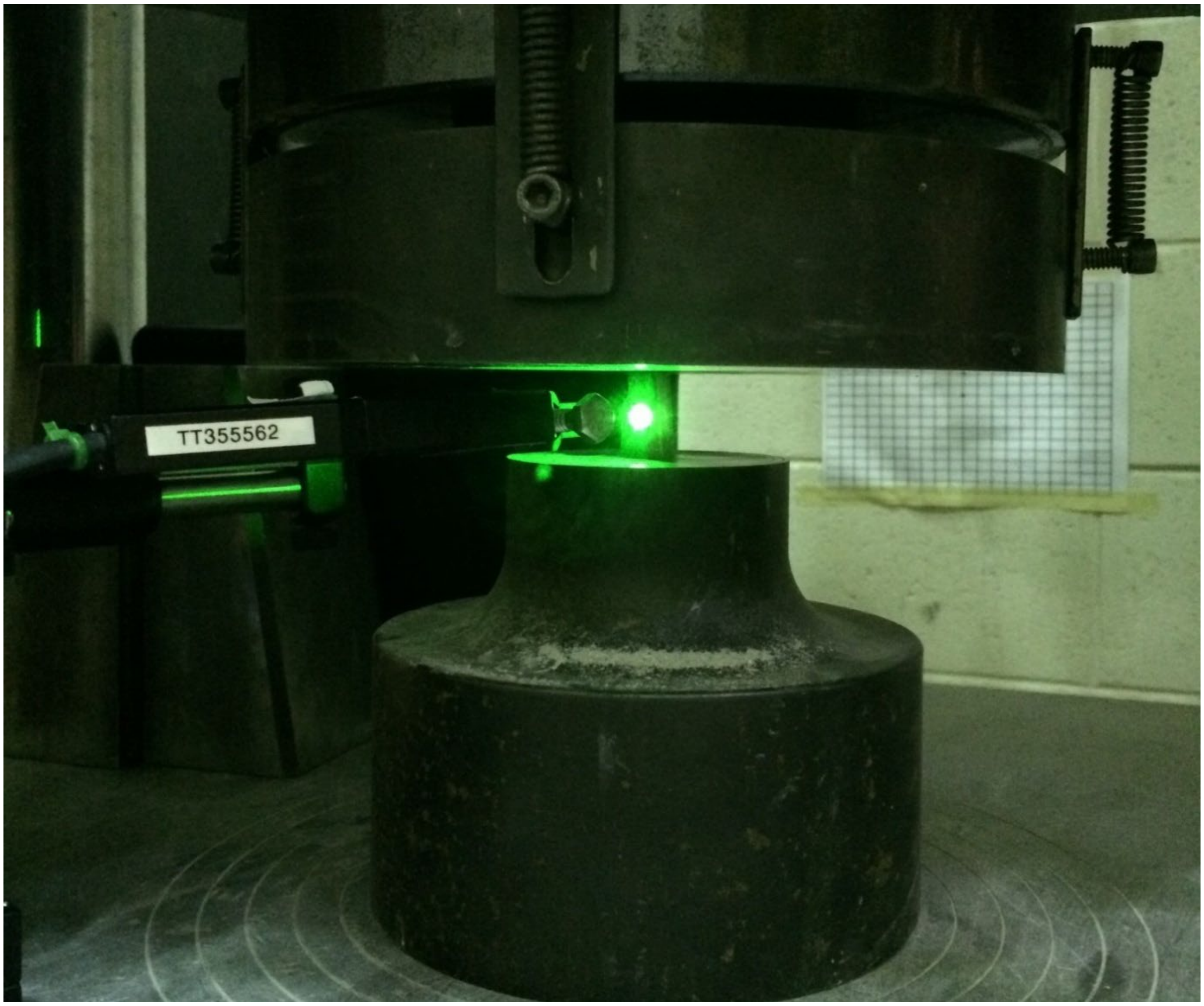

DOT/FRA/ORD-26/02

Final Report | April 2026

REPORT DOCUMENTATION PAGE

Form Approved
OMB No. 0704-0188

1. AGENCY USE ONLY (Leave blank)
3 April 2026

2. REPORT DATE
April 2026

3. REPORT TYPE AND DATES COVERED
Technical Report (March 2015–June 2016)

4. TITLE AND SUBTITLE
Feasibility Study of Raman Piezo-Spectroscopy as a Mobile Method for Measuring Longitudinal Rail Stress

5. FUNDING NUMBERS
DTFR53-15-C-00008

6. AUTHOR(S)
Hae-Bum “Andrew” Yun, and Namgyu Kim

7. PERFORMING ORGANIZATION NAME(S) AND ADDRESS(ES)
University of Central Florida
4000 Central Florida Blvd
Orlando, FL 32816-2450

8. PERFORMING ORGANIZATION REPORT NUMBER

9. SPONSORING/MONITORING AGENCY NAME(S) AND ADDRESS(ES)
U.S. Department of Transportation
Federal Railroad Administration
Office of Research, Development, and Technology
Washington, DC 20590

10. SPONSORING/MONITORING AGENCY REPORT NUMBER
DOT/FRA/ORD-26/02

11. SUPPLEMENTARY NOTES
COR: Cameron Stuart

12a. DISTRIBUTION/AVAILABILITY STATEMENT
This document is available to the public through the FRA Web site at http://www.fra.dot.gov.

12b. DISTRIBUTION CODE

13. ABSTRACT (Maximum 200 words)

The objective of this project was to investigate the feasibility of Raman and fluorescence piezo-spectroscopy as a mobile method to measure the absolute stress in rail. This study identified Raman and fluorescence-sensitive oxides on the rail surface that can be used as an *in-situ* passive sensor for absolute stress measurement. From a series of material characterization tests, we observed that different iron oxide and hydroxide layers near the rail surface are Raman-sensitive materials, including Hematite (α-Fe_2O_3), Goethite (α-FeOOH), Lepidocrocite (γ-FeOOH) and Magnetite (Fe_3O_4). In our Raman piezo-spectroscopy test we found that the Hematite can be used to measure thermal residual stress that is induced when the Hematite layer is formed on rail surface during air quenching after milling at a high temperature. However, the Hematite layer is gradually scaled off over time, and the measurement precision needed to determine a change in stress state exceed the capabilities of the equipment. Much higher resolution equipment is needed to measure small changes in rail stress. Additional experiments were conducted using Aluminum oxide (α-Al_2O_3), commonly found in thermite weld area. Our test results show that the aluminum oxide has an excellent signal-to-noise ratio to measure rail stress without additional surface treatment. Since it is well established that high contents of aluminum oxides in steel makes the thermite weld brittle, Raman and fluorescence spectrometry could be used as a non-contact quality assurance method to inspect chemical (Al_2O_3 and iron oxides) and mechanical (residual stress) conditions of exothermic welds in field.

14. SUBJECT TERMS
Iron oxide/hydroxide layer, thermite weld zone, Raman spectroscopy, fluorescence spectroscopy

15. NUMBER OF PAGES
118

16. PRICE CODE

17. SECURITY CLASSIFICATION OF REPORT
Unclassified

18. SECURITY CLASSIFICATION OF THIS PAGE
Unclassified

19. SECURITY CLASSIFICATION OF ABSTRACT
Unclassified

20. LIMITATION OF ABSTRACT

NSN 7540-01-280-5500 Standard Form 298 (Rev. 2-89)

Contents

Illustrations

Tables

Executive Summary

The Federal Railroad Administration provided funding to the University of Central Florida to investigate the feasibility of Raman and fluorescence piezo-spectroscopy (RPS/FPS) as a mobile method to measure absolute stress in rail from March 2015 to June 2016. The proposed RPS/FPS-based method eliminates the need to install ex-situ sensors on the rail surface. The ex-situ sensing approach can only measure the relative rail stress. The stress at the time of the sensor installation is assumed to be zero.

The metals present in the rail steel alloy naturally react with oxygen in the air to form hematite (α-Fe2O3), magnetite (Fe3O4), goethite (α-FeOOH) and lepidocrocite (γ-FeOOH) near the rail surface during manufacturing, construction and operation processes. In continuous welded rail (CWR), an abundant amount of aluminum oxide (α-Al2O3) is contained in welds, which is created as a byproduct of thermite welding. Therefore, this study was conducted to develop a passive in-situ stress sensor based on spectroscopic techniques using (1) iron oxide and hydroxide on rail surface, and (2) aluminum oxide in thermite weld zone in rail.

(1) Iron oxide and hydroxide layers on the surface of rail: Three rail samples manufactured in 1948, 1999, and 2012 showed iron oxides and hydroxides on rail surface in a series of material characterization tests, including scanning electron microscopy (SEM), Raman spectroscopy, X-ray diffraction spectroscopy (XRD) and energy-dispersive X-ray spectroscopy (EDS), and nano-indentation. Different iron oxides and hydroxides were observed in different colors on the rail surface. Important findings about the iron oxides and hydroxides, which were made in material characterization tests, included the following:

Gray-colored layer

- The surface of the gray-colored layer is a mixture of hematite and magnetite.
- The hematite is known to have Raman piezo-spectroscopic characteristics, which was also confirmed in our Raman piezo-spectroscopy tests.
- The layer developed in a furnace has a uniform thickness of 49 μm.
- However, the layer scales off over time, and cannot be seen on older rails.
- The elastic modulus of gray-colored layer is 107 GPa (15,519 ksi).
- The nano-hardness of gray-colored layer is 7.1 GPa (1,030 ksi), and the value is almost similar to the parent material which is rail steel.

Brown-colored layer

- The surface of the brown-colored layer is a mixture of goethite and lepidocrocite initially.
- The layer grown in uncontrolled environment, and has an irregular thickness of 43 μm.
- The brown-colored layer sometimes grows on iron oxide(s) layer.
- The top layer, however, is changed over time to a non-detectable material for Raman spectroscopy and XRD.
- The elastic modulus of brown-colored layer is 46 GPa (6,671 ksi).

In addition, Raman piezo-spectroscopy tests were conducted to measure residual stress in the iron oxides and hydroxides layers. The followings were concluded in terms of the feasibility of using iron oxides and hydroxides on rail surface:

- It was found that the hematite can be used to measure thermal residual stress that is induced when the hematite layer is formed on rail surface during air quenching after milling at a high temperature. However, the hematite layer is gradually scaled off over time, and using hematite may not be practically feasible, thus, we do not recommend using Hematite as a passive stress sensor.
- The detectability of goethite and lepidocrocite on rail surface decreased for older rail. Also, the goethite and lepidocrocite layers are not mechanically stable due to scaling off (i.e., rusting). In addition, their growth is largely dependent on environmental conditions. Thus, it is not feasible to use goethite and lepidocrocite as a passive sensor.

(2) Aluminum oxide in thermite weld: A series of fluorescence spectroscopy tests were conducted to detect aluminum oxides in thermite welds. A strong signal of aluminum oxide was observed from inside the thermite weld and on its bare surface. Two-dimensional (2D) and three-dimensional (3D) mapping tests were conducted to understand the distribution of aluminum oxide in the weld. A compression test using a hydraulic loading frame to verify that the aluminum oxide's fingerprint peaks shift as compression load increases. The key observations from the above tests are as follows:

- From 2D and 3D mapping tests, it was found that the aluminum oxides are concentrated in the heat-affected zone (HAZ) and the interface of the weld and parent rail when we measured from the rail surface, while the aluminum oxides distributed uniformly when we measure inside the rail.
- The zero-stress state was determined by measuring the fluorescence fingerprint peaks of the aluminum oxide in a fine powder form to make sure that the aluminum oxide retains no stress. The fingerprint peaks of the aluminum oxide were measured at 14405.4036 cm-1 for R1 and 14435.3748 cm-1 for R2.
- Once determining the zero-stress state, we conducted the compression test using a hydraulic loading frame. It was observed that the R1 and R2 peaks shifted to the left as the compressive force increased. The piezo-spectroscopic coefficients were calculated using a linear regression model: 3.7388 cm-1/GPa (0.025775 cm-1/ksi) for R1 and 3.2082 cm-1/GPa (0.02212 cm-1/ksi).

From the above findings, the following can be concluded in terms of the feasibility of using aluminum oxide in thermite weld:

- The aluminum oxide that is abundantly contained in weld as a byproduct of thermite welding, can be used to measure absolute stress in rail in a non-contact manner.
- Our test results show that the aluminum oxide has an excellent signal-to-noise ratio to measure rail stress without additional surface treatment.
- Since it is well established that high contents of aluminum oxides in steel makes the thermite weld brittle, Raman and fluorescence spectrometry could be used as a non-contact quality assurance method to inspect chemical (Al_2O_3 and iron oxides) and mechanical (residual stress) conditions of thermite welds in field.

- The spectrometer used in this study has the maximum resolution of 3~4 cm-1, and a commonly used curve fitting method was adopted as a post-processing technique to increase the resolution of stress measurement. Without post-processing technique, it is recommended to have 0.01 cm-1 resolution that is equivalent to 4 MPa (0.58 ksi) in stress and 1.6 °C (2.88 °F) in temperature.

1. Introduction

The Federal Railroad Administration provided funding to the University of Central Florida to investigate the feasibility of Raman and fluorescence piezo-spectroscopy (RPS/FPS) as a mobile method to measure absolute stress in rail from March 2015 to June 2016.

1.1 Background

Rail is made from low alloy steel in the form of α-Fe or ferrite containing C, Cr, Mn, Cu, Ni, V, Mo and Nb. The metals present in the rail steel alloy react with oxygen in the air to naturally form metal oxide layers near the rail surface during manufacturing and construction processes. At welded joints, iron oxide powder reacts with aluminum powder in the welding zone during thermite welding processes. Some of these oxides are chemically and mechanically stable and may be used as a natural *in-situ* stress sensor without involving ex-situ sensor installation. A stable oxide layer would have effective stress transfer from the rail substrate, which is important for an accurate stress measurement.

It is well established in literature that many of these metal oxides are sensitive with the Raman and fluorescence piezo-spectroscopy(RPS/FPS). This project seeks to identify Raman and fluorescence-sensitive oxides in the rail, which can be used as an in-situ sensor for absolute stress measurement. If successful, this project could lead to the development of a novel non-contact stress sensing technique, which requires *no* sensors, wires, external power, power cable, and additional electronic circuits. The highlights of the proposed research are shown in Figure 1.

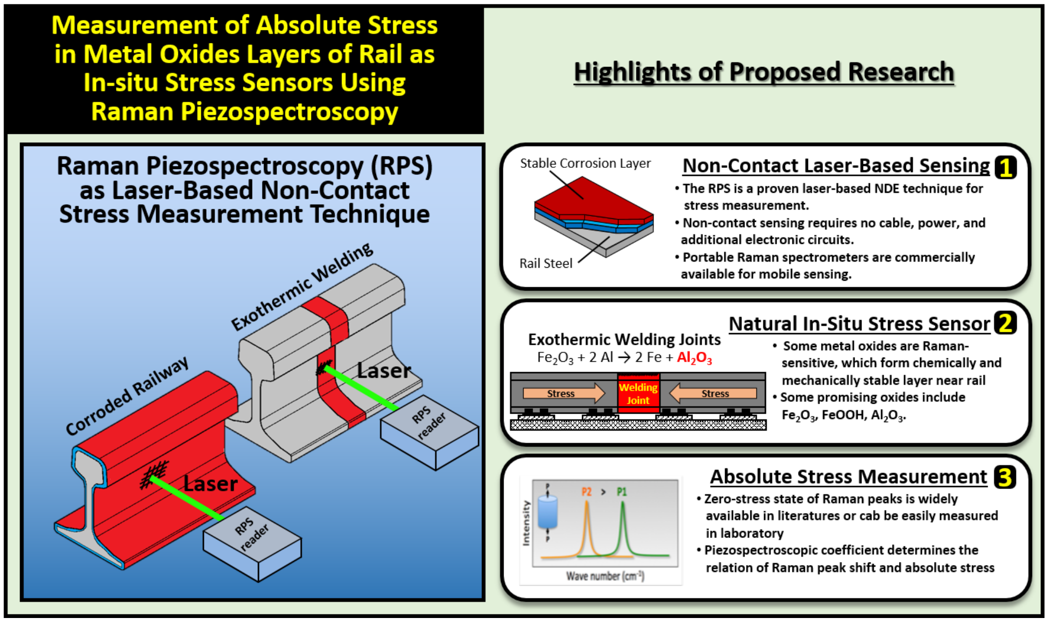

- The RPS is a proven laser-based NDE technique for stress measurement.
- Non-contact sensing requires no cable, power, and additional electronic circuits.
- Portable Raman spectrometers are commercially available for mobile sensing.

$Fe_2O_3 + 2\,Al \rightarrow 2\,Fe + Al_2O_3$

- Some metal oxides are Raman-sensitive, which form chemically and mechanically stable layer near rail
- Some promising oxides include Fe_2O_3, FeOOH, Al_2O_3.

- Zero-stress state of Raman peaks is widely available in literatures or cab be easily measured in laboratory
- Piezospectroscopic coefficient determines the relation of Raman peak shift and absolute stress

Figure 1. Highlights of the Proposed Research

1.2 Objectives

The objective of this project is to investigate the feasibility of RPS/FPS as a mobile method to measure the absolute stress in rail. The proposed RPS/FPS-based method will eliminate the need to install *ex-situ* sensors on the rail surface. The ex-situ sensing approach can only measure the relative rail stress. The stress at the time of the sensor installation is assumed to be zero. The project objective is to identify Raman and fluorescence-sensitive oxides in the rail that can be used as an in-situ passive sensor to achieve an absolute rail stress measurement.

1.3 Overall Approach

RPS/FPS is a proven non-destructive technology for stress measurement in various materials using a Raman and fluorescence spectrometer. A Raman and fluorescence spectrum may have one or more characteristic peaks, called “fingerprints.” Some metal oxides in rail have unique Raman and fluorescence peaks that are widely known, or that can be easily measured in the laboratory. When oxides are subjected to stress, the characteristic peaks shift, their frequency changes and this change can be measured. The peak shift corresponds to the proportional changes of stress. Therefore, knowing characteristic peaks at zero-stress state, one can determine the absolute stress applied to oxide layers by measuring the peak shift. This absolute stress measurement can be validated experimentally by accomplishing four major tasks, as shown in Figure 2.

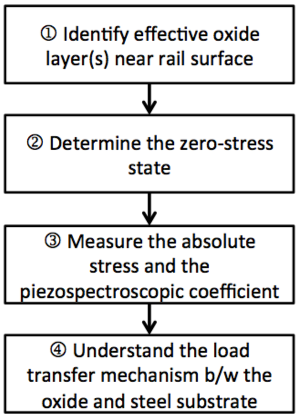

Figure 2. Research Goals to Determine the Absolute Rail Stress Using RPS/FPS

1.4 Scope

This research was designed to develop a passive in-situ stress sensor based on spectroscopic techniques for railroad rails. The target materials are:

- Iron oxide and hydroxide layers on the surface of rail
- Aluminum oxide in thermite weld zone

Included in this report are:

- Material characterization results of iron oxide/hydroxide layers on the surface of a rail
- Residual stress measurement results of the iron oxide layer on the surface of a rail using Raman piezo-spectroscopy
- 3D map of the aluminum oxide inside and outside thermite weld zone
- Stress measurement results of thermite weld zone using fluorescence piezo-spectroscopy

1.5 Organization of the Report

This report is organized into five main sections: an introduction, followed by 3 sections detailing the experimental work and, lastly, the conclusion.

2. Iron Oxides - Material Characterization of the Rail Surface

2.1 Introduction

This section describes the results of the material characterization study that begins with introducing the procedure, describing the purpose of the tests and the sample fabrication, as well as presenting the test equipment specifications. Results from individual tests will be discussed further in this section.

The goal of the material characterization study was to determine if iron oxide and hydroxide layers on the rail surface can be used as a passive in-situ stress sensor using Raman piezo-spectroscopy technology. Chemical and mechanical characterization tests were performed in this research. Microscopic imaging technology and scanning electron microscopy (SEM) were used to observe the morphology of the oxide and hydroxide layers on the rail. Spectroscopy technology, such as Raman spectroscopy, X-ray diffraction spectroscopy (XRD) and energy-dispersive X-ray spectroscopy (EDX), were applied to chemically assess the oxide and hydroxide layers on the rail. Additionally, mechanical characterization technology, using nano-indentation, was performed to analyze the mechanical properties of the oxide, hydroxide layers, and the parent material.

2.2 Rail Sample Preparation

Transportation Technology Center, Inc. (TTCI) cut three, 10-inch-long rail samples, from long rail sections (Figure 3) and delivered them to the University of Central Florida (UCF) for use in this project. Table 1 shows the types of rail samples, the three samples are all type 115 RE and have a nominal weight of 115 lb/yd. The rail samples are named 2012 rail, 1999 rail and 1948 rail based on the year of manufacture. The rail samples have different surface colors. The 2012 rail has dark gray color in addition to the red-orange-brown on the running surface. The 1999 rail only has greenish brown color, and the 1948 rail has mostly reddish brown color on the surface.

Table 1. Specification of Rail Samples

	2012 rail	**1999 rail**	**1948 rail**
Type of rail section	115RE AREMA	115RE AREMA	115RE AREMA
Manufactured year	2012	1999	1948
Surface color	Dark gray, red-orange-brown	Greenish brown	Reddish brown

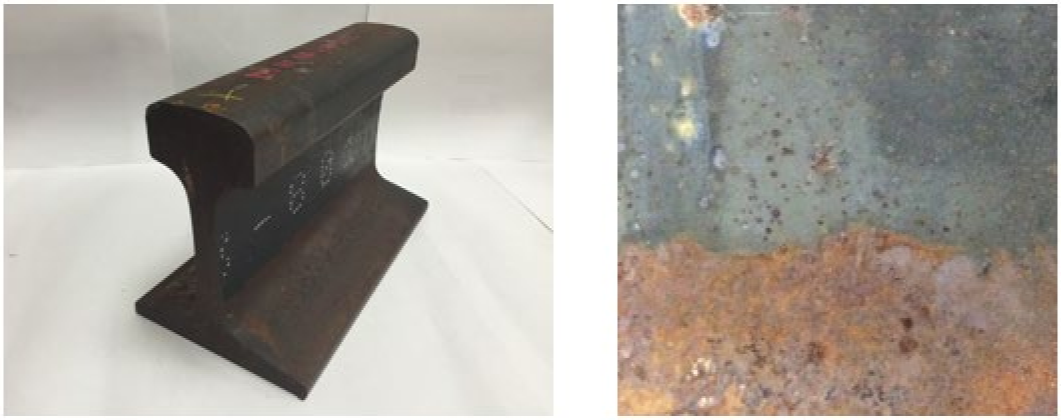

(a) 2012 rail (isometric view) (b) 2012 rail (surface image of web)

(c) 1999 rail (isometric view) (d) 1999 rail (surface image of web)

(e) 1948 rail (isometric view) (f) 1948 rail (surface image of web)

Figure 3. Photographs of 2012, 1999 and 1948 Rails

Before executing the material characterization tests, the rail samples were sectioned into different sizes using a band saw machine at UCF. Figure 4 shows a general procedure for sample preparation. For example, SEM, EDX, and nano-indentation samples were obtained by cutting the sample into roughly 0.7 inches x 0.7 inches x 0.7 inches. For XRD, the above samples were further cut to a depth of 0.1 inches because of the equipment limitation. After cutting the samples, oil and dirt were removed using ethanol or acetone, and the samples were dried completely. Optical and electron microscopy was then performed on the samples.

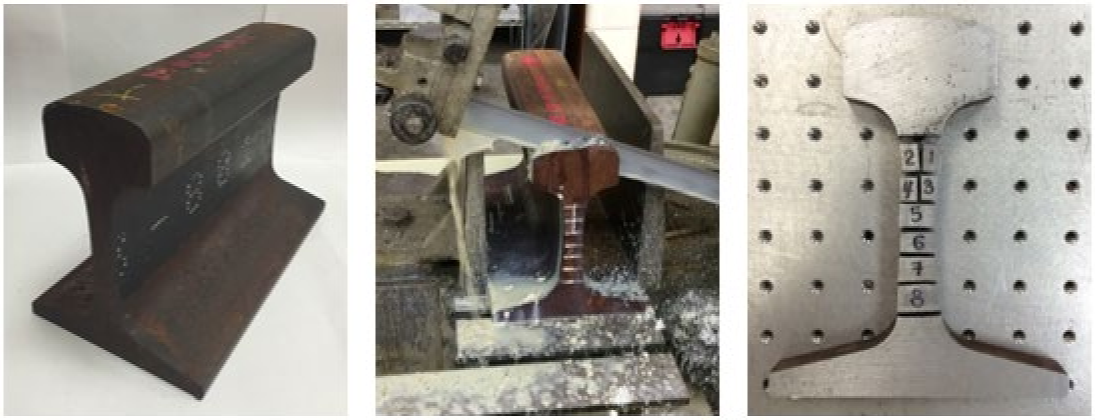

(a) Raw sample (b) Cutting rail sample (c) Cut rail

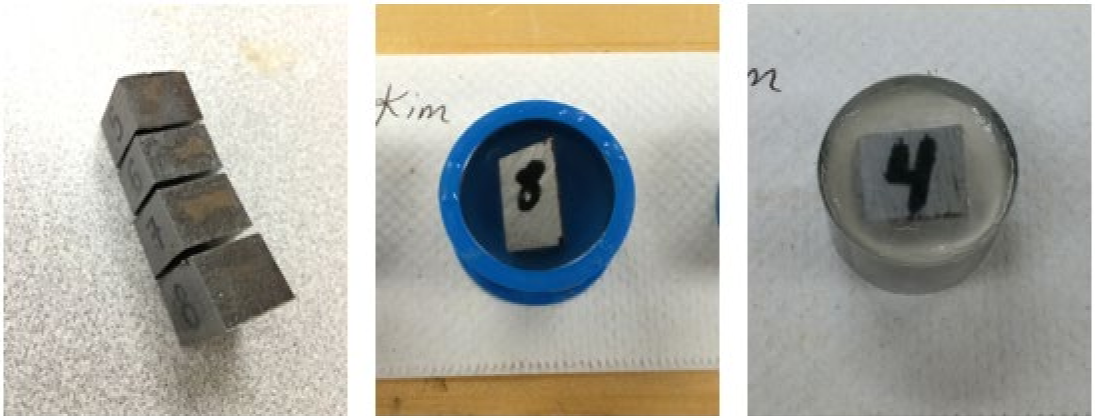

(d) Cleaning and drying (e) Epoxy molding (f) De-molding

(g) Polishing (h) Prepared sample

Figure 4. Sample Preparation for Material Characterization Tests

2.3 Experimental Work

The following sections document the experimental procedure.

2.3.1 Experimental Design

Experiment 1 compared the chemical and mechanical features of the gray and brown colors on the 2012 rail.

Aging tests were simultaneously performed with the brown-colored layers on the three rails, which were manufactured in 2012, 1999 and 1948. The experimental plan consisted of observing the change in the rail's chemical and mechanical features based on aging during Experiment #2. The rails were tested under the same conditions. The experimental setups are shown in Figure 5 and Table 2.

Table 2. Experimental Design

Name	Variable	Constant	Sample
Experiment # 1	Type of material (type of color)	Time	1-a. **Gray-colored** layer on 2012 rail 1-b. **Brown-colored** layer on 2012 rail
Experiment # 2	Time (aging test)	Type of material (type of color)	2-a. Brown-colored layer on **2012 rail** 2-b. Brown-colored layer on **1999 rail** 2-c. Brown-colored layer on **1948 rail**

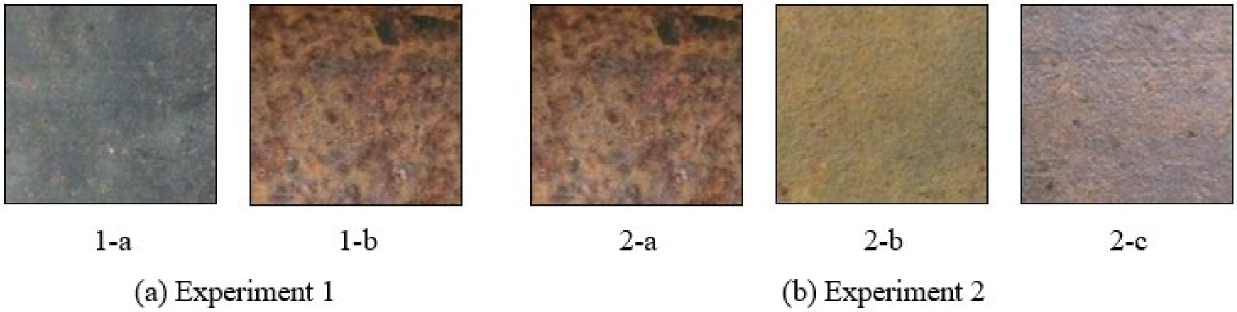

(a) Experiment 1

(b) Experiment 2

Figure 5. Experimental Designation

2.3.2 Experimental Procedure

The test procedure is shown in Figure 6. Several chemical and mechanical characterization techniques were used to determine whether iron oxide and hydroxide layers on the rail could be used as a passive in-situ stress sensor based on Raman piezo-spectroscopy technology. SEM, Raman spectroscopy, XRD, EDX and nano-indentation tests were performed.

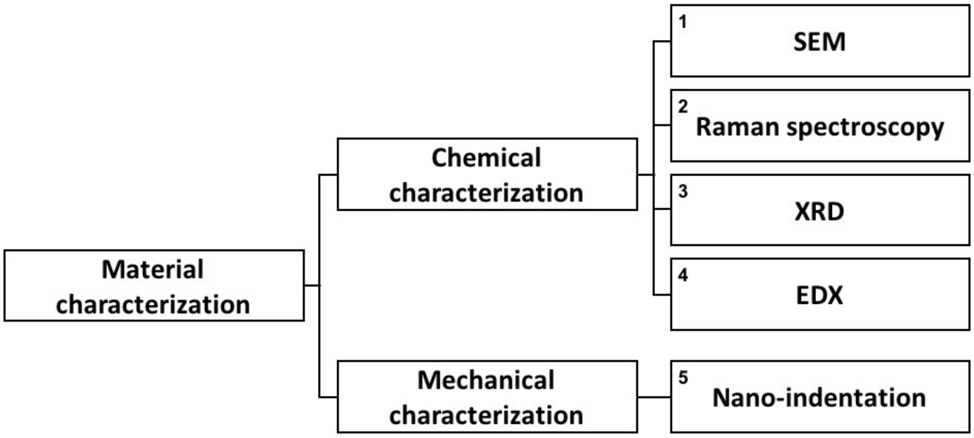

Figure 6. Material Characterization Procedure

2.3.3 Scanning Electron Microscopy

SEM was employed to observe the morphology of the oxide and hydroxide layers on the rail. SEM was used to assess the surface roughness/quality, and to measure the thickness of oxide and hydroxide layers on the rail surface. SEM was also used to assess the quality of bonding and interface states between oxide/hydroxide layers and the rail substrate.

The JEOL JSM-6480 SEM, shown in Figure 7, was used to obtain electron images of the samples. The system is a combination of SEM and EDX techniques. Figure 7 shows, (a) electron gun for producing a source of high energy electrons, (b) polished sample, (c) 3d motor stage for adjusting the location and tilting the angle of the sample, (d) X-ray detector for converting X-ray energy into a voltage signal. The measurement function of the system is shown in Table 3.

To have clear images of the surface and cross-section of iron oxide and hydroxide layers, accelerating voltage of 20 kV to 30 kV and magnification of 22X to 700X were used. Magnification of 700X was especially applied to measure the accurate thickness of the oxide and hydroxide layers on the rail. After having cross-sectional SEM images, the images were analyzed by using morphological image processing and edge detection algorithms to measure the thickness of iron oxide and hydroxide layers.

Table 3. Measurement Function of JEOL JSM-6480 SEM

Item	Specification
Magnification	15X to 300,000X
Image	Secondary electron image (SEI), Back scattered electron image (BSE)
Resolution	30 nm (SEI), 50nm (BSE)
Accelerating Voltage	0.3 to 30 kV
Specimen size	150 mm diameter maximum

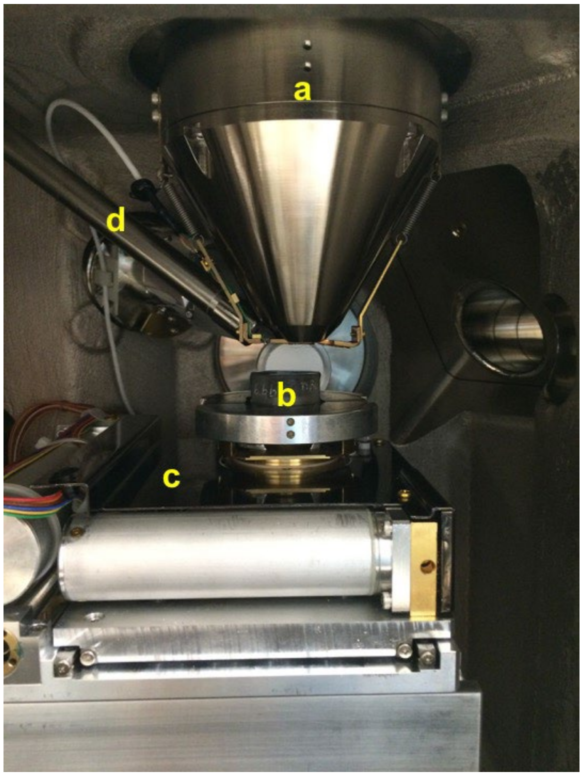

Figure 7. SEM/EDX System at UCF
(a) Electron Gun; (b) Sample; (c) 3d Motor Stage; (d) X-Ray Detector

2.3.4 Raman Spectroscopy

Raman spectroscopy is a vibrational/rotational spectroscopic technique to characterize molecules by observing the vibrational and rotational modes in a system. Raman spectroscopy was used to characterize the chemical compounds of the oxide and hydroxide layers on the rail. The reference Raman spectra were first collected by using powdered iron oxide and hydroxide. The Raman spectra were then collected from the surface and cross-section of iron and hydroxide layers on the rail. After obtaining the spectra, they were compared with the reference Raman spectra of iron oxide and hydroxide.

Two different Raman spectroscopy systems were employed. First, the Renishaw RM 1000b Micro-Raman spectrometer, a bench-top system with a 514.5 nm laser was used to characterize the iron oxide and hydroxide layers on the rail surface. Figure 8 shows four parts of the system: (a) CCD camera for adjusting the focal length, target location and taking microscopic pictures, (b) microscope, (c) laser generator for vibrating the target material, (d) spectrometer for collecting Raman spectrum. The measurement function of the system is shown in Table 4. To obtain distinguishable Raman spectra of iron oxide and hydroxide layers a 514.5 nm argon ion laser was used as the excitation source, and a magnification of 50X was utilized to observe the samples through a microscope. An integration time of 60 to 120 seconds and accumulation of 1 to 2 times were also used for obtaining high-intensity Raman spectra. The parameters were selected by considering the peak intensities. Optical images gathered using the microscope and CCD camera.

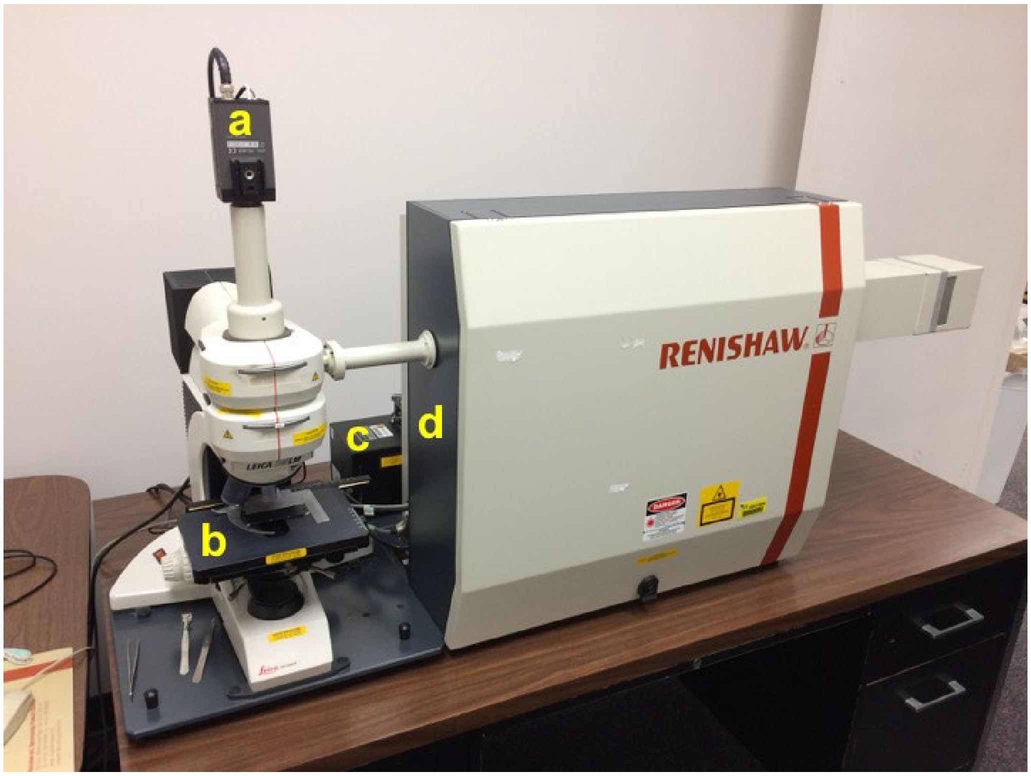

Figure 8. Bench-Top Raman Spectroscopy System at UCF (a) CCD Camera; (b) Microscope; (c) 514 nm Laser (Green Laser); (d) Raman Spectrometer

Table 4. Measurement Function of Renishaw RM 1000B Micro-Raman Spectrometer

Item	Specification
Excitation source	514.5 nm argon ion laser, 100 mW output power(Max.)
Microscope	Leica microscope (x5, x20 and x50 objectives)
Grating	1,800 line/mm

The second system is the Ocean Optics QE Pro. It is portable and was used with a 785 nm laser. Figure 9 shows the different parts of the system as in: (a) commercial software for collecting Raman spectra and adjusting experimental parameters; (b) spectrometer; (c) laser generator and controller; (d) Raman probe for carrying the laser signal to the target from the generator and bringing the scattered signal back to the spectrometer. The measurement function of the system is shown in Table 5. To obtain a correct Raman spectra with the portable system, a 785-nm multimode diode laser was used as an excitation source. The integration time of 10 seconds and accumulation of 1 to 6 times were utilized for obtaining Raman spectra. The parameters were selected by considering the peak intensities similar to the experiment with the bench-top system. Those two spectrometers were calibrated using the Raman peak at 520 cm^{-1} of a clean Si wafer.

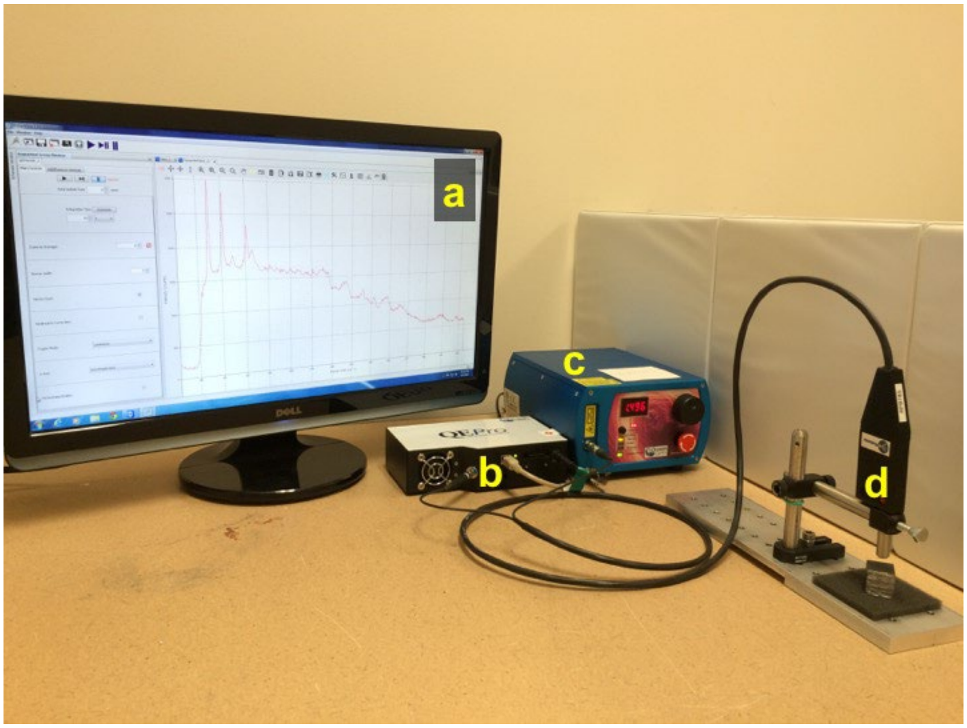

Figure 9. Portable Raman Spectroscopy System at UCF (a) Spectrometer Control Software; (b) Spectrometer; (c) 785 nm Laser (Red Laser); (d) Optic Cable and Probe

Table 5. Measurement Function of Ocean Optics QE Portable-Raman Spectrometer

Item	Specification
Excitation source	785 nm multimode diode laser, 499 mW output power(Max.)
Probe	Fiber length: 1.5 m, Working distance: 7.5 mm
Grating	1,200 line/mm

2.3.5 X-Ray Diffraction Spectroscopy

XRD was used to identify the molecular structures in oxide/hydroxide layers on the rail and verify the results of Raman spectroscopic test.

The PANalytical Empyrean, shown in Figure 10, was used to obtain an XRD pattern of the samples. The XRD instrument was configured for basic XRD, and can determine the crystal structure and lattice parameters of crystalline materials. Figure 10 shows the three parts of the system, (a) X-ray tube for producing an X-ray source, (b) sample holder, (c) detector that can be used as a point, line and area detector. The measurement function of the system is shown in Table 6.

To obtain XRD patterns of iron oxide and hydroxide layers on the rail, copper was utilized as an anode material. The tests used a generator voltage of 45 kV and a tube current of 40 Ma. After obtaining XRD patterns, they were compared with the reference XRD patterns from literature.

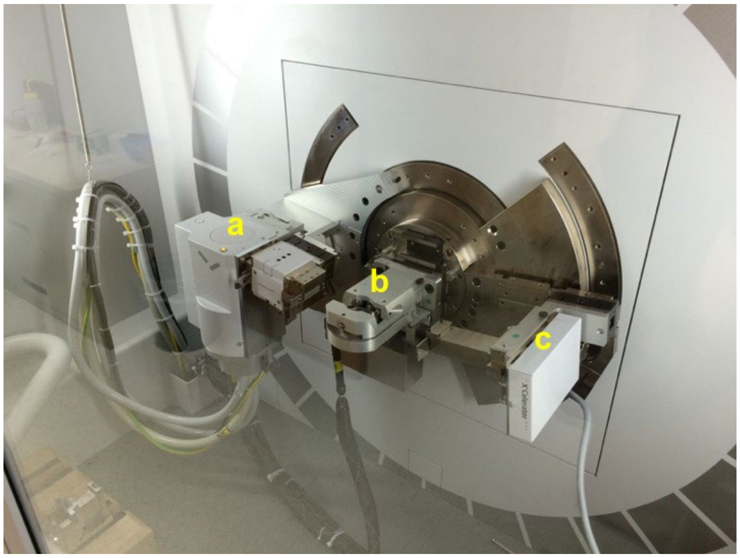

Figure 10. XRD System at UCF (a) X-Ray Tube; (b) Sample Holder; (c) Detector

Table 6. Measurement Function of PANalytical Empyrean

Item	Specification
X-ray source	1.8 kW copper X-ray tube
Goniometer	240 mm radius, maximum usable range $-111° < 2\theta < 168°$

2.3.6 Energy-Dispersive X-Ray Spectroscopy

EDX was used to perform quantitative analysis of atoms in oxide/hydroxide layers on the rail. The weight percentages of Fe, O, and C ions measured in the oxide and hydroxide layer were compared with the molecular mass percentages of pure iron oxide and hydroxides.

JEOL JSM-6480 SEM is a combination of SEM and EDX, and was simultaneously used to measure the weight/atomic percentages of atoms in oxide layers and obtain the electron images. The specifications of the system and the experimental parameters are like those used during the SEM test.

2.3.7 Nano-Indentation

Nano-indentation was used to measure the mechanical properties of the oxide and hydroxide layers on the rail.

The HYSITRON TI Premier, as shown in Figure 11, was used to obtain elastic modulus and hardness of the samples. Figure 11 shows three parts of the system which were in a chamber to isolate vibrational noise, where (a) is nano-indenter, (b) is a microscope of 10X magnification, (c) is 3d motor stage for adjusting the location of the sample. The measurement function of the system is shown in Table 7.

To calculate the elastic modulus and hardness accurately, the load-displacement curve, as shown in Figure 12, must be precisely measured. A force of 8,000 μN and 3,000 μN were applied to the oxide and hydroxide layers respectively. After calculating the elastic modulus and hardness, the results are compared with the mechanical properties of pure oxide and hydroxides.

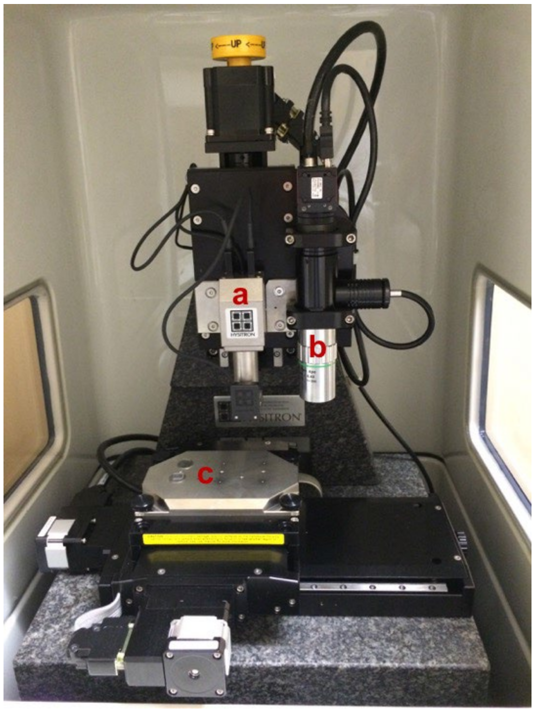

Figure 11. Nano-Indentation System at UCF (a) Nano-Indenter; (b) Microscope; (c) 2d Motor Stage

Table 7. Measurement Function of HYSITRON TI Premier

Item	Specification
Normal load range	70 nN to 10 mN
Displacement range	2 A to 5μm
Magnification	10X

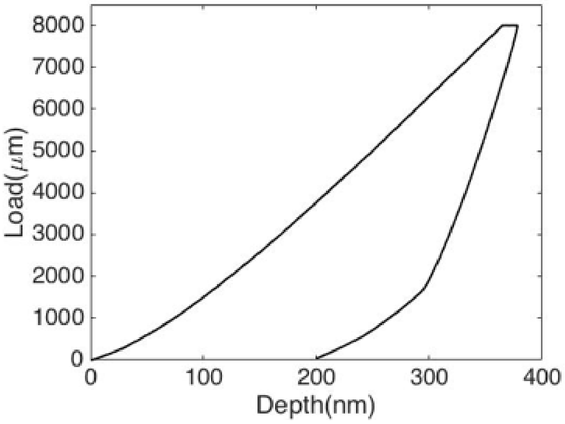

Figure 12. An example of Load-Displacement (Depth) Curve

2.4 Experimental Results

This section documents the results of the experimental work.

2.4.1 *Scanning Electron Microscopy*

The surface roughness of iron oxide and hydroxide layers were observed with a magnification range of 20X to 30X. The cross-sectional images were surveyed with a 700X magnification to look at the uniformity of and measure the thickness of the oxide and hydroxide layers. The thickness of the respective layers were calculated automatically by using morphological structuring elements. When the quality of SEM images was not sufficient to calculate the thickness using the automation algorithm, the thicknesses of three different locations were measured in pixels and then averaged. When there was no iron oxide/hydroxide on the surface, or the layers were scaled off, the parts were excluded from the calculation of the average thickness of the iron oxide/hydroxide layers. Cracks in these layers were also investigated for checking the relative hardness and stiffness of the layers. The experimental procedure is described in Figure 13.

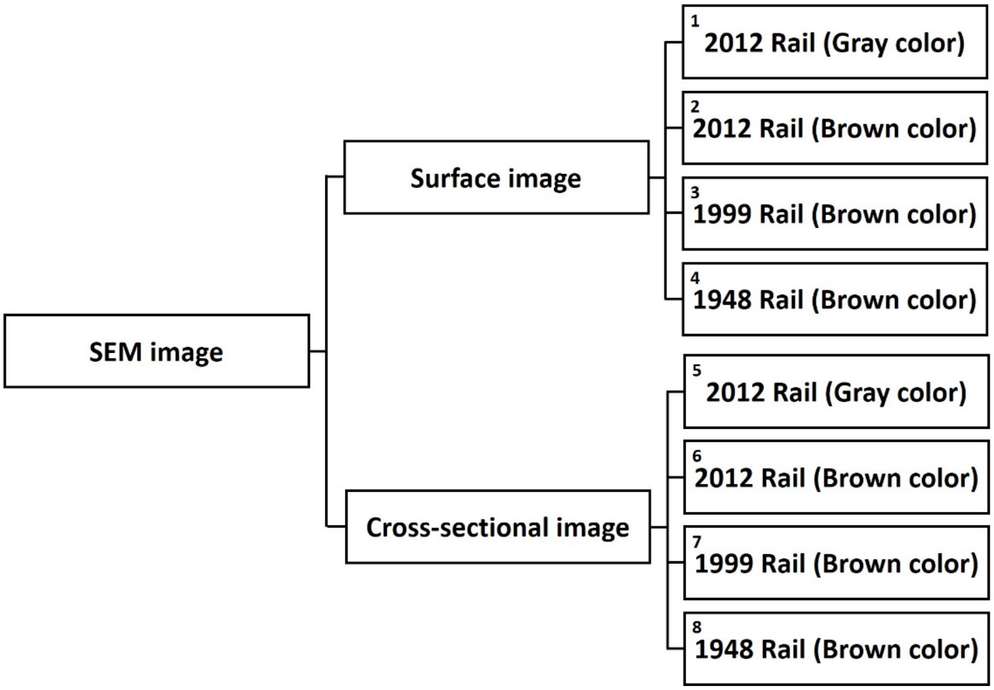

Figure 13. The Experimental Procedure of SEM

2.4.1.1 *Surface Image Results*

Surface images of gray-colored layers on the 2012 rail were obtained using SEM. Two different magnifications, 22X and 400X, with scale bars are shown in Figure 14.

The gray-colored layer had a mostly smooth rail surface, as shown in Figure 14(a) and (b). However, some parts were scaled off mechanically, as shown in Figure 14(c). An in-plane compressive residual stress which was thermally induced in the furnace to a gray-colored layer on the 2012 rail is characterized by vertical wrinkles on the surface. However, additional mechanical experiments are needed to estimate the stress.

In the case of brown-colored layers, which developed in the service condition on the 2012 rail, the smoothness of the surface is relatively rough than the gray-colored layer. Moreover, scaled off layers were found in abundance, when compared to the gray-colored layer as shown in Figure 15.

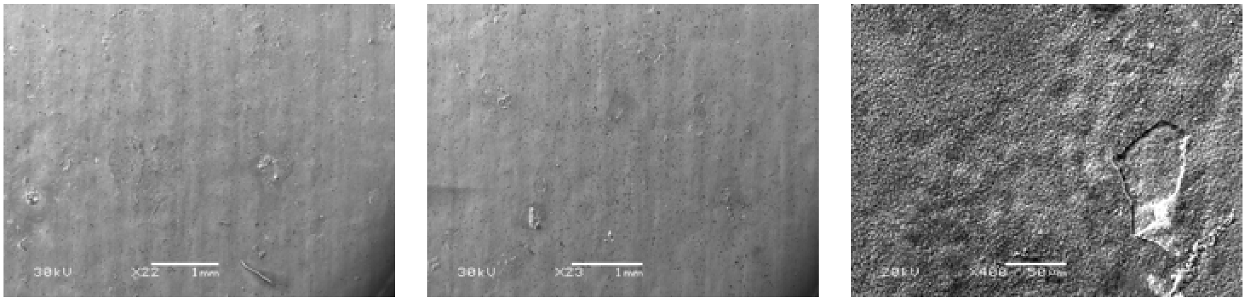

(a) Location 1 (x22, 30kV) (b) Location 2 (x23, 30kV) (c) Location 3 (x400, 20kV)

Figure 14. SEM Surface Images for the Gray-Colored Layer on 2012 rail

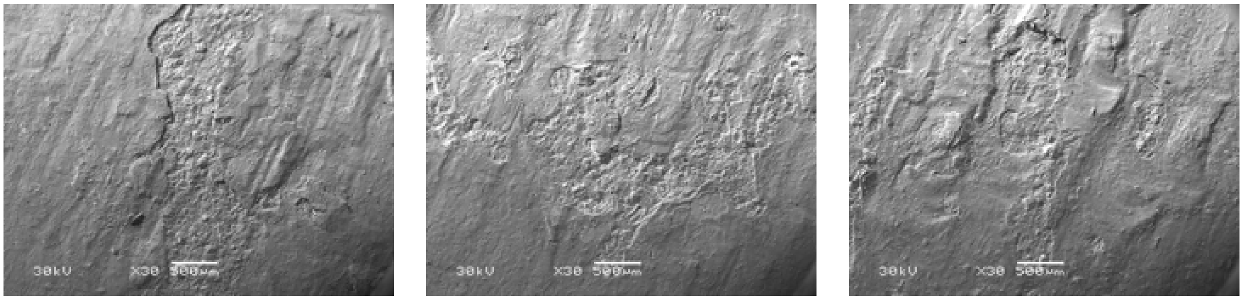

(a) Location 1 (x30, 30kV) (b) Location 2 (x30, 30kV) (c) Location 3 (x30, 30kV)

Figure 15. SEM Surface Images for the Brown-Colored Layer on 2012 Rail

The surface SEM images of brown-colored layers of rail from 1948 and 1999 are shown in Figure 16 and Figure 17. The brown-colored layers of rail from 1948 and 1999 and are relatively rough in comparison to the gray-colored layer on the 2012 rail. These brown layers develop in the uncontrolled service environment, while the gray layers seen in the 2012 sample are the result of the controlled manufacturing process. Residual stress in the brown-colored layers can not be presumed with the SEM images.

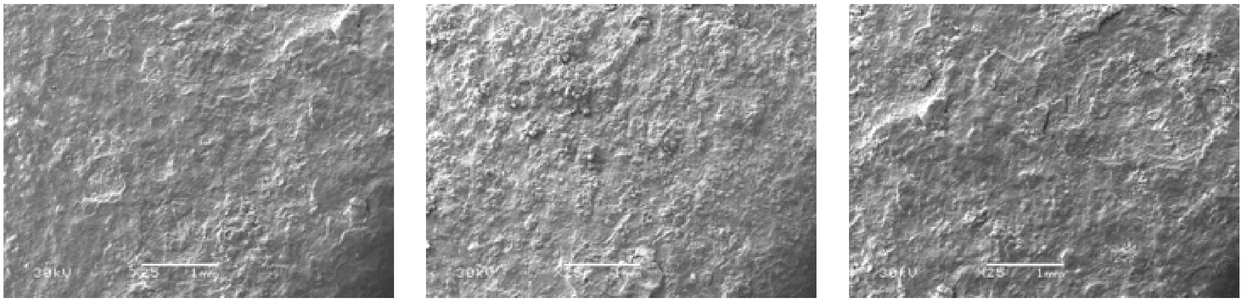

(a) Location 1 (x25, 30kV) (b) Location 2 (x25, 30kV) (c) Location 3 (x25, 30kV)

Figure 16. SEM Surface Images for the Brown-Colored Layer on 1999 Rail

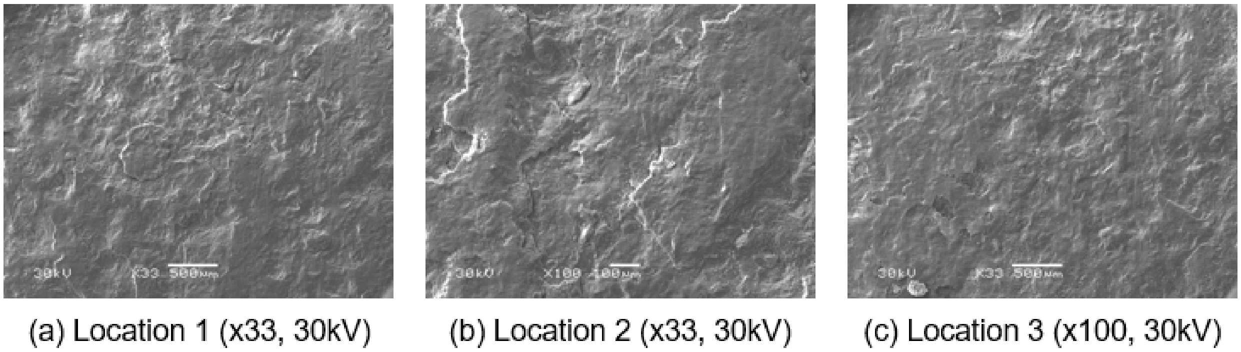

(a) Location 1 (x33, 30kV) (b) Location 2 (x33, 30kV) (c) Location 3 (x100, 30kV)

Figure 17. SEM Surface Images for the Brown-Colored Layer on 1948 Rail

2.4.1.2 Cross-Section Analysis

Cross-sectional SEM images of gray-colored layers on the 2012 rail were obtained by using SEM with the magnifications of 700X and an accelerating voltage of 30kV as shown in Figure 18. The electron images consist of three layers. The top layer is the epoxy mold, which helps the polishing process, and the middle layer is the gray-colored layer. The bottom layer is then parent material—rail steel.

The gray-colored layer thicknesses are uniform (49 µm). This oxide layer is a result of the rail manufacturing process. Some parts were scaled mechanically off as shown in Figure 18. The exfoliates, however, occurred before molding and polishing the samples. The result can be inferred from the absence of crevice between the epoxy mold layer and gray-colored layer. If the exfoliates occur after polishing, the sample would have cracks in the layer or a gap between the epoxy mold layer and the gray-colored layer.

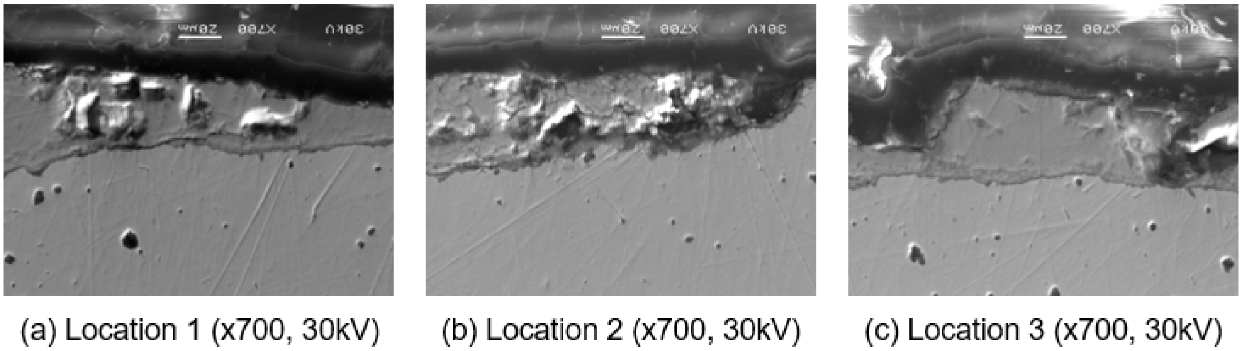

(a) Location 1 (x700, 30kV) (b) Location 2 (x700, 30kV) (c) Location 3 (x700, 30kV)

Figure 18. SEM Cross Section Images for Gray-Colored Layer on 2012 Rail

Cross-sectional SEM images of brown-colored layers on the 2012 rail were obtained by using SEM with the magnifications of 700X and an accelerating voltage of 20kV as shown in Figure 19. The electron images consist of three layers which are the epoxy mold, the brown-colored layer and the parent material respectively.

The images show a non-uniform thickness of 25 µm. The thickness of the brown-colored layer is thinner than the gray-colored layer as most of the brown-colored layer had been scaled off from the parent material.

The exfoliates occurred in the polishing process. The result can be inferred from the existence of crevice between the epoxy mold layer and the brown-colored layer. Based on the above results, an inference can be made that the hardness of brown-colored layer is relatively lower than gray-colored layer since the polishing was perfomred under the same condition. In order to get an estimation, additional mechanical experiments, such as nano-indentation test, are required.

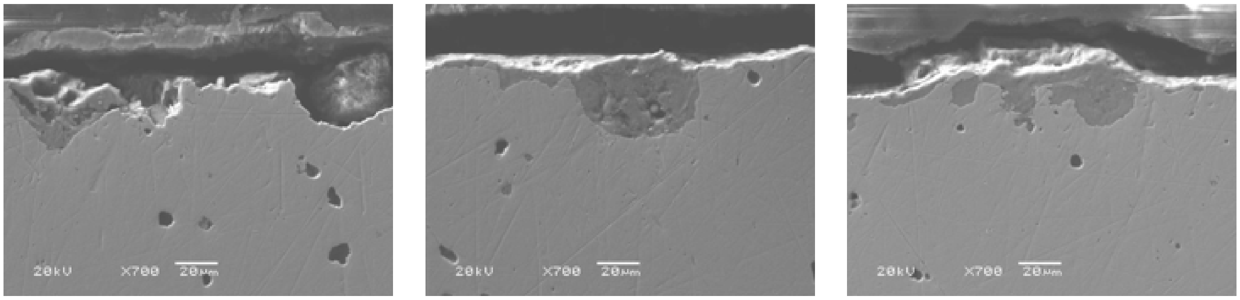

(a) Location 1 (x700, 20kV) (b) Location 2 (x700, 20kV) (c) Location 3 (x700, 20kV)

Figure 19. SEM Cross Section Images for the Brown-Colored Layer on 2012 Rail

Cross-sectional SEM images of the brown-colored layers on the 1999 rail were obtained by using SEM with a magnifications of 700X and an accelerating voltage of 30kV as shown in Figure 20. The obtained electron images consist of three layers which are the epoxy mold, the brown-colored layer and the parent material respectively.

The electron images of the brown-colored layer show a non-uniform thickness of approximately 53 µm. The brown-colored layer on the 1999 rail is more uniform than the brown-colored layer on the 2012 rail as the 1999 rail is more stablized. Severe cracks are detected in the brown-colored layer. Based on the detected severe cracks, it can be inferred that the hardness of the brown-colored layer on the 1999 rail is relatively lower than the gray-colored layer as polishing was performed under the same condition.

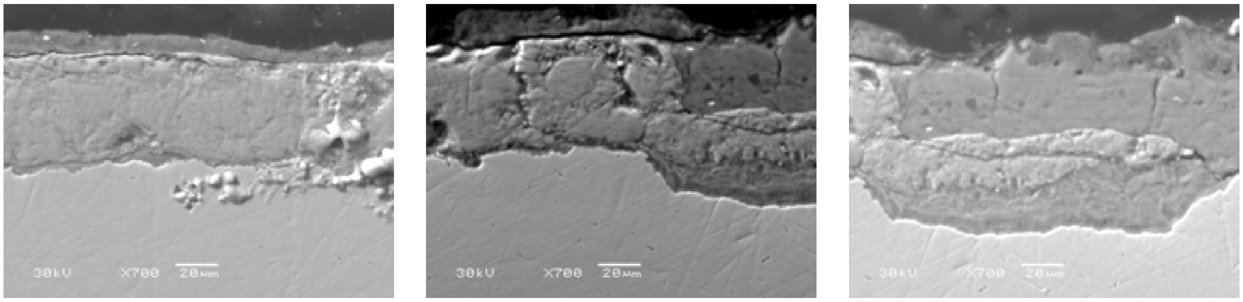

(a) Location 1 (x700, 30kV) (b) Location 2 (x700, 30kV) (c) Location 3 (x700, 30kV)

Figure 20. SEM Cross Section Images for Brown-Colored Layer on 1999 Rail

Cross-sectional SEM images of the brown-colored layers on the 1948 rail were obtained using SEM with a magnification of 700X and an accelerating voltage of 30kV as shown in Figure 21. The electron images consist of three layers which are the epoxy mold, the brown-colored layer and the parent material.

The brown-colored layers have non-uniform thickness, averaging 50 µm. The brown-colored layer on the 1948 rail is more uniform than the brown-colored layer on the 2012 rail as the layer is stabilizing over time. Moreover, some severe cracks were detected in the layer.

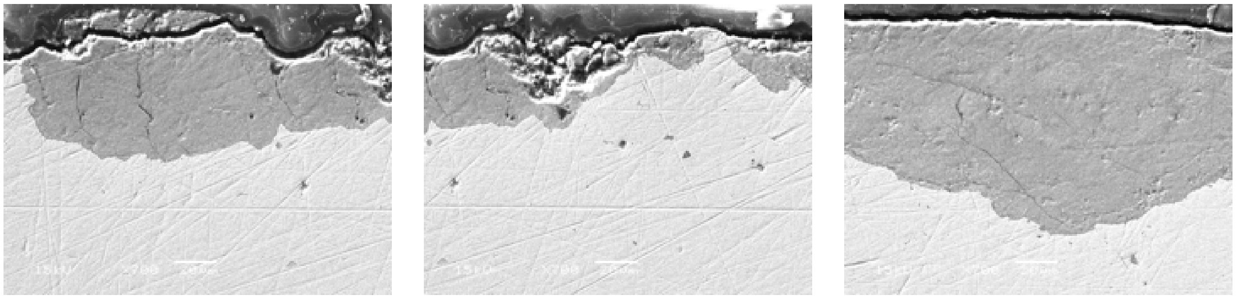

(a) Location 1 (x700, 30kV) (b) Location 2 (x700, 30kV) (c) Location 3 (x700, 30kV)

Figure 21. SEM Cross Section Images for Brown-Colored Layer on 1948 Rail

2.4.1.3 Summary of SEM Results

SEM was used to observe the morphology of the iron oxides/hydroxides layers on the rail. The thicknesses of the iron oxides/hydroxides were measured using a morphological element method and edge detection algorithm. In addition, the relative surface roughness and quality were determined using SEM.

Morphology

The gray-colored oxide layer on the rail is similar to hot rolled carbon steels and is generally known as mill scale iron oxides. The mill scale mostly consists of Magnetite (Fe3O4) and Hematite (α-Fe2O3). Hematite forms on the outer layer as it requires more oxygen than Magnetite to form, and it is a very thin layer [3]. The brown-colored oxide layers are mostly iron hydroxides and consist of Goethite (α-FeOOH), Lepidocrocite (ɣ-FeOOH) and Magnetite (Fe3O4) [1].

Figure 22 and Table 8 show the measured thicknesses and standard deviation of the iron oxides/hydroxides on the rail surface. Table 9 shows the morphological features of each layer. The gray-colored layer is composed of a mixture of Magnetite and Hematite, on the 2012 rail has a uniform thickness of 49 µm and smooth surface. On the other hand, the brown-colored layer on the 2012 rail has a non-uniform thickness of 25.2 µm and forms the rough surface as shown in the Figure 22(a). The reason why the average thickness of the brown-colored layer being thinner than the gray-colored layer is that the brown-colored layer on the 2012 rail started to form just after 1–2 years under uncontrolled environments when the gray-colored layer was scaled off. Unlike the brown-colored layer, the gray-colored layer is formed in the furnace with controlled temperature and humidity.

The thicknesses of brown-colored layer on the 2012, 1999 and 1948 rails are 25.2, 53.3 and 49.7 µm respectively as shown in Figure 22(b). All the layers have rough surfaces and non-uniform thicknesses. The thicknesses of the brown-colored layer on the 1999 and 1948 rails are similar. The layer on the 2012 rail is however noticeably thinner than the others because of its exfoliation.

Mechanical Features

All the rail samples were polished using an identical procedure. By comparing the iron oxides and hydroxides layer cracks after the polishing process, a relative comparison of the layer hardness is possible. The gray-colored layer on the 2012 rail has no cracks or exfoliation. The brown-colored layer on the 2012 rail has severe cracks and exfoliation. Therefore, the hardness of brown-colored layer is relatively low compared to the gray-colored layer. Other mechanical experiments, such as nano-indentation test, are required to quantify these results.

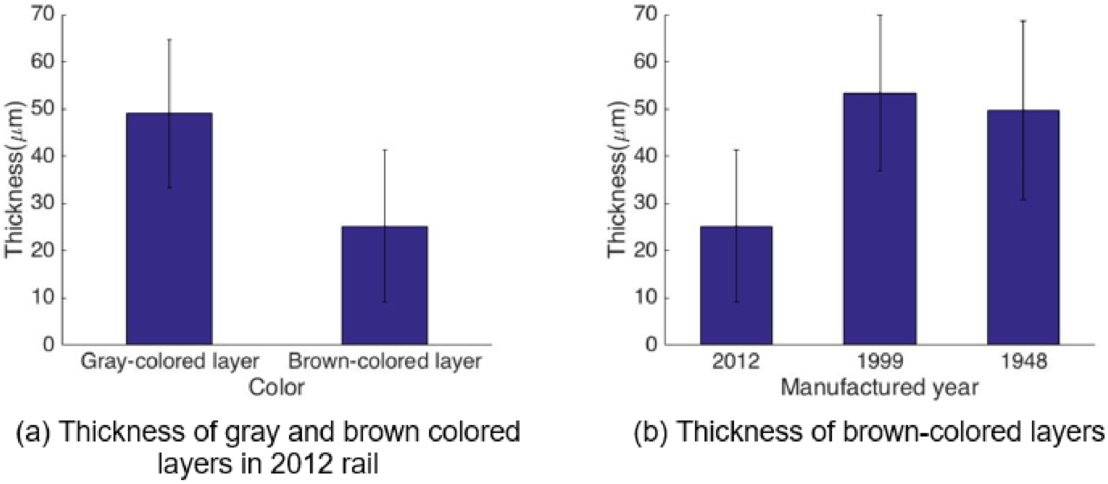

(a) Thickness of gray and brown colored layers in 2012 rail

(b) Thickness of brown-colored layers

Figure 22. Thickness of Gray and Brown-Colored Layers

Table 8. Average Thickness and Standard Deviation of Gray and Brown-Colored Layers

	2012 rail (gray)	**2012 rail (brown)**	**1999 rail (brown)**	**1948 rail (brown)**
Average thickness (μm)	49.0	25.2	53.3	49.7
Standard deviation (μm)	15.6	16.1	16.5	19.0

Table 9. Comparison of Morphological Features

	2012 rail (gray)	**2012 rail (brown)**	**1999 rail (brown)**	**1948 rail (brown)**
Surface smoothness	Smooth	Rough	Rough	Rough
Uniformity of thickness	Uniform	Non-uniform	Non-uniform	Non-uniform
Exfoliation(cracks) or crevice between oxide layer and parent steel	No cracks	Many exfoliation	Many cracks	Few cracks

2.4.2 Raman Spectroscopy

Raman spectra were obtained by using both the Renishaw RM1000B with a 514-nm laser and the Ocean Optics QE Pro with a 785-nm laser. Reference Raman spectra were obtained from the pure powders of Hematite (α-Fe_2O_3), Goethite (α-FeOOH) and Lepidocrocite (ɣ-FeOOH). These are iron oxides and hydroxides typically found on rail steel. To characterize the outer layer of the gray and brown-colored layer on the 2012, 1999 and 1948 rails, Raman spectra were obtained from the surface of the samples without any surface treatment. In addition, Raman spectra on the cross-section were obtained from the 2012, 1999 and 1948 rails to characterize the layer between the outer layer and parent material. The respective experimental procedure is described in order as shown in Figure 23.

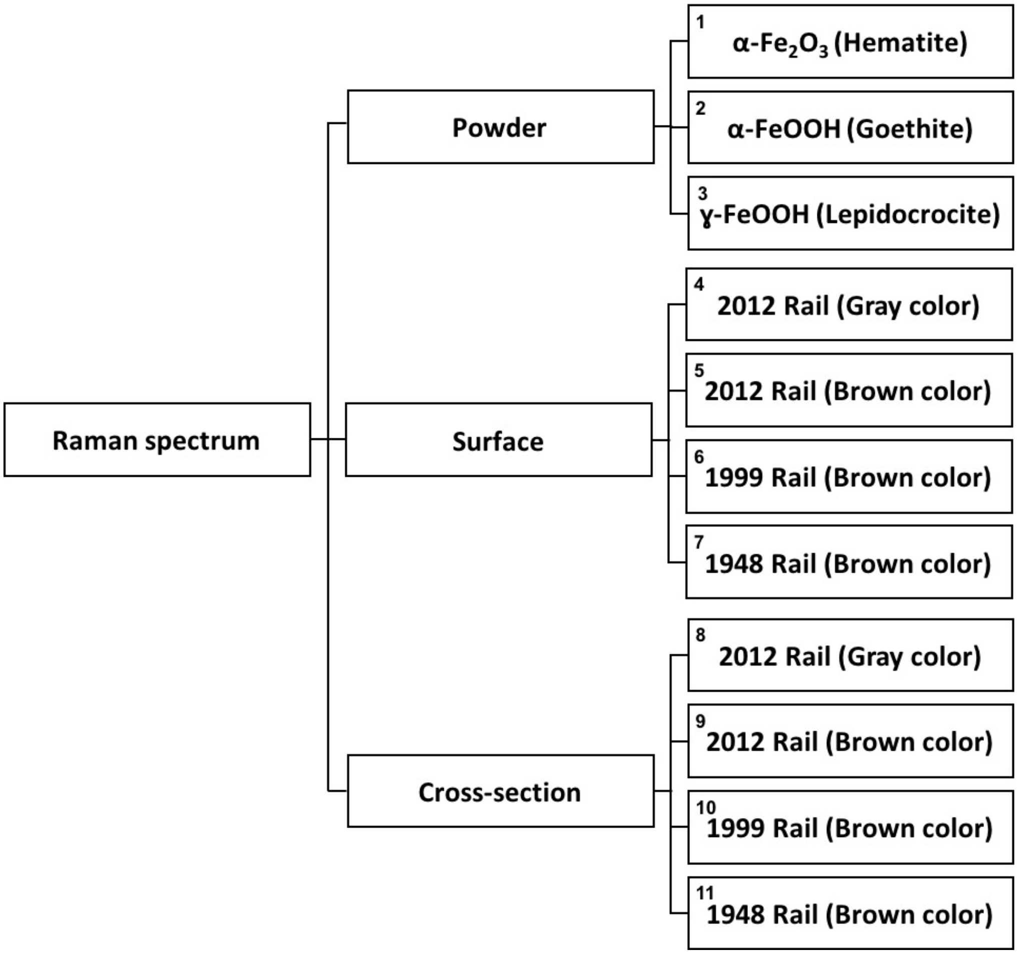

Figure 23. The Experimental Procedure of Raman Spectroscopy

2.4.2.1 Reference Raman Spectra of Iron Oxide and Hydroxide Powders

Reference Raman spectra were obtained from the pure powders of Hematite (α-Fe_2O_3), Goethite (α-FeOOH) and Lepidocrocite (γ-FeOOH) which are common types of iron oxides and hydroxides found on rail steel by using Ocean Optics QE Pro. A 785-nm laser focused on the powders for 10 seconds and accumulated 4 times to obtain distinguishable peaks.

Figure 24 shows the photographs and collected Raman spectra of the powders. Hematite has several peaks at 216, 284, 399, 479, 490, 579, 593 and 603 cm^{-1}. Goethite has peaks at 239, 291, 392, 479 and 536 cm^{-1}. Lepidocrocite has distinguishable peaks at 246.8 and 370.0 cm^{-1}. The reference Raman spectra were used for identifying the iron oxides and hydroxides on the rail samples.

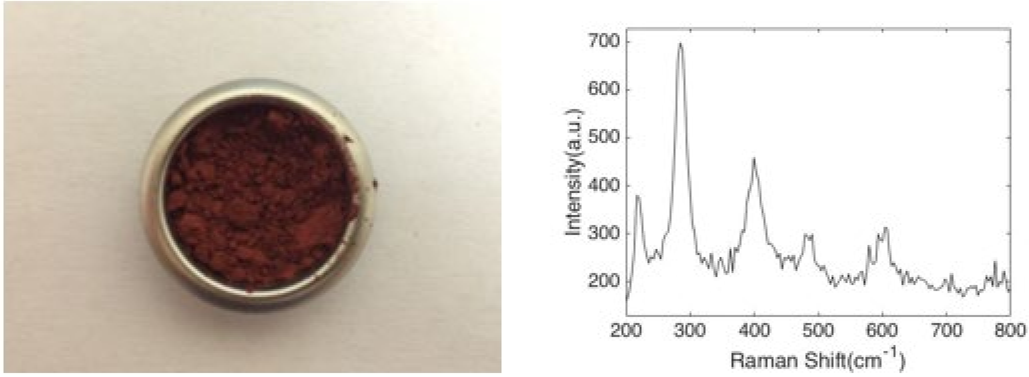

(a) Hematite (α-Fe_2O_3) powder (b) Raman spectrum of Hematite

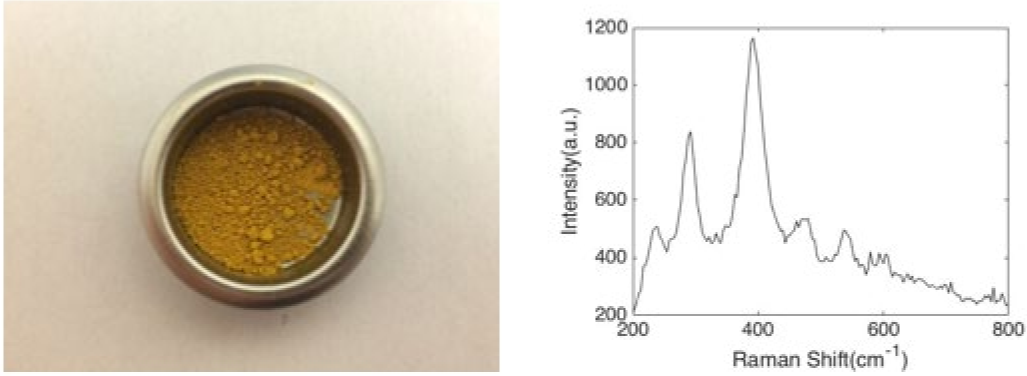

(c) Goethite (α-FeOOH) powder (d) Raman spectrum of Goethite

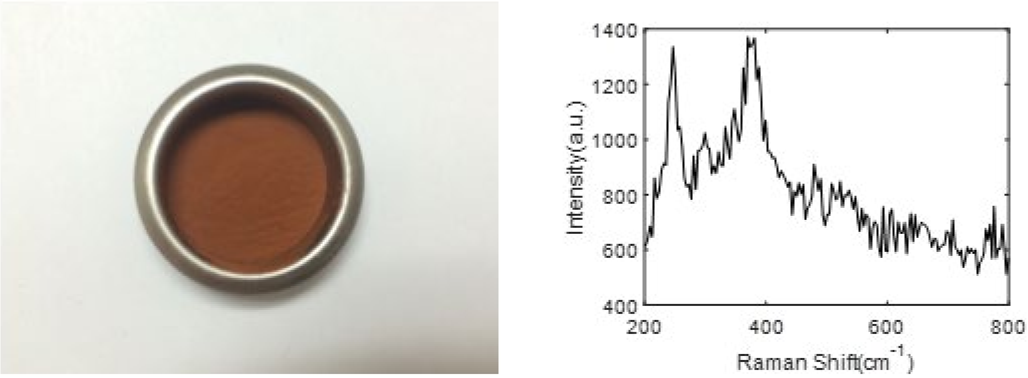

(e) Lepidocrocite (γ-FeOOH) powder (f) Raman spectrum of Lepidocrocite

Figure 24. Photograph and Raman Spectra of Iron Oxide Powders Using a 785-nm Laser

Table 10. Peak Locations of Raman Spectra Collected from Powders

Hematite	216.4	284.4	399.4	479.4	490.2	579.2	593.3	603.9
Goethite	239.2	291.9	392.1	479.4	536.7			
Lepidocrocite	246.4	299.4	371.9					

2.4.2.2 Chemical Identification of Rail Surface Layer

514 nm Laser – 2012 Rail (Gray-Colored Layer)

Raman spectra were obtained from the surface of the gray-colored layer on the 2012 rail. To generate a scattered signal from the target material, a 514-nm laser was focused on the target surface for 120 seconds with a microscope objective of 50X. Figure 25 shows the microscope image and collected Raman spectrum which typically have dominant peaks at 226.9, 247.2, 292.2 and 411.4. Based on the spectra, it was found that Hematite is the outer layer of the gray-colored layer on the 2012 rail. No peaks were found on some samples. The gray surface layer may have become mixed with brown during environmental exposure.

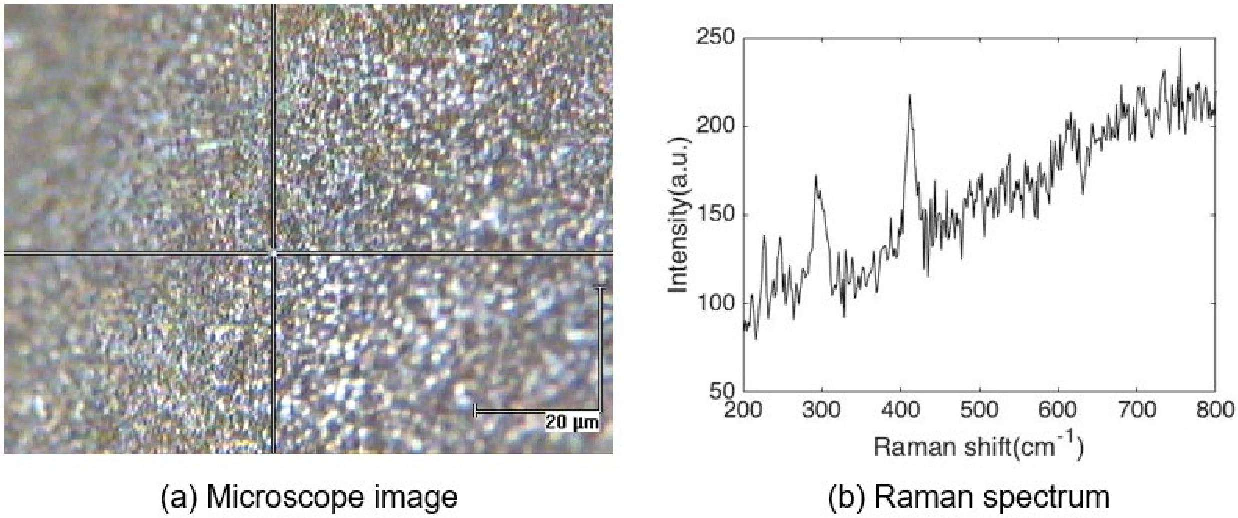

(a) Microscope image

(b) Raman spectrum

Figure 25. Microscope Surface Image and Raman Spectrum of Gray-Colored Layer on 2012 Rail Using a 514-nm Laser [120 Seconds, 1 Averaging, 50X Objective]

785 nm Laser – 2012 Rail (Gray-Colored Layer)

To test for laser wavelength differences, the test was repeated with a 785-nm laser focused on the target surface for 10 seconds. Figure 26 shows the surface photograph and collected Raman spectrum which typically have dominant peaks at 288.2, 406.8, 493.8 and 659.7 cm-1. Based on the peaks at 288.2, 406.8, 493.8 cm-1, it was found that Hematite layer is the outer layer of the gray-colored layer on the 2012 rail. In addition, we could also find the Raman spectrum of Magnetite as well based on the peaks at 659.7 cm-1. However, sometimes no peaks were found as the samples may have become a mixture when they were exposed for 2–3 years under uncontrolled environment.

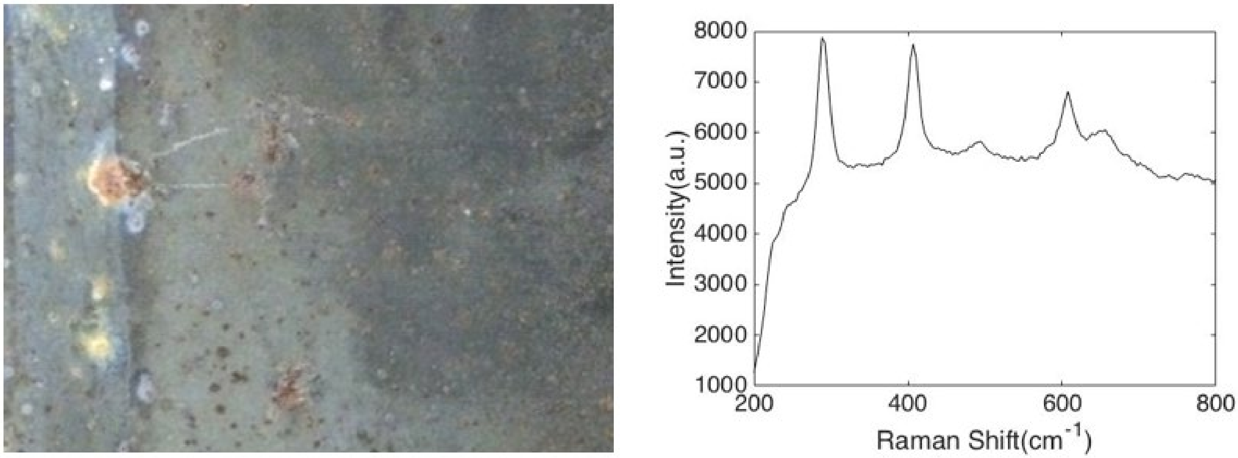

(a) Surface photograph (b) Raman spectrum

Figure 26. Surface Photograph and Raman Spectrum of Gray-Colored Layer on 2012 Rail Using a 785-nm Laser [10 seconds, no Averaging]

514 nm Laser – 2012 Rail (Brown-Colored Layer)

Raman spectra were obtained from the surface of the brown-colored layer on the 2012 rail. To generate scattered signal from the target material, a 514-nm laser was focused on the target surface for 60 seconds and accumulated two times with a microscope objective of 50X. Figure 27 shows the microscopic image and collected Raman spectrum which typically have dominant peaks at 248 and 380 cm^{-1}. Based on the spectra, the brown-colored layer on the 2012 rail contains a mixture of Goethite and Lepidocrocite.

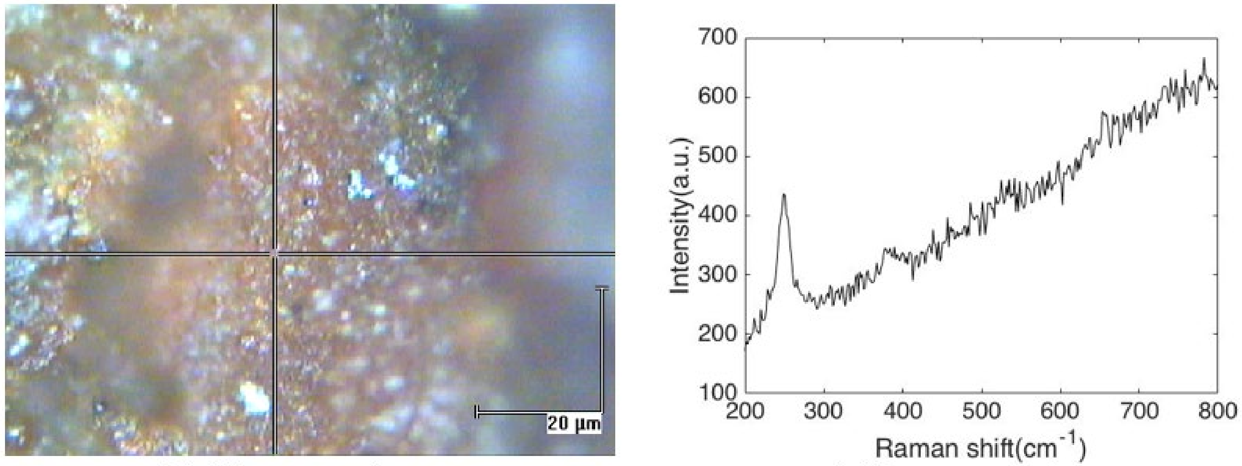

(a) Microscope image (b) Raman spectrum

Figure 27. Microscope Surface Image and Raman Spectrum of Brown-Colored Layer on 2012 Rail Using a 514-nm Laser [60 seconds, 2 Averaging, 50X Objective]

785 nm Laser – 2012 Rail (Brown-Colored Layer)

To test for laser wavelength differences, the test was repeated with a 785-nm laser focused on the target surface for 10 seconds. Figure 28 shows the surface photograph and collected Raman spectrum which typically have dominant peaks at 247 and 373 cm^{-1}. Based on the peak locations, it was found that the mixture of Goethite and Lepidocrocite is the outer layer of the brown-colored layer on the 2012 rail. The results are the same with the 514-nm laser.

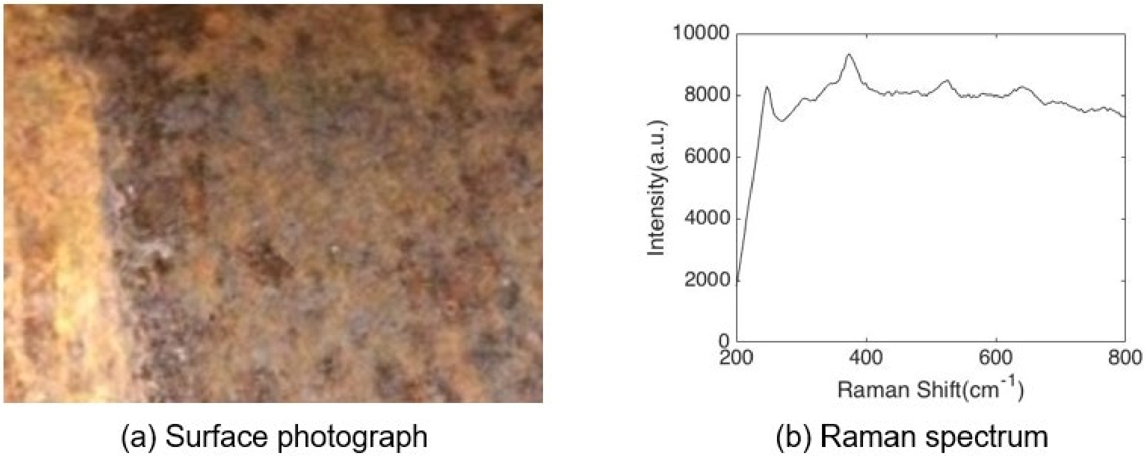

(a) Surface photograph (b) Raman spectrum

Figure 28. Surface Photograph and Raman Spectrum of Brown-Colored Layer on 2012 Rail Using a 785-nm Laser [10 Seconds, no Averaging]

514 nm Laser – 1999 Rail (Brown-Colored Layer)

Raman spectra were obtained from the surface of the brown-colored layer on the 1999 rail. To generate scattered signal from the target material, a 514-nm laser focused on the target surface for 120 seconds with a microscope objective of x50. Figure 29 shows the microscope image and collected Raman spectrum which have blunt peaks at 247 cm^{-1}. A mixture of Goethite and Lepidocrocite is contained in the brown-colored layer on the 1999 rail. However, the peak intensities are too weak to distinguish the materials.

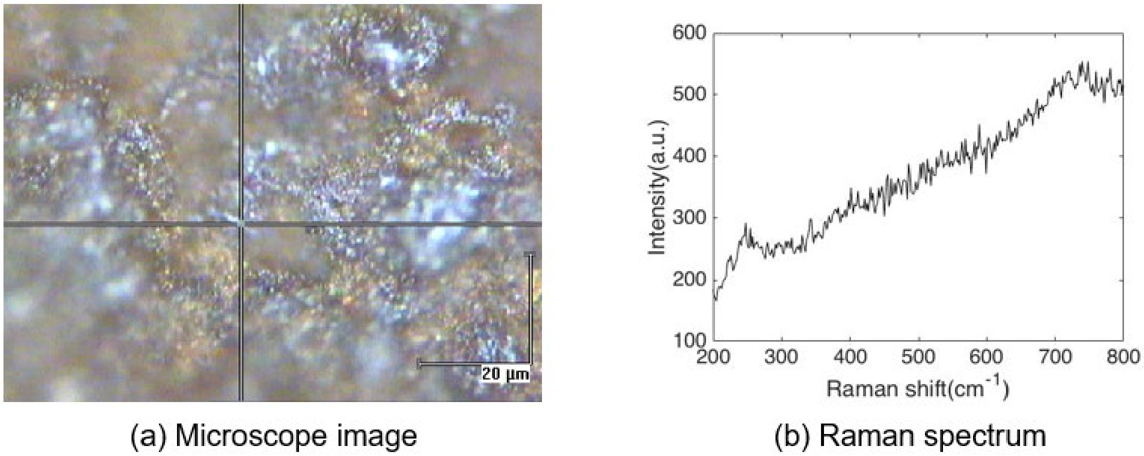

(a) Microscope image (b) Raman spectrum

Figure 29. Microscope Surface Image and Raman Spectrum of Brown-Colored Layer on 1999 Rail Using a 514-nm Laser [120 Second, no Averaging, 50X Objective]

785 nm Laser – 1999 Rail (Brown-Colored Layer)

Raman spectra were obtained from the surface of the brown-colored layer on the 1999 rail repeatedly with different laser. A 785-nm laser focused on the target surface for 10 seconds. Figure 30 shows the surface photograph and Raman spectrum which typically have blunt peaks at 247 and 373 cm^{-1}. Based on the peak locations, it was found that the mixture of Goethite and Lepidocrocite is the outer layer of the brown-colored layer on the 2012 rail. However, the peak intensities are too weak to distinguish the materials. The results are the same with the results using a 514-nm laser.

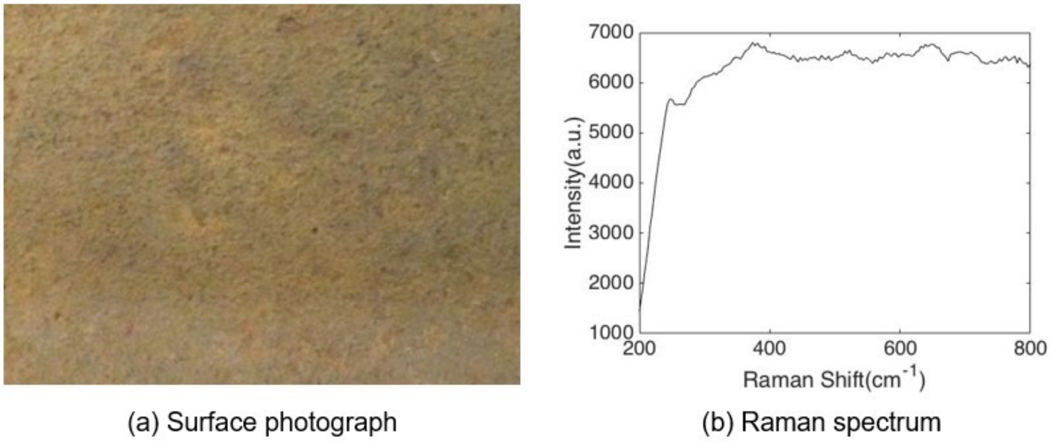

(a) Surface photograph (b) Raman spectrum

Figure 30. Surface Photograph and Raman Spectrum of Brown-Colored Layer on 1999 Rail Using a 785-nm Laser [10 Seconds, no Averaging]

514 nm Laser – 1948 Rail (Brown-Colored Layer)

Raman spectra were obtained from the surface of the brown-colored layer on the 1948 rail. To generate a scattered signal from the target material, a 514-nm laser focused on the target surface for 120 seconds with a microscope objective of 50X. Figure 31 shows the microscope image and collected Raman spectrum. No significant peaks were found from the Raman spectrum. After exposure to the elements for 50+ years, this layer may be composed of another material that is hard to detect using the Raman spectroscopy technique.

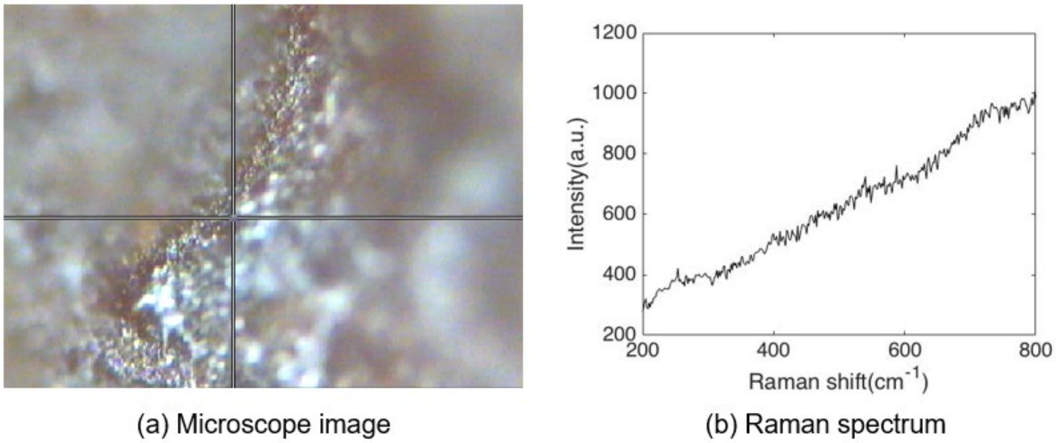

(a) Microscope image (b) Raman spectrum

Figure 31. Microscope Surface Images and Raman Spectra of Brown-Colored Layer on 1948 Rail Using a 514-nm Laser [120 Seconds, no Averaging, 50X Objective]

785 nm Laser – 1948 Rail (Brown-Colored Layer)

Raman spectra were obtained from the surface of the brown-colored layer on the 1948 rail repeatedly with different laser. A 785-nm laser focused on the target surface for 10 seconds. Figure 32 shows the surface photograph and collected Raman spectrum. No significant peaks were found from the Raman spectrum as the layer changed to another material which is hard to detect using the Raman spectroscopy technique when it is exposed in the uncontrolled environment for more than 50 years. The results are the same with the results using the 514-nm laser.

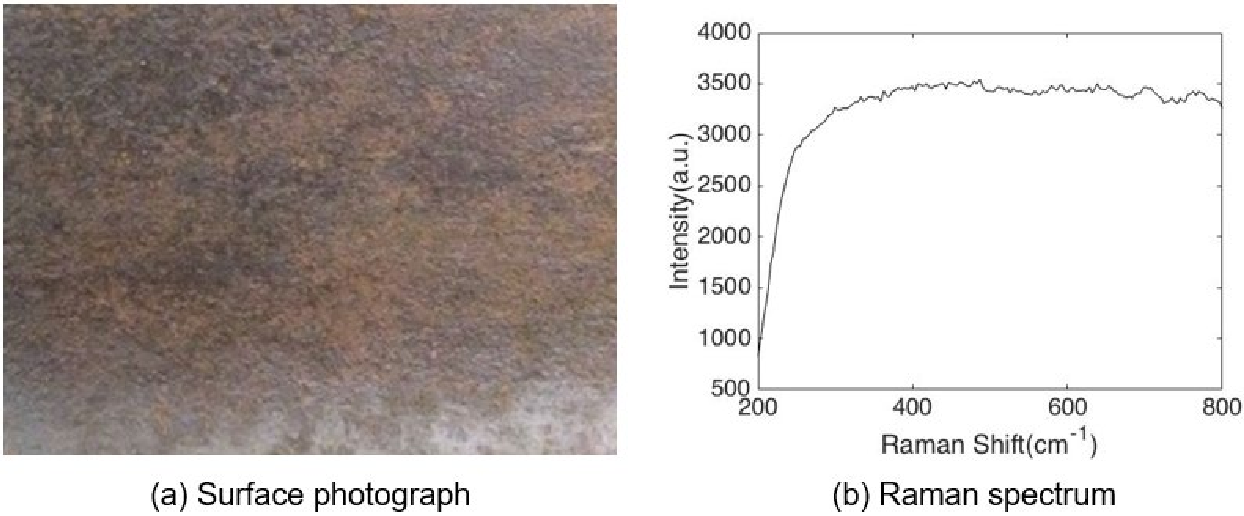

(a) Surface photograph

(b) Raman spectrum

Figure 32. Surface Photograph and Raman Spectra of Brown-Colored Layer on 1948 Rail Using a 785-nm Laser [10 Seconds, no Averaging]

2.4.2.3 Chemical Identification of Rail Surface Layer (Cross-Section)

Raman spectra were obtained from the cross-section of the gray and brown-colored layer on the 2012, 1999 and 1948 rails. The Benchtop Raman spectroscopy system with a 514-nm laser was used for focusing the laser on the cross-section of iron oxide or hydroxides using a microscope objective of 50X. Figure 33 shows the microscope images and Raman spectra collected for 120 seconds. No dominant peaks were found from the Raman spectra.

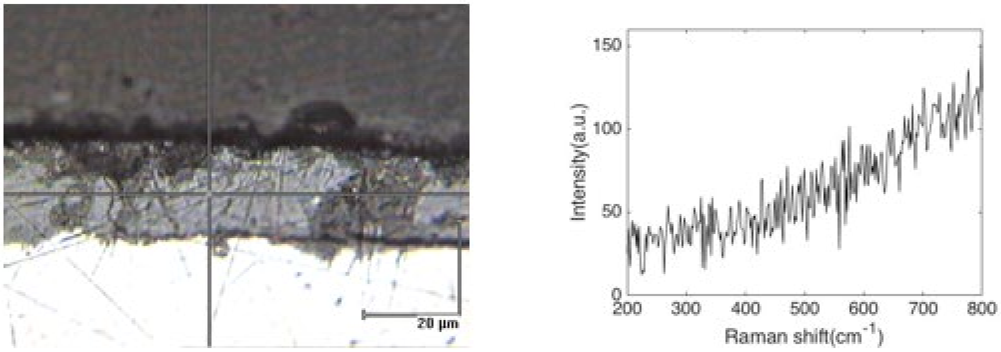

(a) SEM image of 2012 rail (gray) (b) Raman spectrum of 2012 rail

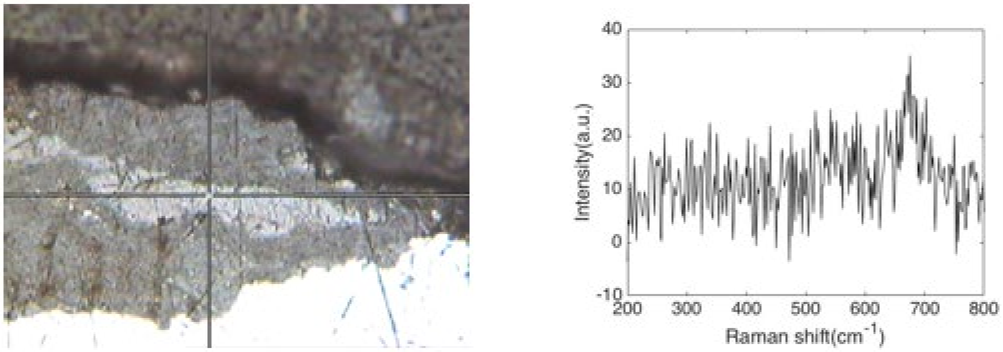

(c) SEM image of 1999 rail (brown) (d) Raman spectrum of 1999 rail

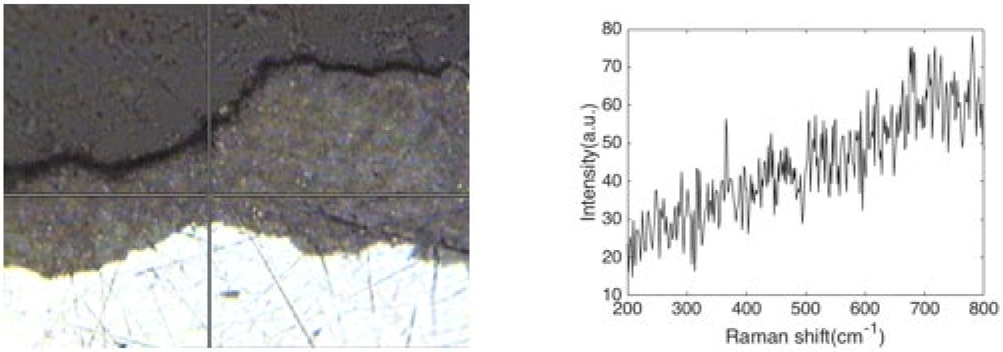

(e) SEM image of 1948 rail (brown) (f) Raman spectrum of 1948 rail

Figure 33. SEM Cross-Section Images and Raman Spectra

2.4.2.4 Summary of Raman Spectroscopy

Raman spectra were obtained from the pure iron oxide/hydroxide powder on the surface and cross-section of the three rails using both the 514 nm and 785-nm laser. It was found that the 514 nm and 785-nm lasers produced similar results, but the data from the 785 nm laser tests have a lower background noise level. For example, the Magnetite peak at 660 cm^{-1} can be found on the gray-colored layer using a 785-nm laser, but a 514-nm laser could not generate the Raman scattering signal of Magnetite.

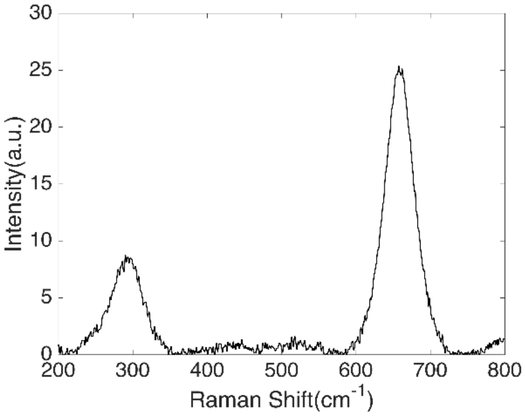

Figure 34. Raman Spectrum of Magnetite

Raman spectra were obtained from the surface of the samples without any surface treatment. The Hematite (α-Fe_2O_3) and Magnetite (Fe_3O_4) were found on the gray-colored layer on the 2012 rail. The Goethite (α-FeOOH) and Lepidocrocite (γ-FeOOH) were found on the brown-colored layer on the 2012 and 1999 rails. However, the Raman spectra on the 1999 rail are less intense on the 2012 rail. Finally, the 1948 rail has no distinguishable Raman spectrum on the surface.

2.4.3 X-Ray Diffraction Spectroscopy Analysis

XRD patterns were obtained by using PANalytical Empyrean to identify the molecular structures in oxide/hydroxide layers on the rail and verify the results of Raman spectroscopic tests. After obtaining XRD patterns, experimentally obtained XRD patterns were compared with the reference XRD patterns from literature.

2.4.3.1 Test Result and Summary of XRD

XRD patterns were obtained from the surface of the gray-colored layer on the 2012 rail, the brown-colored layer on the 1999 and 1948 rails. It was found that Hematite and Magnetite are the outer layer of the gray-colored layer on the 2012 rail based on the collected XRD pattern as shown in Figure 35(b). The collected XRD pattern has dominant peaks at 33.1, 35.4, 39.4, 43.0 and 56.9 cm^{-1}as show in Table 11. The peak at 36 cm^{-1} is the highest peak among the collected XRD pattern on the 2012 rail.

The two peaks at 33.1 and 35.4 show that Hematite is included in the gray-colored layer. The three peaks at 35.4 and 56.9 show that Magnetite is also in the gray-colored layer. As mentioned above, Hematite and Magnetite have a dominant peak at 36 simultaneously. That is why the collected XRD pattern has a highest peak at 36.

Figure 35(d) shows the collected XRD pattern from the surface of the brown-colored layer on the 1999 rail. The peaks are not vivid as seen from 2012 rail, but are distinguishable. The collected XRD pattern has peaks at 26.6, 35.4 and 58.6. The peak at 26.6 represents that Lepidocrocite is present in the brown-colored layer on the 1999 rail. The peak at 35.4 represents that Goethite is also present in the layer.

Figure 35(f) shows the collected XRD pattern from the surface of the brown-colored layer on the 1948 rail. The XRD pattern has a similar trend with the one from 1999 rail, but the intensities of peaks are too low to distinguish the peaks.

The XRD patterns collected from 2012, 1999 and 1948 rails have similar results with Raman spectroscopy. However, the XRD process requires more integration time to collect the spectrum compared to Raman spectroscopy. In addition, the target sample needs to be thin to use a commercial XRD equipment.

Based on the results of Raman spectroscopy and XRD test, it is found that the surface of gray-colored layer is a mixture of Hematite and Magnetite, and the surface of the brown-colored layer is a mixture of Goethite and Lepidocrocite. The gray-colored layer is scaled off over time, and the surface of the brown-colored layer changes over time to a material that cannot be detected using Raman spectroscopy and XRD.

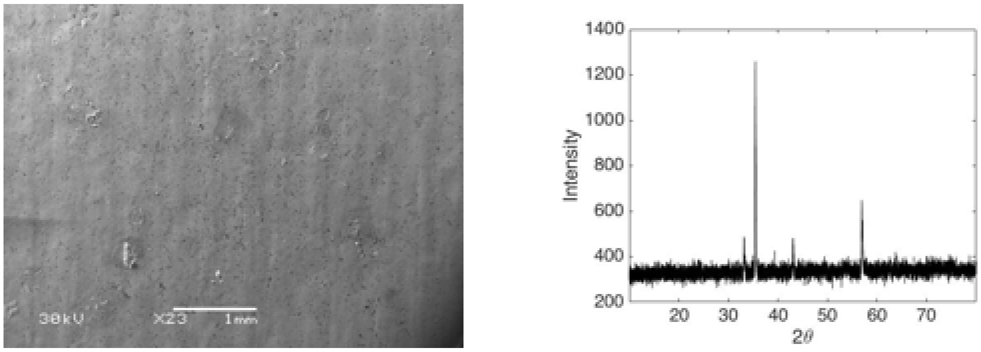

(a) SEM image of 2012 rail (b) XRD spectrum of 2012 rail

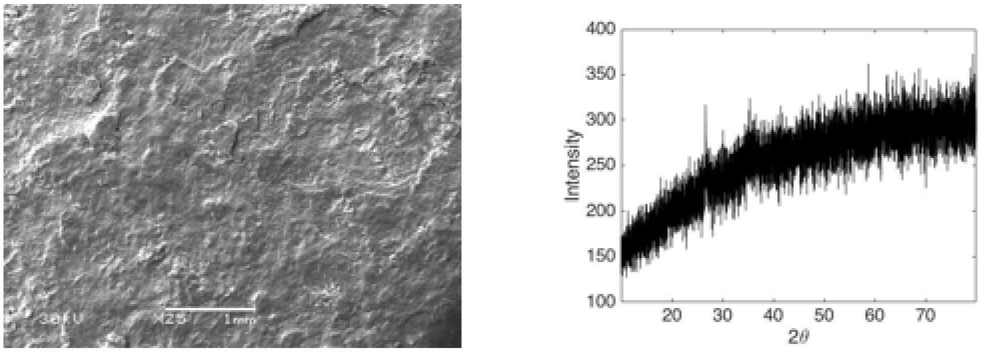

(c) SEM image of 1999 rail (d) XRD spectrum of 1999 rail

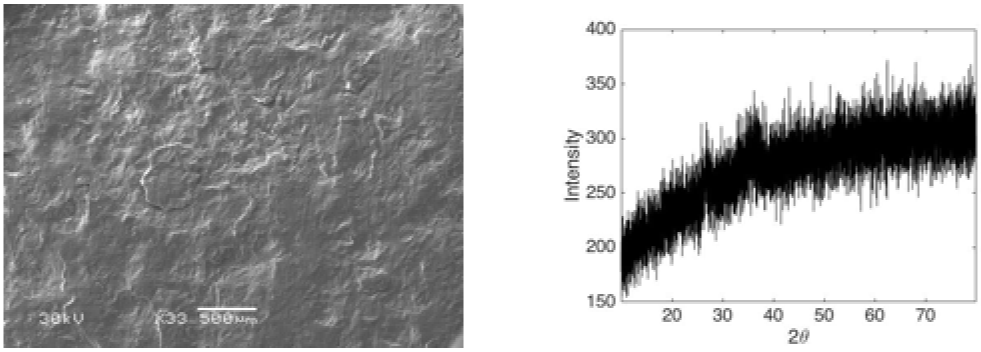

(e) SEM image of 1948 rail (f) XRD spectrum of 1948 rail

Figure 35. SEM Surface Images and XRD Patterns

Table 11. Collected XRD Patterns of the Iron Oxide/Hydroxide on the Rails

Samples	Peak locations				
2012 Rail (Gray-color)	33.14	35.44	39.35	43.04	56.9
1999 Rail (Brown-color)	26.62	35.36	58.75		
1948 Rail (Brown-color)	No distinguishable peaks				

2.4.4 *Energy-Dispersive X-Ray Spectroscopy*

EDX was applied to perform quantitative analysis of atoms in the iron oxide/hydroxide layers. The weight percentages of Fe, O, and C ions measured in the iron oxide and hydroxide layer were compared with the molecular mass percentages of pure iron oxide and hydroxides as shown in Table 12. In addition, the weight percentages of Fe, O, and C ions measured in the rail steel which is a parent material. The respective experimental procedure is shown in Figure 36.

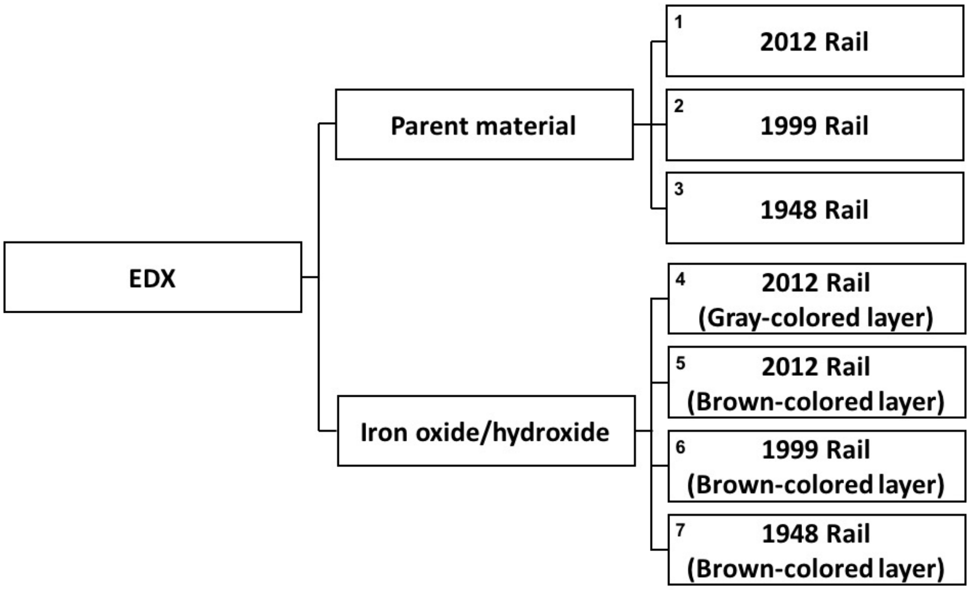

Figure 36. The Experimental Procedure of EDX

Table 12. Molecular Mass Percentage of Iron Oxides

	FeO	**Fe_2O_3**	**Fe_3O_4**	**FeOOH**	**$FeCO_3$**
Fe	77.7 %	69.9 %	72.4 %	62.9 %	48.2 %
O	22.3 %	30.1 %	27.6 %	36.0 %	41.4 %
H				1.1 %	
C					12.0 %

2.4.4.1 *Test Results — Rail Parent Material*

EDX spectra were obtained from the parent material of the 2012, 1999 and 1948 rails. Figure 37 and Table 13 show SEM images, collected EDX spectra and the weight percentages of the parent materials, respectively. The EDX spectra were obtained at the plus sign locations shown in the figures. Based on the spectra, it was found that the parent materials of the three samples have a little difference in weight percentage of chemical composition, but the parent materials mostly consist of Fe, C and O.

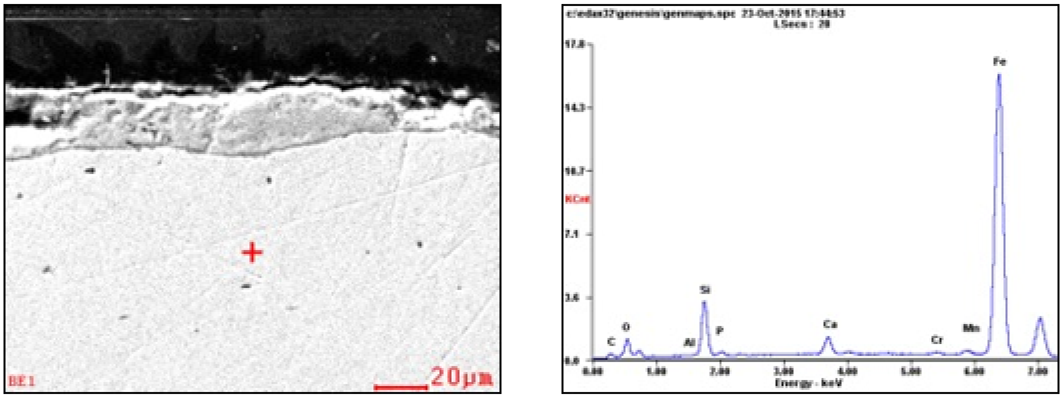

(a) SEM image of 2012 rail (b) EDX spectrum of 2012 rail

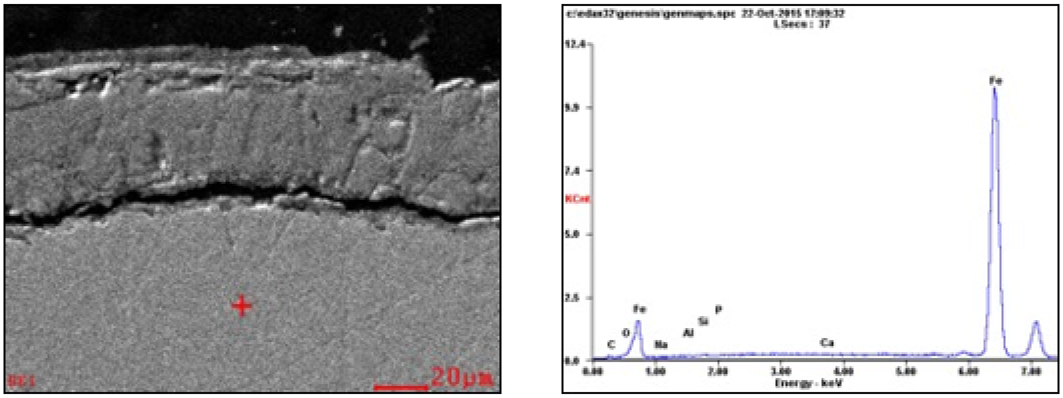

(c) SEM image of 1999 rail (d) EDX spectrum of 1999 rail

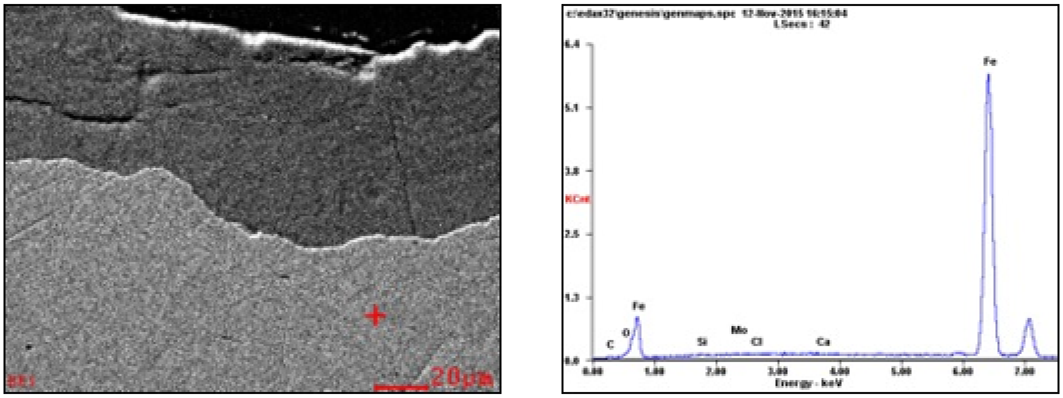

(e) SEM image of 1948 rail (f) EDX spectrum of 1948 rail

Figure 37. SEM images and EDX spectra for rail parent material

Table 13. Weight percentage of rail parent material

Element	2012 rail	1999 rail	1948 rail
Fe	**90.9 %**	**89.9 %**	**90.6 %**
C	**3.7 %**	**6.1 %**	**5.3 %**
O	**2.1 %**	**2.5 %**	**2.4 %**
Si	0.9 %	0.6 %	0.6 %
Mo			0.7 %
Cl			0.3 %
Ca	0.1 %	0.1 %	0.1 %
Na		0.2 %	
Al	0.3 %	0.1 %	
P	0.1 %	0.2 %	
Cr	0.4 %		
Mn	0.1 %		

2.4.4.2 Test Results - Iron oxide/hydroxide layer

EDX spectra for Fe, O and C were obtained from the iron oxide/hydroxide layer on the 2012, 1999 and 1948 rails. To identify the molecular structures of the iron oxide and hydroxide layers on the rails based on the weight percentages, the obtained weight percentages by EDX were compared to the one of pure iron oxides. Table 12 shows the molecular mass percentage of the pure iron oxides.

Gray-colored layer on the 2012 Rail

EDX spectra were obtained from the gray-colored layer on the 2012 rail. Figure 38 shows the SEM image and collected EDX spectrum. The EDX spectrum was collected at the plus sign on the gray-colored oxide layer in the SEM image. Table 14 shows the average weight and atomic percentages of the gray-colored layer. Based on the obtained EDX spectra, it is found that the obtained weight percentages were not well matched with the one of pure iron oxides such as FeO, Fe_2O_3 and Fe_3O_4. This may because the layer was grown by the oxidation process of rail steel which is an impure steel.

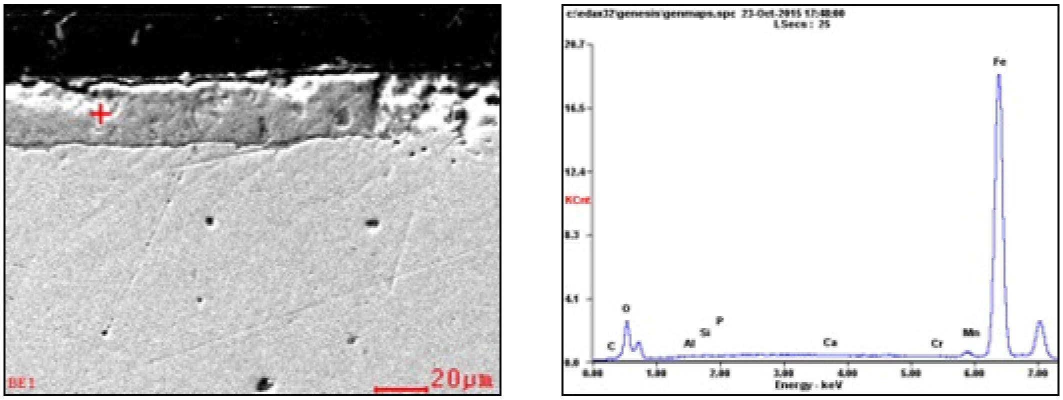

(a) SEM image of gray-colored layer (b) EDX spectrum of gray-colored layer

Figure 38. SEM images and EDX spectra for gray-colored layer on 2012 rail.

Table 14. Average weight and atomic percentages of gray-colored layer on 2012 rail

Element	Weight percentage (%)	Atomic percentage (%)
Fe	77.7 % (84.1 %)	50.6 %
O	14.6 % (15.9 %)	33.2 %
C	4.4 %	13.0 %

Brown-colored layer on the 2012 Rail

EDX spectra were obtained from the brown-colored layer on the 2012 rail. Figure 39 shows the SEM image and collected EDX spectrum. The EDX spectrum was collected at the box sign location on the brown-colored layer in the SEM image. Table 15 shows the average weight and atomic percentages of the brown-colored layer. It is found that the brown-colored layer has less Fe ions and more O ions than gray-colored layer, as shown in Figure 40. Molecular information cannot be obtained using EDX, as the technique is a quantitative analysis of atoms. However, the molecular information can be estimated using the weight percentage. Based on the comparison between obtained weight percentages and the one from pure iron oxide/hydroxide, the molecular construction of the gray-colored layer is like iron oxides such as FeO, Fe_2O_3 and Fe_3O_4. Brown-colored layer is like iron hydroxide which is FeOOH.

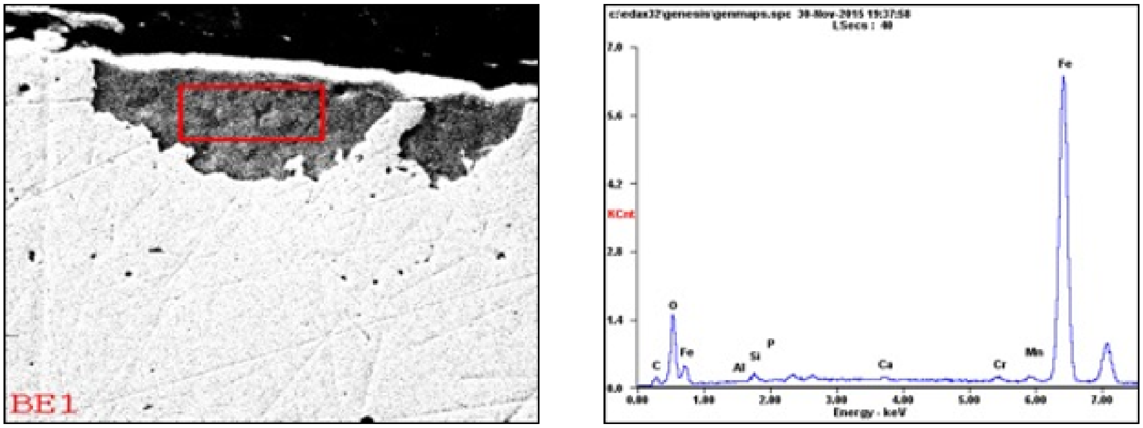

(a) SEM image of brown-colored layer (b) EDX spectrum of brown-colored layer

Figure 39. SEM images and EDX spectra for brown-colored layer on 2012 rail.

Table 15. Average weight and atomic percentages of brown-colored layer on 2012 rail

Element	Weight percentage (%)	Atomic percentage (%)
Fe	59.9 % (71.9 %)	28.7 %
O	23.4 % (28.1 %)	39.1 %
C	13.3 %	29.6 %

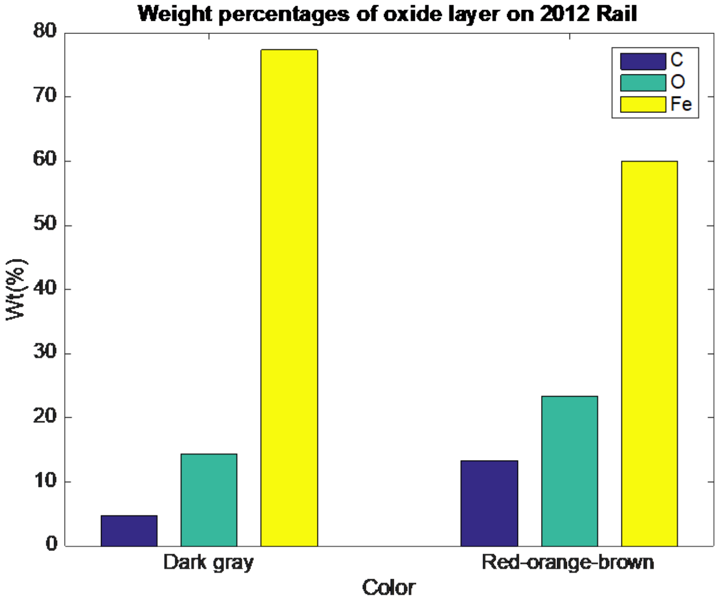

Figure 40. Weight percentages of the gray and brown-colored layer on 2012 rail.

Brown-colored layer on the 1999 Rail

EDX spectra were obtained from the brown-colored layer on the 1999 rail. Figure 41 shows the SEM image and collected EDX spectrum. The EDX spectrum was collected at the plus sign location on the brown-colored layer in the SEM image. Table 16 shows the average weight and atomic percentages of the brown-colored layer. The brown-colored layer mostly consists of 78% of Fe, 15% of O and 5% of C.

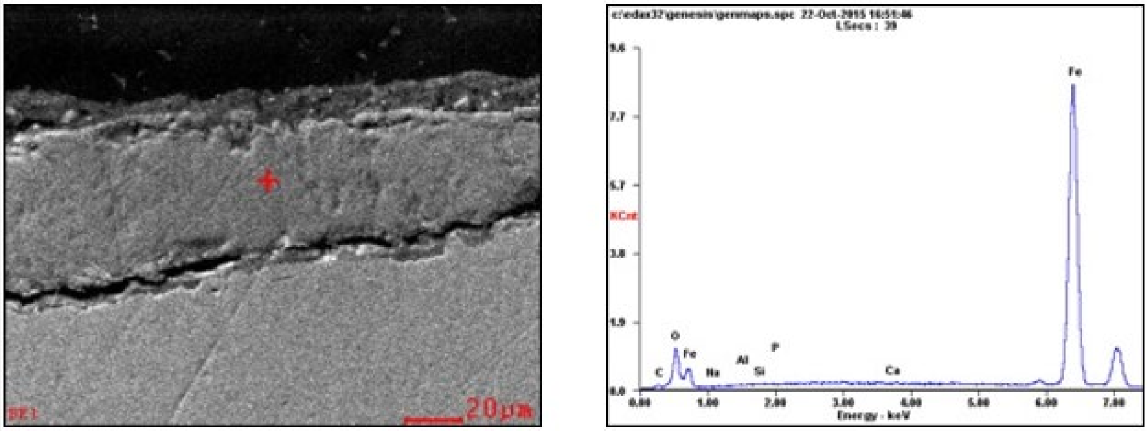

(a) SEM image of brown-colored layer

(b) EDX spectrum of brown-colored layer

Figure 41. SEM images and EDX spectra for brown-colored layer on 1999 rail (1).

Table 16. Average weight and atomic percentages of brown-colored layer on 1999 rail

Element	Weight percentage (%)	Atomic percentage (%)
Fe	78.2 %	49.4 %
	(84.1 %)	
O	14.8 %	32.7 %
	(15.9 %)	
C	5.41 %	15.9 %

Brown-colored layer on the 1948 Rail

EDX spectra were obtained from the brown-colored layer on the 1948 rail. Figure 42 shows the SEM image and collected EDX spectrum. The EDX spectrum was collected at the plus sign location on the brown-colored layer in the SEM image. Table 17 shows the average weight and atomic percentages of the brown-colored layer. The brown-colored layer mostly consists of 64% of Fe, 23% of O and 11% of C.

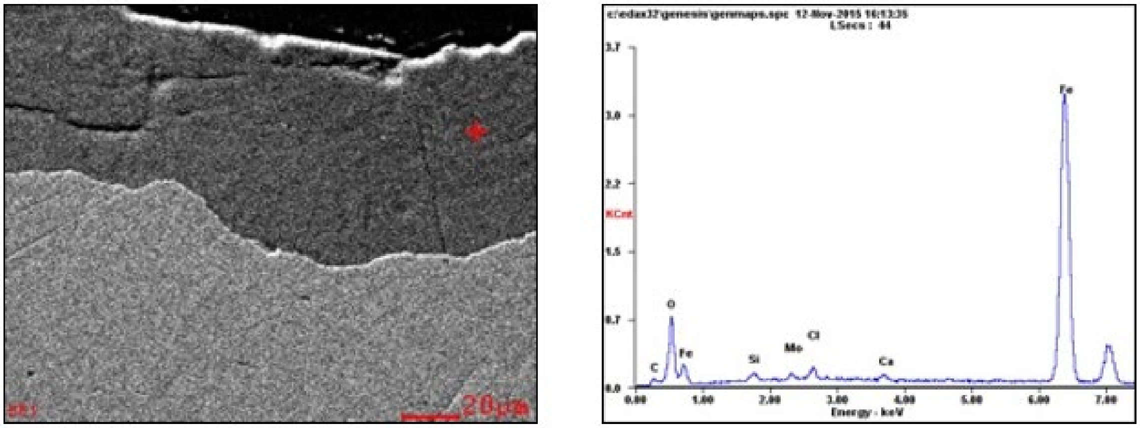

(a) SEM image of brown-colored layer (b) EDX spectrum of brown-colored layer

Figure 42. SEM images and EDX spectra for brown-colored layer on 1948 rail (1).

Table 17. Average weight and atomic percentages of brown-colored layer on 1948 rail.

Element	Weight percentage (%)	Atomic percentage (%)
Fe	63.7 %	32.4 %
	(73.7 %)	
O	22.8 %	40.4 %
	(26.3 %)	
C	10.5 %	24.8 %

EDX spectra were obtained from the brown-colored layer on the 2012, 1999 and 1948 rails. Figure 43 and Table 18 show the weigh percentages of the brown-colored layers on the different rails. from a comparison between the collected obtained weight percentages and pure iron oxide/hydroxide data, we conclude that the molecular composition of the brown-colored layers is similar to iron hydroxide which is FeOOH. The weight percentage of 1999 rail is however similar to iron oxide, which is FeO, Fe_2O_3 and Fe_3O_4 since the prepared sample has a brown-colored layer grown on top of the gray-colored layer.

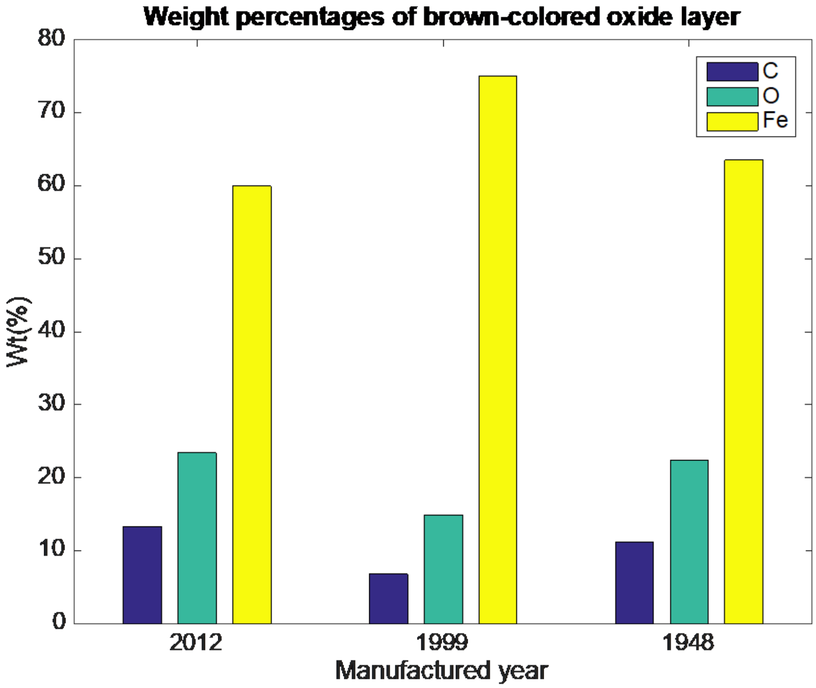

Figure 43. Weight percentages of the brown-colored layer on 2012, 1999 and 1948 rails.

Table 18. Weight percentages of brown-colored layer on 2012, 1999 and 1948 rails.

Element	**Weight percentage (%)**		
	2012 Rail	**1999 Rail**	**1948 Rail**
Fe	59.9 %	78.2 %	63.7 %
O	23.4 %	14.8 %	22.8 %
C	13.3 %	5.41 %	10.5 %

2.4.4.3 Summary of EDX

Based on the results of the EDX test, we conclude that the gray-colored layer contains iron oxides such as FeO, Fe_2O_3 and Fe_3O_4, and the brown-colored layer contains iron hydroxides, FeOOH. This brown-colored layer sometimes grows on the surface of iron oxides when it is exposed to uncontrolled environments over time and the layer is not uniform. The brown layer, therefore, may not be suitable for use as a passive stress sensor.

2.4.5 Nano-indentation

Nano-indentation was used to measure the mechanical properties of the iron oxide and hydroxide layers on the rails. Four sets of nano-indentation tests were performed on the 2012, 1999 and 1948 rails. The parent material, which is rail steel, was additionally indented for measuring the reference elastic modulus of 200 GPa. To have the accurate mechanical properties, forty points (4 points x 10 points) were indented, and the dimensions were 30 µm (width) and 90 µm (depth). The results were compared to the mechanical properties of pure oxide and hydroxides as shown in Table 19 [4], [5] . The respective experimental procedures are described in order as shown in Figure 44.

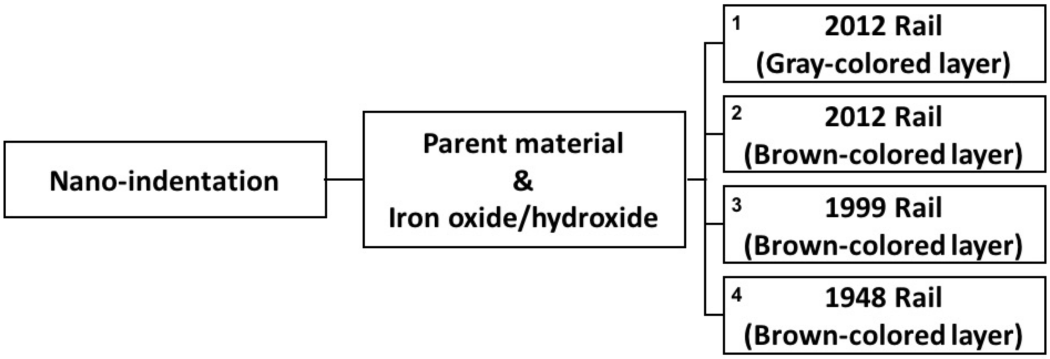

Figure 44. The experimental procedure of nano-indentation.

Table 19. Mechanical properties of pure iron oxides and typical rail steel

	α-Fe_2O_3	Fe_3O_4	α-FeOOH	γ-FeOOH	Rail steel
Elastic modulus	359 GPa	175 GPa	358 GPa	350 GPa	200 GPa
Hardness	2.7 GPa	5.3 GPa	1.1 GPa	-	-

2.4.5.1 Test result

Gray-colored layer on the 2012 rail

Nano-indentation was performed on the gray-colored layer and the parent material for the 2012 rail. Figure 45 shows the SEM images and calculated elastic modulus and hardness. The top, middle and bottom layers are epoxy, gray-colored and parent material layers, respectively (Figure 45(a)). Forty points were indented as shown in the boxed area of the SEM images. Twenty, twelve and eight points were indented on the parent material, gray-colored layer and the border between parent material and gray-colored layer respectively as shown in Figure 45(b). Using the nano-indentation test, it was found that the gray-colored layer has an elastic modulus of 107.3 GPa and nano-hardness of 7.1 GPa. The elastic modulus of the gray-colored layer is similar with the parent material, but the layer has higher hardness than the parent material as shown in Figure 45(c)-(f).

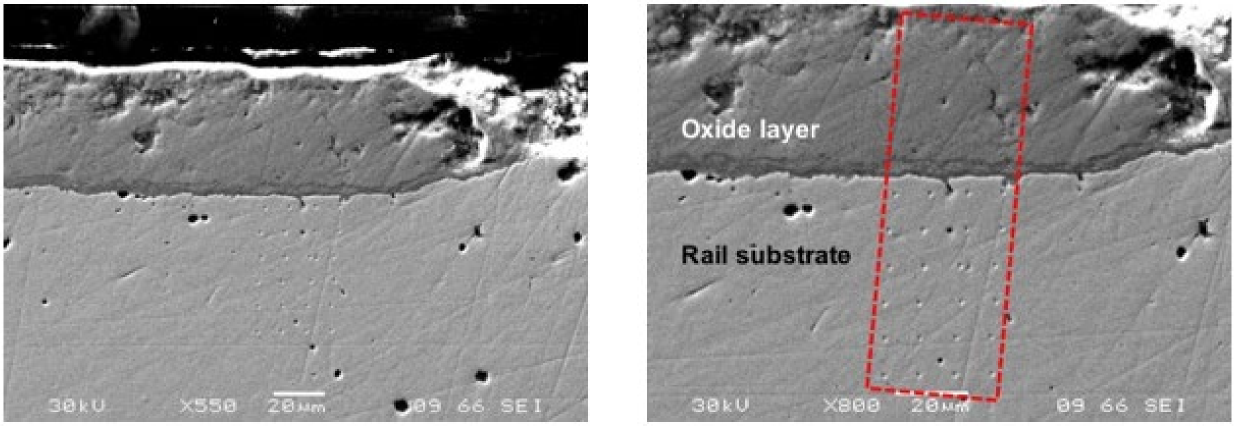

(a) SEM image (x550, 30kV)

(b) SEM image (x800, 30kV)

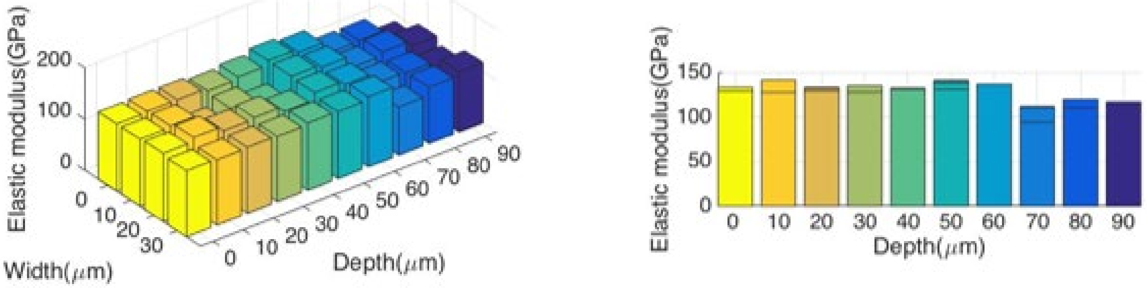

(c) Elastic modulus (Isometric view)

(d) Elastic modulus (2D view)

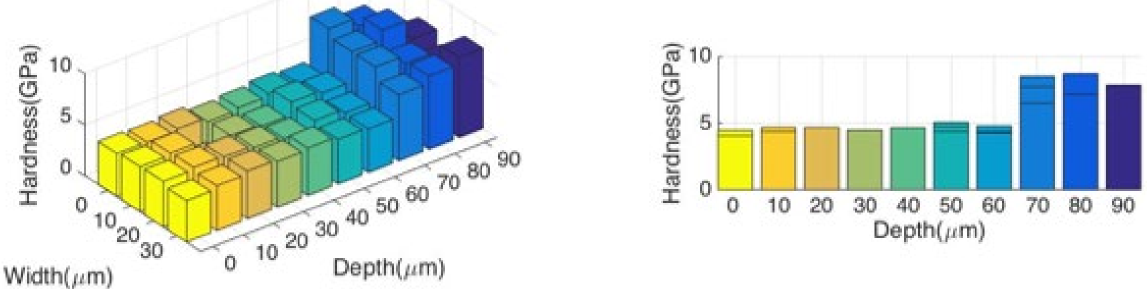

(e) Nano-hardness (Isometric view)

(f) Nano-hardness (2D view)

Figure 45. SEM images and nano-indentation results for iron oxide layer on 2012 rail.

Brown-colored layer on the 2012 rail

Nano-indentation was performed on the brown-colored layer and the parent material on the 2012 rail. Figure 46 shows the SEM images and calculated elastic modulus and hardness. The top, middle and bottom layers are epoxy, brown-colored and parent material layers respectively as shown in Figure 46(a). Forty points were indented in the box sign in the SEM images. Sixteen, sixteen and eight points were indented on the parent material, brown-colored layer and the border between parent material and brown-colored layer respectively as shown in Figure 46(b). It was found that the brown-colored layer has an elastic modulus of 48.7 GPa and nano-hardness of 2.5 GPa. The elastic modulus and hardness of the brown-colored layer are smaller than the parent material as shown in Figure 46(c)-(f). In addition, the obtained elastic modulus and hardness of brown-colored layer are lower than the gray-colored layer on the 2012 rail.

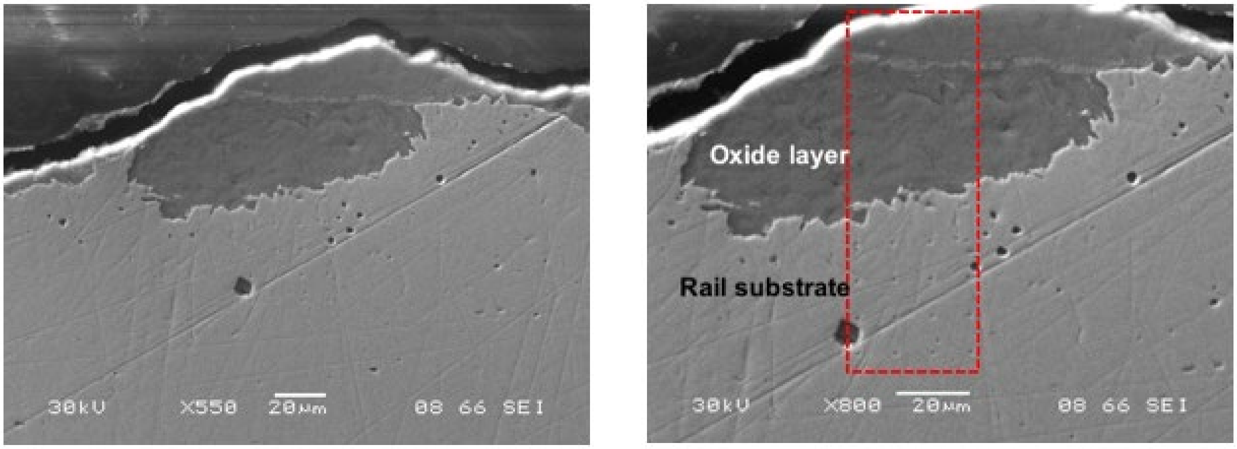

(a) SEM image (x550, 30kV) (b) SEM image (x800, 30kV)

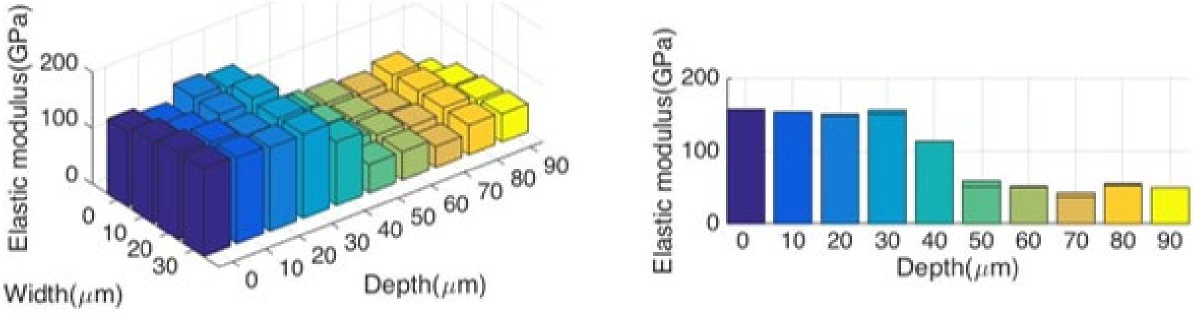

(c) Elastic modulus (Isometric view) (d) Elastic modulus (2D view)

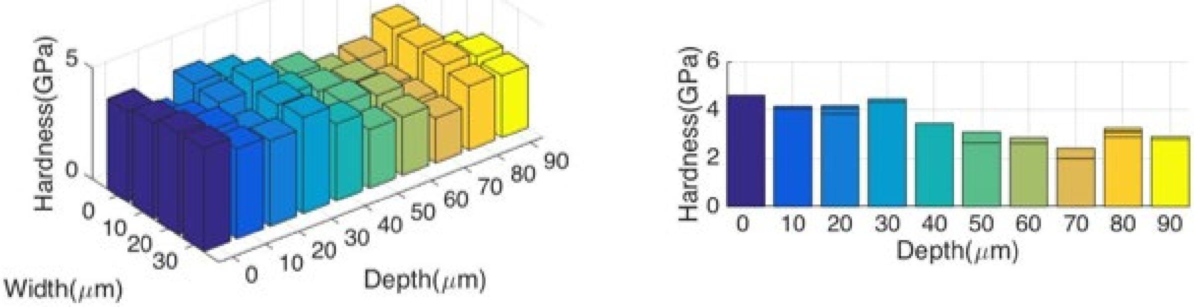

(e) Nano-hardness (Isometric view) (f) Nano-hardness (2D view)

Figure 46. SEM images and nano-indentation results for iron hydroxide layer on 2012 rail.

Brown-colored layer on the 1999 rail

Nano-indentation was performed on the brown-colored layer and the parent material on the 1999 rail. Figure 47 shows the SEM images and calculated elastic modulus and hardness. The top, middle and bottom layers are epoxy, brown-colored and parent material layers respectively as shown in Figure 47(a). Forty points were indented in the box sign in the SEM images. Twelve, twenty and eight points were indented on the parent material, brown-colored layer and the border between parent material and brown-colored layer respectively as shown in Figure 47(b). It wss found that the brown-colored layer has an elastic modulus of 39.4 GPa and nano-hardness of 1.8 GPa. The elastic modulus and hardness of the brown-colored layer are lower than the parent material as shown in Figure 47(c)-(f). In addition, the obtained elastic modulus and hardness of brown-colored layer on the 1999 rail are even lower than brown-colored layer on the 2012 rail.

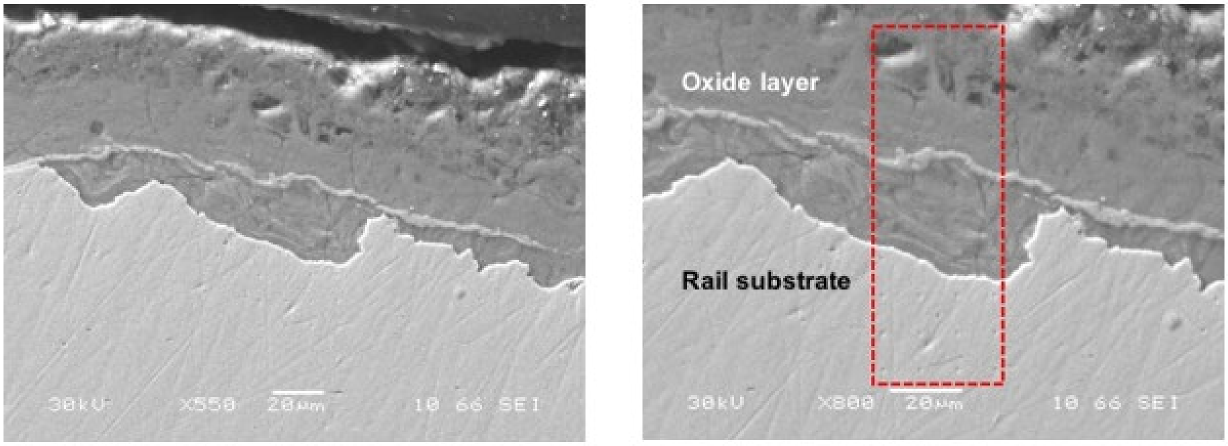

(a) SEM image (x550, 30kV) (b) SEM image (x800, 30kV)

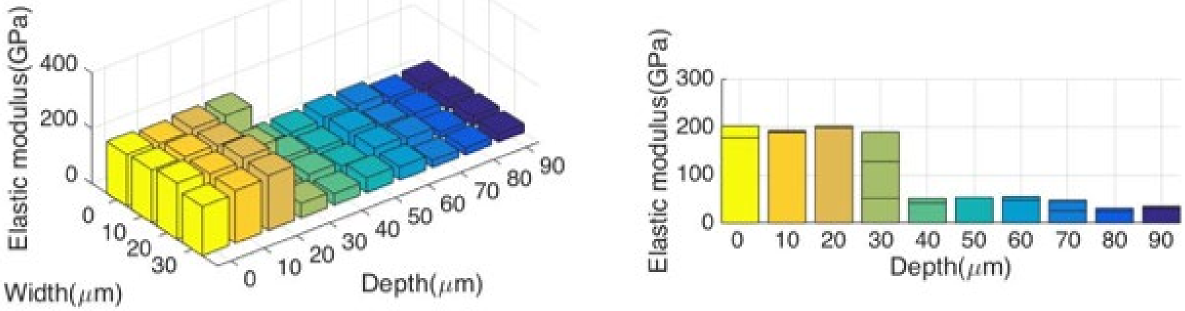

(c) Elastic modulus (Isometric view) (d) Elastic modulus (2D view)

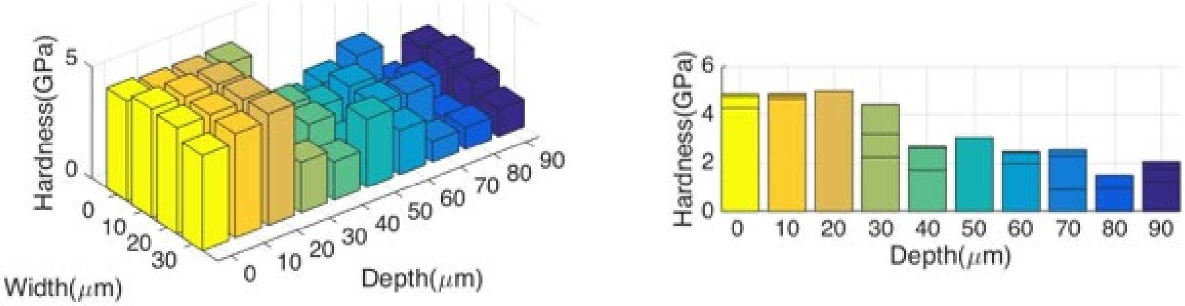

(e) Nano-hardness (Isometric view) (f) Nano-hardness (2D view)

Figure 47. SEM images and nano-indentation results for iron hydroxide layer on 1999 rail.

Brown-colored layer on the 1948 rail

Nano-indentation was performed on the brown-colored layer and the parent material on the 1948 rail. Figure 48 shows the SEM images and calculated elastic modulus and hardness. The top, middle and bottom layers are epoxy, brown-colored and parent material layers respectively as shown in Figure 48(a). Forty points were indented in the box sign in the SEM images. Sixteen, sixteen and eight points were indented on the parent material, brown-colored layer and the border between parent material and brown-colored layer respectively as shown in Figure 48(b). It is found that the brown-colored layer has an elastic modulus of 49.7 GPa and nano-hardness of 1.9 GPa. The elastic modulus and hardness of the brown-colored layer are lower lower than the parent material as shown in Figure 48(c)-(f). In addition, the obtained elastic modulus of brown-colored layer on the 1948 rail is like the brown-colored layer on the 2012 rail, and the nano-hardness is like the brown-colored layer on the 1999 rail.

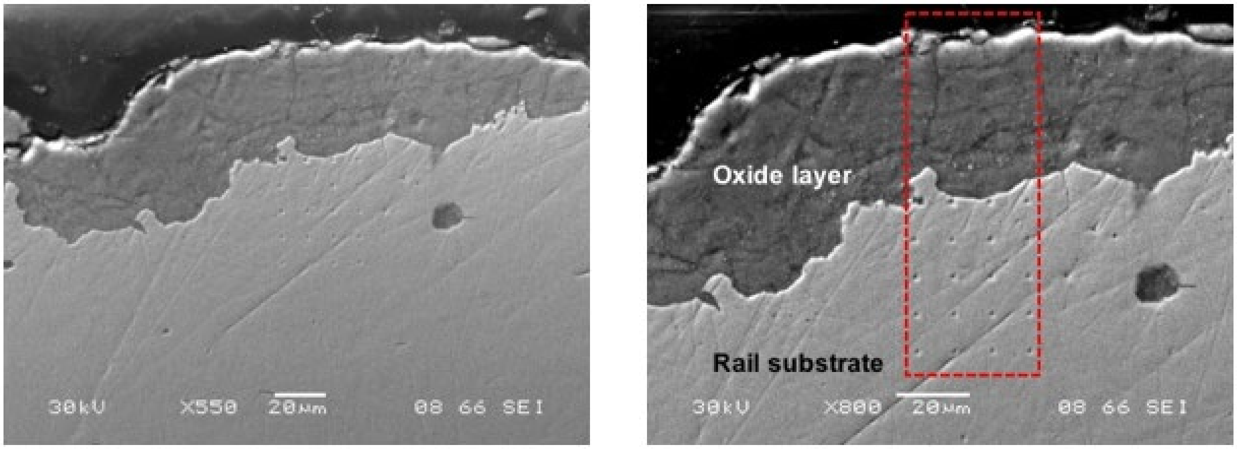

(a) SEM image (x550, 30kV)

(b) SEM image (x800, 30kV)

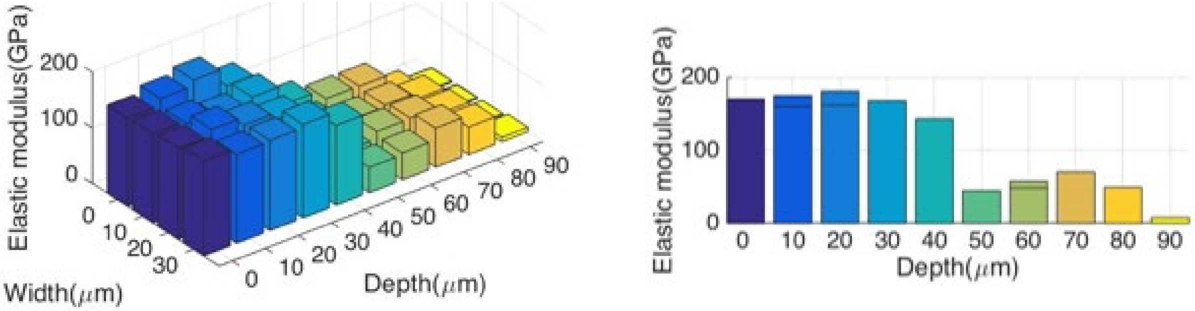

(c) Elastic modulus (Isometric view)

(d) Elastic modulus (2D view)

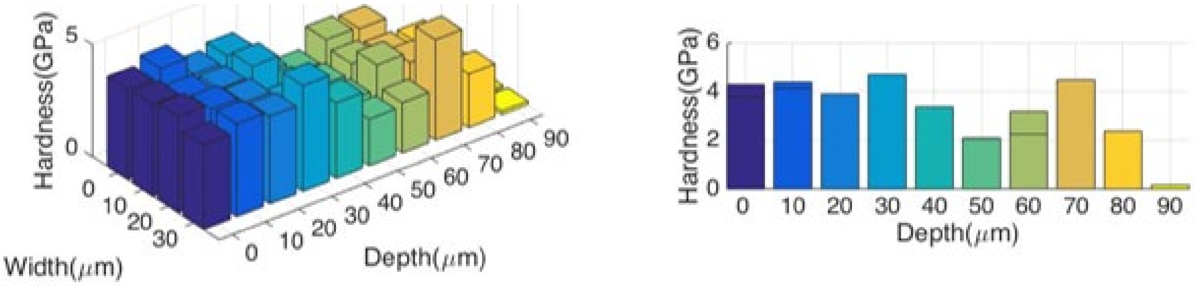

(e) Nano-hardness (Isometric view)

(f) Nano-hardness (2D view)

Figure 48. SEM images and nano-indentation results for iron hydroxide layer on 1948 rail.

2.4.5.2 *Summary of nano-indentation tests*

Nano-indentation was used to measure the mechanical properties of the iron oxide and hydroxide layers on the rails. Figure 49 and Figure 50 show the measured elastic modulus and nano-harness of the parent material and the iron oxide/hydroxide layer on the rail. The elastic modulus of the rail substrate is lower than the typical elastic modulus of rail steel because of the metal diffusion between the parent material and the iron oxide layer. When the iron oxide/hydroxide layer developed on the parent material, Fe or C ions were moved to the oxide layer from the parent material. In this progress, the elastic modulus is affected.

It is difficult to compare the elastic modulus data to the pure iron oxides because iron oxide/hydroxide layer on the rail are not a pure oxide material. The elastic modulus of gray-colored layer on the 2012 rail is 107.3 GPa, and the average of elastic modulus of brown-colored layers on the 2012, 1999 and 1948 is 45.9 GPa as shown in Table 21. The hardness of gray-colored layer is higher than the both the parent material and the brown-colored layer.

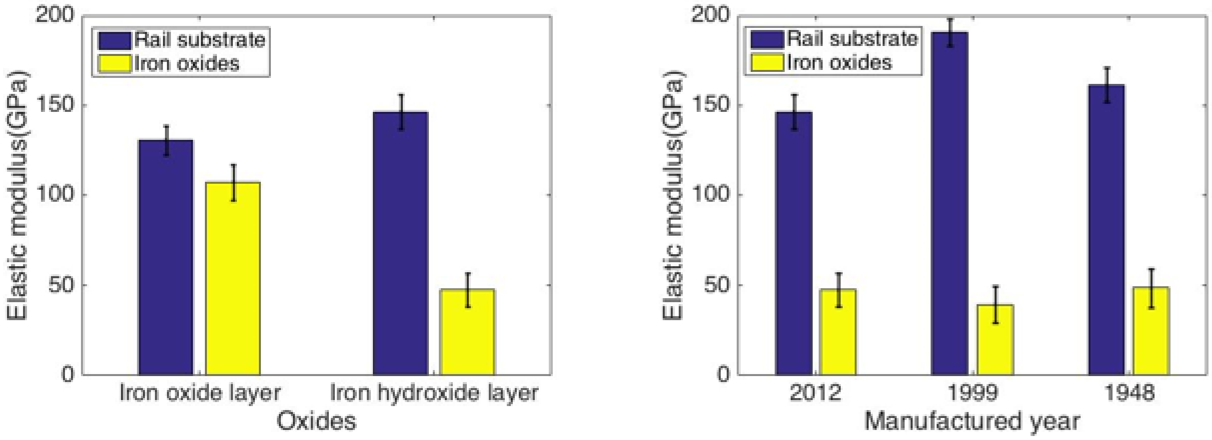

(a) 2012 rail

(b) Iron hydroxide layer

Figure 49. Elastic modulus of rail substrate and iron oxides

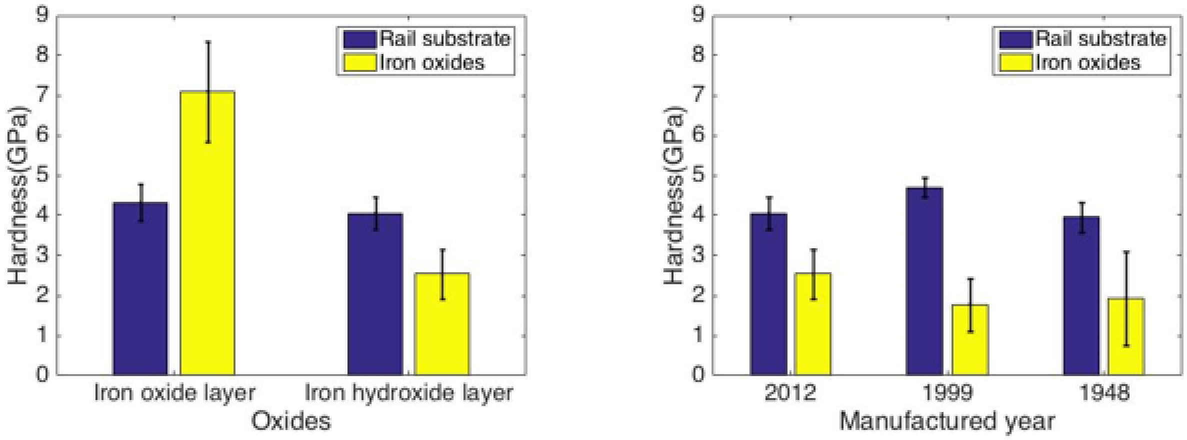

(a) 2012 rail

(b) Iron hydroxide layer

Figure 50. Hardness of rail substrate and iron oxides

Table 20. Average elastic modulus and standard deviation of parent material

	2012 rail (gray)	2012 rail (brown)	1999 rail (brown)	1948 rail (brown)
Elastic modulus (GPa)	130.8	146.4	190.8	161.5
Standard deviation (GPa)	8.2	9.6	7.5	9.6
Hardness(GPa)	4.3	4.1	4.7	4.0
Standard deviation (GPa)	0.5	0.4	0.2	0.4

Table 21. Average elastic modulus and standard deviation of iron oxide/hydroxide layers

	2012 rail (gray)	2012 rail (brown)	1999 rail (brown)	1948 rail (brown)
Elastic modulus (GPa)	107.3	48.7	39.4	49.7
Standard deviation (GPa)	10.1	9.3	10.2	10.8
Hardness(GPa)	7.1	2.5	1.8	1.9
Standard deviation (GPa)	1.3	0.6	0.7	1.2

2.5 Key findings

The 2012, 1999 and 1948 rails have two different colors on their surface, gray and brown. The different colored layers were selected to compare the chemical and mechanical features. Various material characterization techniques such as SEM, Raman spectroscopy, XRD, EDX and nano-indentation tests were carried out to confirm whether the iron oxide and hydroxide layers can be used as a passive in-situ stress sensor for railroad. The major key findings of the material characterization tests are summarized below:

Gray-colored layer

- The surface of the gray-colored layer is a mixture of Hematite (α-Fe2O3) and Magnetite (Fe3O4).
- Hematite is a material that is known to display Raman piezo-spectroscopic effect [2].
- The layer developed in a furnace has a uniform thickness of 49 µm (0.009 inches).
- However, the layer scales off over time. The layer is not seen on older rails.
- The elastic modulus of gray-colored layer is 107 GPa (15519 ksi).
- The nano-hardness of gray-colored layer is 7.1 GPa (1030 ksi), and the value is almost similar to the parent material which is rail steel.

Brown-colored layer

- The surface of the brown-colored layer is a mixture of Goethite (α-FeOOH) and Lepidocrocite (ɣ-FeOOH) initially.
- The layer grown in uncontrolled environment, and has an irregular thickness of 43 μm (0.0017 inches).
- The brown-colored layer sometimes grows on iron oxide(s) layer.
- The top layer changes over time to a non-detectable material for Raman spectroscopy and XRD.
- The elastic modulus of brown-colored layer is 46 GPa (6671 ksi).
- The nano-hardness of brown-colored layer is 2.0 GPa (290 ksi).

3. Iron Oxides; Residual Stress Measurement

3.1 Introduction

This section describes the results of the residual stress measurement of Hematite and begins by introducing the purpose of test and sample fabrication. The specification of the device used in the test is presented as well. Results from the test are discussed in the remainder of this chapter.

The iron oxide layer, mill scale, on the surface of the 2012 rail is a mixture of Hematite and Magnetite. They were grown in the furnace under controlled temperature and humidity. A thermal residual stress is induced to the layer when a cast iron is subjected to the cooling process. The Hematite has Raman piezo-spectroscopic effect as well as a measurable Raman spectrum.

It is possible to measure absolute stress of the Hematite using Raman piezo-spectroscopy as a stress-free spectrum can be obtained using the Hematite powder. In this research, the peak shift caused by thermally grown residual stress was measured using Raman piezo-spectroscopy and compared to the stress-free spectrum. The actual stress value however was not calculated.

3.2 Sample fabrication

Preliminary uniaxial compression tests were applied to A36 steels, which also has a mill scale layer on the surface, using a universal testing machine (UTM) at UCF as shown in Figure 51. To collect the Raman spectra, a portable Raman spectrometer (Ocean Optics QE Pro) was used with a 785nm laser. Figure 52(a) shows the prepared A36 sample for compression tests.

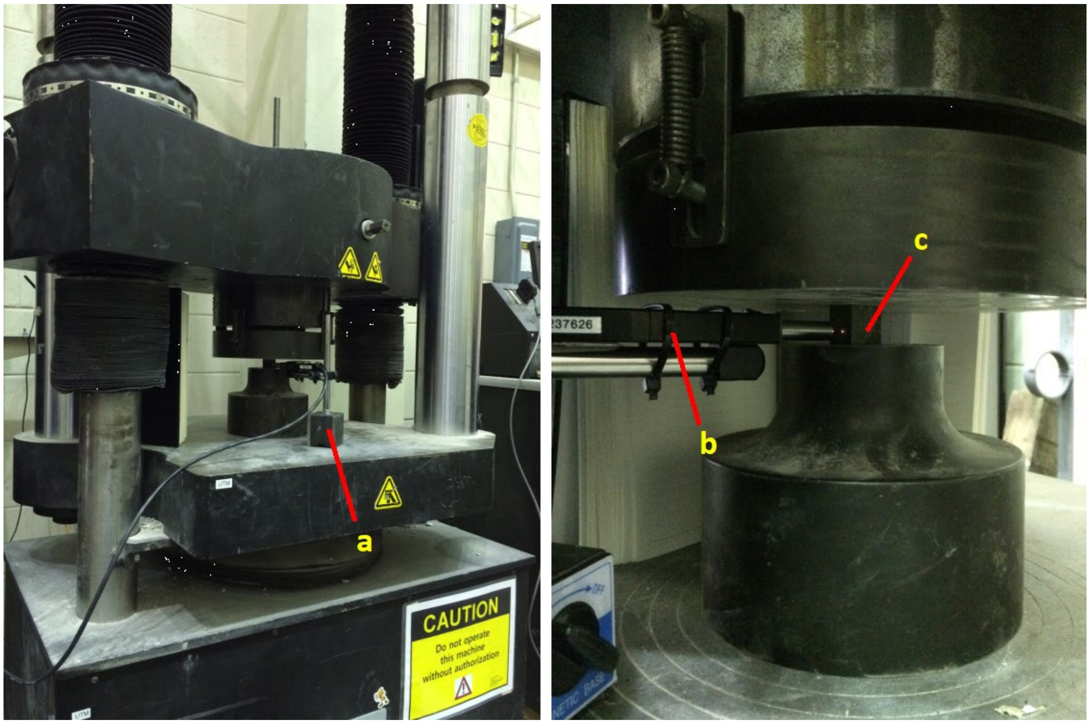

Figure 51. Loading frame at UCF (a) Probe stand; (b) Raman probe; (c) A36 steel sample.

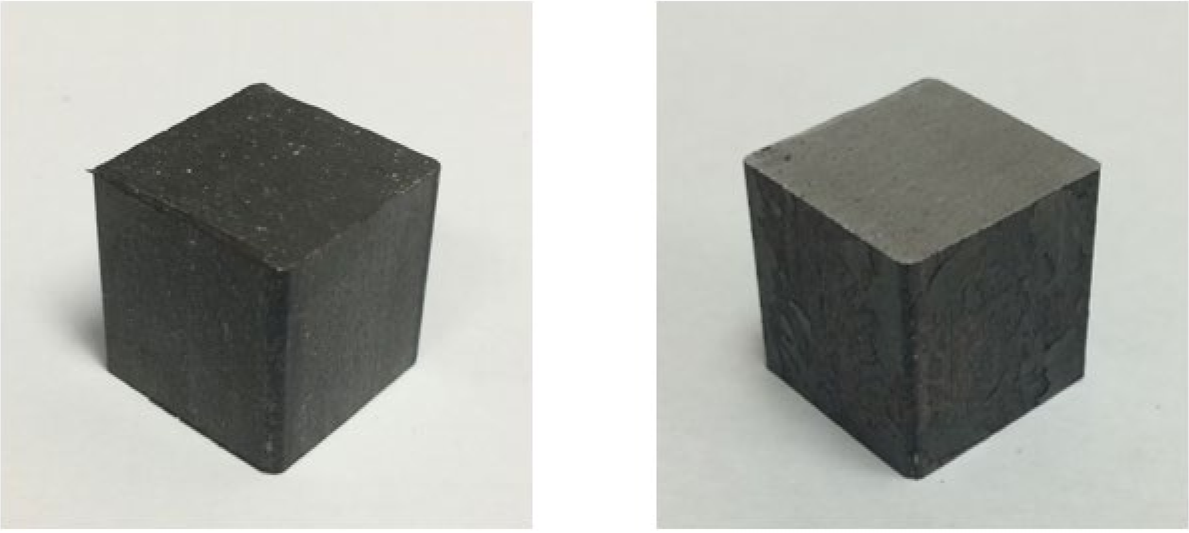
(a) Before compression test (b) After compression test

Figure 52. A36 steel samples before and after compression tests

It is found that the applied stress could not be measured through the mill scale layer using the portable Raman spectrometer, as once the compressive stress was applied to the A36 sample, the mill scale layer immediately peeled off as shown in Figure 51(b). Therefore, the thermal residual stress in the mill scale layer on the 2012 rail was only measured using Raman spectrometer in this research. The results are shown in the next chapters.

3.3 Sample preparation

The goal of the Raman piezo-spectroscopy test is to measure the thermal residual stress in the iron oxide layer on the 2012 rail. To measure the thermal residual stress in the layer, two samples were prepared in this research. As shown in Figure 53(a), sample 1 is the raw oxide layer on the surface of 2012 rail. The sample has a thermal residual stress in the layer. To prepare a stress-free sample which is sample 2, the iron oxide layer on the surface of 2012 rail was scratched out from the parent material and crushed into the powder as shown in Figure 53(b).

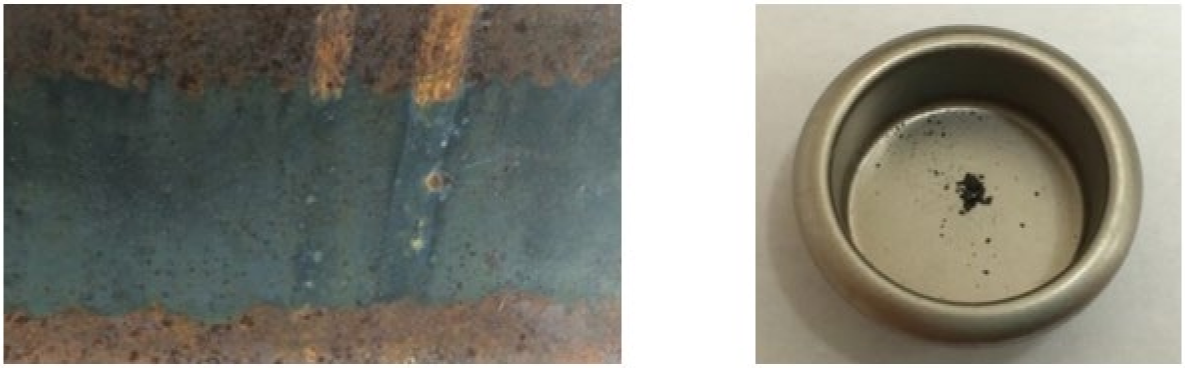
(a) Oxide layer in 2012 rail (b) Fragments of oxide layer

Figure 53. Prepared sample for measuring the residual stress in the oxide layer

3.4 Experimental setup

The Ocean Optics QE Pro is a portable system and was used with a 785nm laser. Figure 54 shows the different parts of the system, (a) commercial software for collecting Raman spectra and adjusting experimental parameters; (b) spectrometer; (c) laser generator and controller; (d) Raman probe for carrying laser signal to the target from generator and bringing the scattered signal back to the spectrometer. The measurement function of the system is shown in Table 22. To correct Raman spectra with the portable system, 785 nm multimode diode laser was used as an excitation source. The integration time of 10 seconds and accumulation of 4 times were utilized for obtaining Raman spectra. The Raman spectrometer was calibrated using the Raman peak at 520 cm-1 of a clean Si wafer.

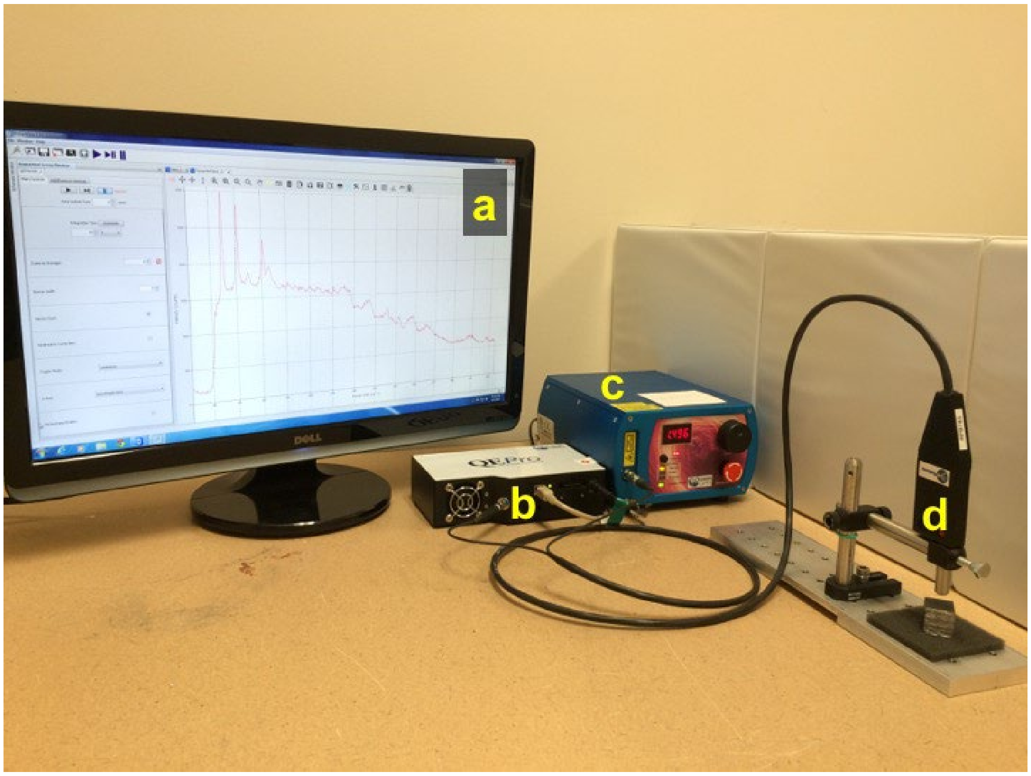

Figure 54. Portable Raman spectroscopy system at UCF (a) spectrometer control software; (b) spectrometer; (c) 785nm laser (red laser); (d) optic cable and probe.

Table 22. Measurement function of Ocean Optics QE Portable-Raman spectrometer

Item	Specification
Excitation source	785nm multimode diode laser, 499 mW output power(Max.)
Probe	Fiber length: 1.5 m, Working distance: 7.5 mm
Grating	1,200 line/mm

3.5 Stress-free Raman spectrum of α-Fe_2O_3 on the rail

To obtain the stress-free Raman spectrum of α-Fe2O3 on the rail, Ocean optics QE Pro was used with 785 nm laser. The laser was focused on the powder of the gray-colored layer for 10 seconds, and the spectra accumulated 4 times to obtain clear peaks.

Figure 55 shows the obtained raw Raman spectrum of α-Fe2O3 on the rail. To see the peak locations, pick peaking method was applied to the raw Raman spectrum. Table 23 shows the peak locations measured by using pick peaking method. It is found that the stress-free Raman spectrum of α-Fe2O3 on the rail has two clear peaks at 280.7 and 399.4 cm-1 and four more distinguishable peaks at 479.4, 596.8 and 645.8 cm-1. The stress-free spectrum was used for identifying the α-Fe2O3 and measuring the absolute residual stress levels in the iron oxide layer.

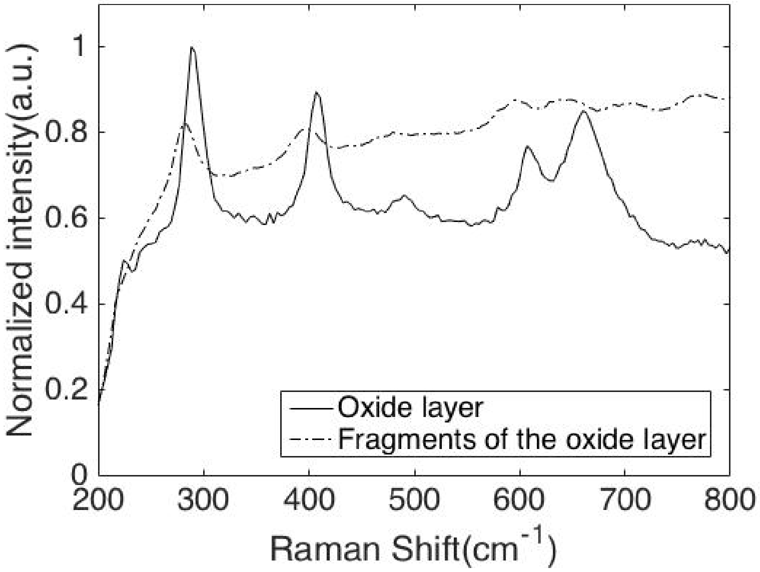

Figure 55. Raman spectra of the iron oxide layer and the fragments [10sec, 4 averaging]

Table 23. Peak locations of Raman spectra using peak-picking

Samples	Peak locations					
Fragments		280.7	399.4	479.4	596.8	645.8
Oxide layer	224.0	288.2	406.8	490.2	607.4	659.7

3.6 Residual stress measurement

The peak shift caused by thermal residual stress was measured using Raman piezo-spectroscopy. The solid and dashed line in Figure 55 show the Raman spectra of the raw iron oxide layer and stress-free powder respectively. To show the difference of peak locations in the figure, the y-axis is normalized by the highest peak intensity. As shown in Figure 55 and Table 23, the peak at 280.7 cm-1 moved to 288.2 cm-1 under the thermal residual stress. The peak at 399.4 cm-1 also moved to 406.8 cm-1. Most of the peaks moved to the right side of the stress-free peaks. It indicates that the direction of the thermal residual stress is compressive stress. The estimated stress direction using Raman piezo-spectroscopy is well matched with the SEM results of the

2012 rail. As shown in Figure 56, there are many of vertical furrows on the surface of the iron oxide caused by the compressive stress.

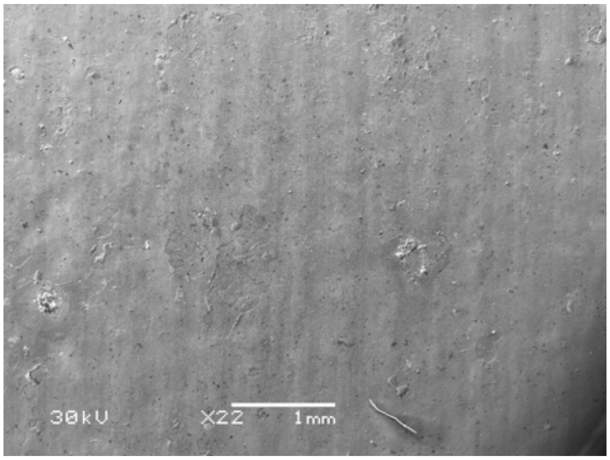

Figure 56. SEM image on the surface of iron oxide layer

3.7 Key findings

In this research, it is found that mechanically applied stresses cannot be measured through the mill scale layer using a portable Raman spectrometer, as once the minimum compressive stress that can be detected by the portable Raman spectrometer was applied to the steel sample, the mill scale layer immediately peeled off from the parent material.

Although the applied stresses are not measurable by portable Raman spectrometer, the presence of thermal residual stress in iron oxide layer can be detected using portable Raman spectrometer. However, a high-resolution Raman spectrometer is needed to accurately measure the stresses.

3.8 Conclusion

The objectives were to investigate the feasibility of Raman piezo-spectroscopy as a mobile method to measure absolute stress. The conclusion of this research is as follows:

- It was observed that the existence of the iron oxides (hematite, magneite) and hydroxides(goethite, lepidocrocite) which are Raman sensitive materials, on rail surface in a series of material characterization tests for three rail samples manufactured in 1948, 1999, and 2012.
- It was found that the hematite can be used to measure thermal residual stress that is induced when the hematite layer is formed on rail surface during air quenching after milling at a high temperature. However, the hematite layer is gradually scaled off over time, using hematite may not be practically feasible. We do not recommend using Hematite as a passive stress sensor.
- The detectability of goethite and lepidocrocite on rail surface decreased for older rail. Also, the goethite and lepidocrocite layers are not mechanically stable due to scaling off (i.e., rusting). In addition, their growth is largely dependent on environmental conditions. Thus, it is not feasible to use goethite and lepidocrocite as a passive sensor.

4. Aluminum Oxide; Absolute Stress Measurement in Thermite Welding

4.1 Introduction

Thermite welding, also known as exothermic welding, is a wide-gap welding technique, filling the gap between rail ends with cast iron. In thermite welding process, highly reactive fine aluminum powder reduces the oxide of iron oxide, by producing high temperatures up to 3500 °F (2000 °C).

$$Fe_2O_3 + 2Al \rightarrow 2\,Fe + Al_2O_3 + 181.5\,kcal$$

The reaction produces iron (Fe) and slag (Al_2O_3). The alumina compounds have excellent sensitivity for fluorescence spectroscopy. Particularly, α-Alumina, which is α-Al_2O_3, is one of most sensitive materials in fluorescence spectroscopy. Using the fluorescence spectrometer, which is the same as the Raman spectrometer, α-Al_2O_3 has two fingerprint peaks at 14402 cm^{-1} for R_1 and 14432 cm^{-1} for R_2 as shown in Figure 57. When α-Al_2O_3 is subjected to stress, the peaks move horizontally depending on stress direction[6] [7]. The relationship between the peak shift and stress magnitude can be determined in a laboratory, and the slope of the relationship is called piezo-spectroscopic coefficient. Piezo-spectroscopic characteristics of α-Al_2O_3 is well established in literature.

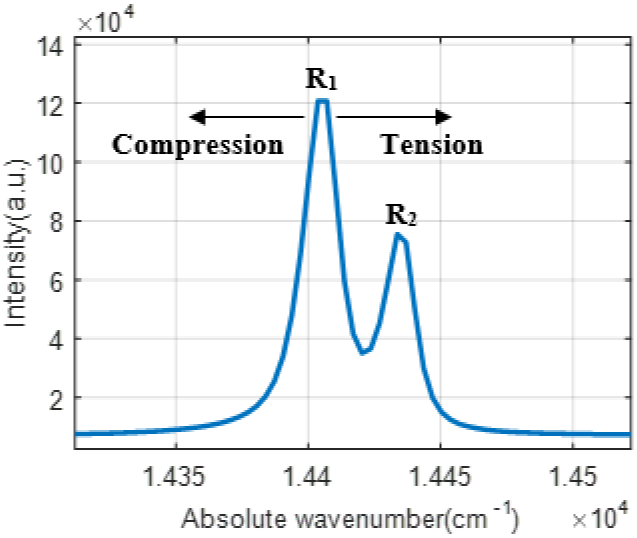

Figure 57. Typical fluorescence spectrum of α-Al_2O_3.

In this research, it was observed that the existence of α-Al_2O_3 on the surface and the inside of thermite weld metal and heat affected zone (HAZ). In addition, compression tests were carried out to the thermite weld steel to confirm whether the thermite weld metal can be used as a passive in-situ stress sensor for railroad.

4.2 Sample fabrication

Two thermite welded rail samples (Figure 58) were prepared by cutting 8 inches of the entire rail. One sample is a 136RE AREMA rail and has a nominal weight of 136 lbs/yd and is 7-5/16” tall. The other sample, 141RE AREMA, has a nominal weight of 141 lb/yd and is 7-7/16” tall. The rail samples are named 136 RE rail and 141 RE rail based on the nominal weight for the sake of convenience in this report.

(a) 136 RE rail

(b) 141 RE rail

Figure 58. Photographs of thermite welded rails.

136 RE rail was used for obtaining 2D/3D alumina map from the surface without any surface treatment. 141 RE rail was used for obtaining 2D alumina map from the inside of the rail and mechanical test. To obtain fluorescence spectra from the inside of the 141 RE rail, the rail was prepared by cutting the rail into two halves using a band saw machine at UCF as shown in Figure 59(a)-(b). To reduce the heat effect caused by the high-speed blade, the sample was prepared using low-speed cutting with excess coolant. Figure 59(c) shows the cross-section of the 141 RE rail right after the cutting. There are lots of grooves on the surface of the cutting plane created by rail cutting. To reduce the accumulation of alumina and other on the grooves, milling process was performed to the surface of cut rail. Figure 59(d) shows the prepared rail sample using rail cutting and milling process. The horizontal lines on the cutting plane show the path of cutter on milling machine.

(a) Band saw machine at UCF

(b) Rail cutting

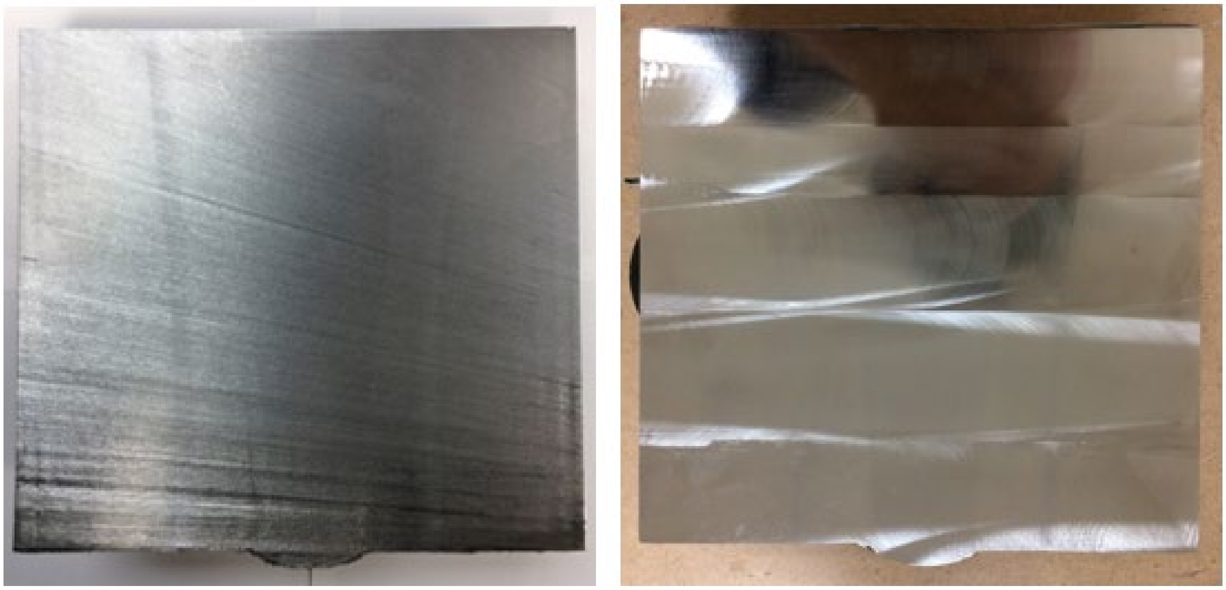

(c) Before milling process

(d) After milling process

Figure 59. Sample fabrication of 141 RE rail for 2D/3D Al_2O_3 mapping.

Figure 60 shows the prepared rail sample of 141 RE rail for mechanical test. To perform a compressive loading test, the thermite weld was cut into thirty-two samples and polished. The sample dimensions are roughly 1” x 0.5” x 0.5”.

(a) Entire rail samples

(b) A prepared rail sample

Figure 60. Sample fabrication of 141 RE rail for mechanical test

4.3 Mapping

The following sections describe the tools, process, and results of the fluorescence spectrum mapping effort.

4.3.1 *Automated system development*

A 3-dimensional motorized translation device was assembled to yield a finely spaced alumina map on the rail surface. Figure 61 and Table 24 show the pictures and specification of the motorized translation device, spectrometer and excitation source. A LabVIEW-based code was developed for controlling the translation stage and spectrometer as shown in Figure 62. The translation device and spectrometer can be controlled by changing parameters such as dimension of map, integration time, and accumulation time, etc.

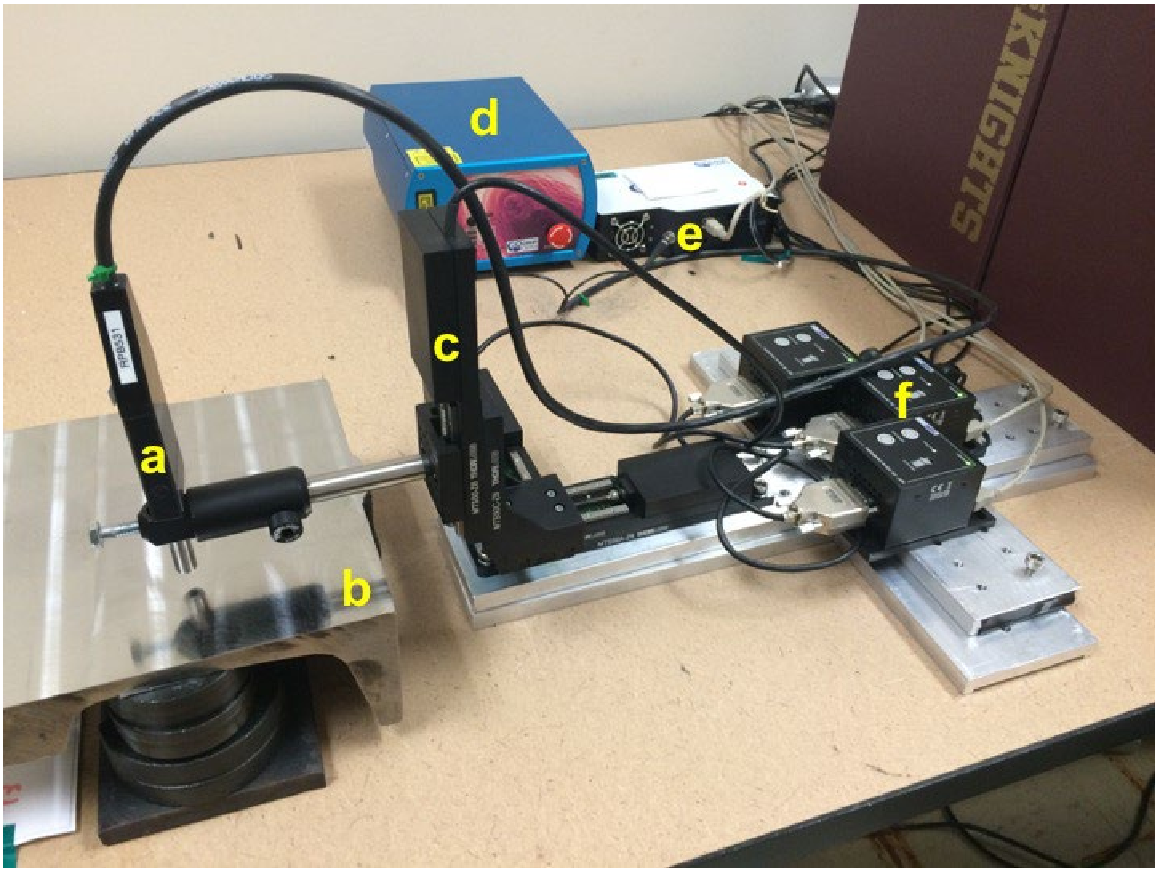

Figure 61. 3D stage combined with portable spectroscopy system at UCF (a) probe; (b) sample; (c) translation stage; (d) laser (red laser); (e) spectrometer; (f) controller.

Table 24. Specification of automated system

Item	Specification
Translation stage	50 mm travel range, 0.05 μm minimum incremental movement
Excitation source	785nm multimode diode laser, 499 mW output power(Max.)
Spectrometer	1,200 line/mm

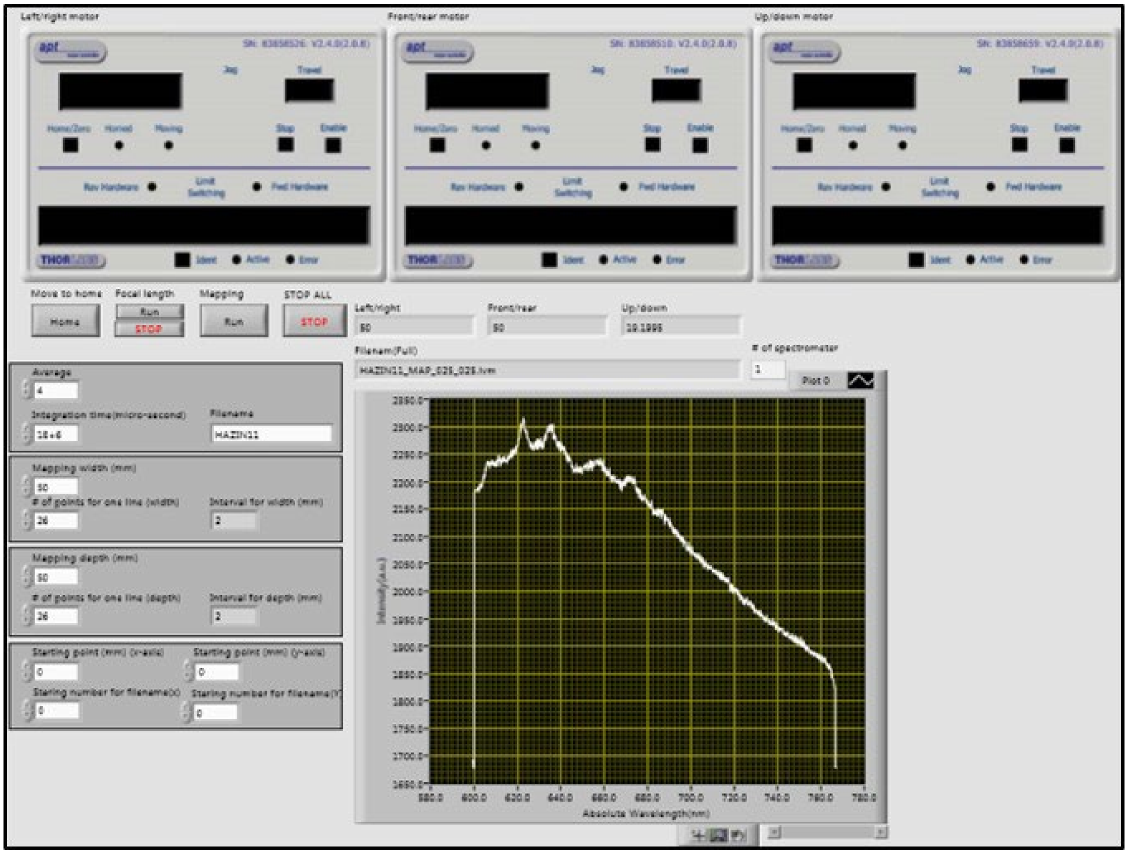

Left/right: 50
Front/rear: 50
Up/down: 19.1995
Filenam(Full): HAZIN11_MAP_025_025.lvm
# of spectrometer: 1
Average: 4
Integration time(micro-second): 1E+6
Filename: HAZIN11
Mapping width (mm): 50
# of points for one line (width): 26
Interval for width (mm): 2
Mapping depth (mm): 50
# of points for one line (depth): 26
Interval for depth (mm): 2
Starting point (mm) (x-axis): 0
Starting point (mm) (y-axis): 0
Staring number for filename(X): 0
Staring number for filename(Y): 0

Developed Graphic User Interface (front panel)

Figure 62. LabVIEW-based user's screen for controlling translation stage and spectrometer.

4.3.2 Background correction

Figure 63(a) shows a typical example of obtained fluorescence spectrum of alumina in the thermite welded zone. It is hard to distinguish the location of alumina peaks using the raw spectrum as the background level is very high when compared to the intensities of alumina peaks. Therefore, background correction is required for obtaining clear peaks on the spectra. Asymmetric truncated quadratic function is applied to estimate the background of the raw spectra. Figure 63 shows the procedure of background correction. After removing the background spectrum, two alumina peaks are distinguished and compared with the stress-free alumina spectrum.

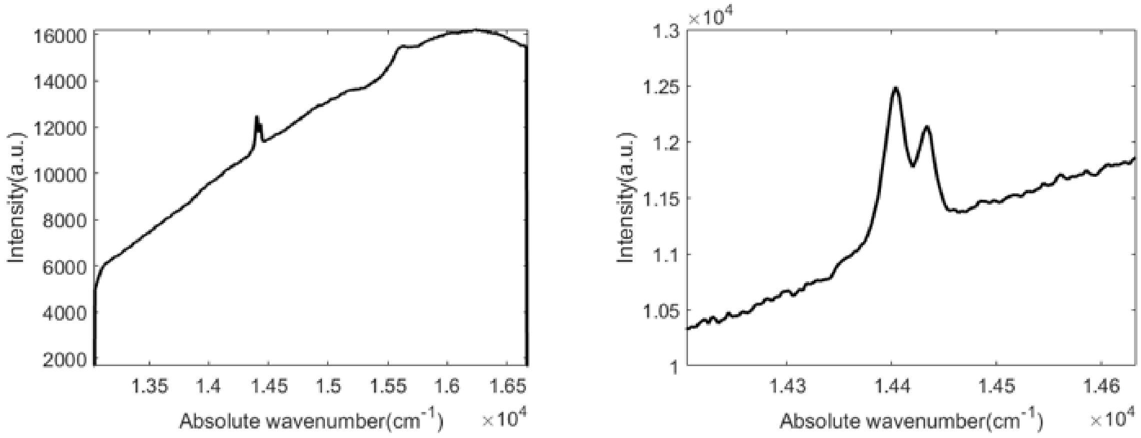

(a) Raw spectrum (b) Zoomed in spectrum

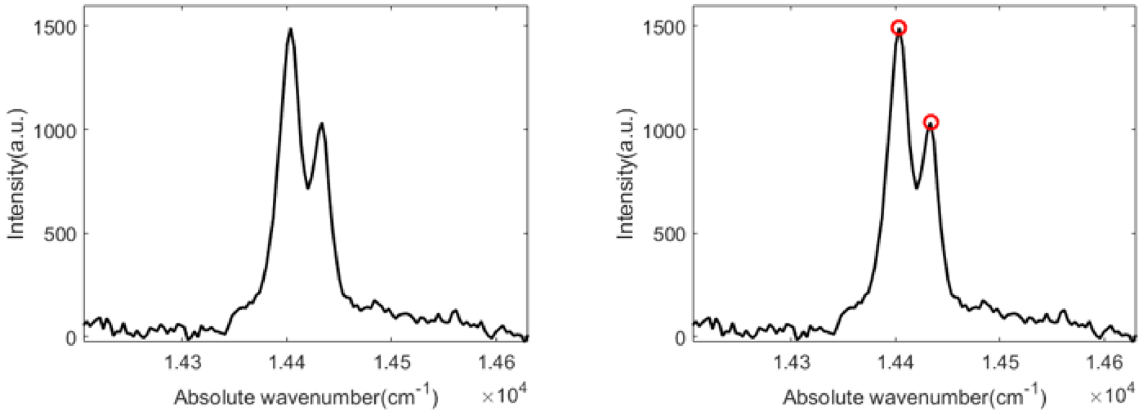

(c) After background correction (d) Finding peaks

Figure 63. Procedure used for background correction and peak finding.

4.3.3 2D and 3D maps- Outside surface of Rail

To observe the distribution of α-Alumina on the surface of the thermite welded rail, fluorescence spectra were collected from the rail head/web/foot using the developed automation system without any surface treatment. α-Alumina intensity map then was drawn and overlapped on the photograph of 136 RE rail as shown in Figure 65, Figure 66, Figure 67, and Figure 68. The color is determined by the signal-to-noise ratio of α-Alumina. In the maps, red color and blue color show the high and low-concentration of α-Alumina near the spot respectively. No-color shows no α-Alumina near the spot. Based on the obtained 2D maps, it is found that the rail head, web and foot have α-Alumina on the surface. Particularly, α-Alumina is highly concentrated on the border between weld metal and heat-affected zone (HAZ) as shown in Figure 67.

3D intensity map of α-Alumina is drawn using the obtained 2D maps. The color is determined by the signal-to-noise ratio of α-Alumina. Based on the 3D intensity map, α-Alumina is highly concentrated on the border between weld metal and HAZ.

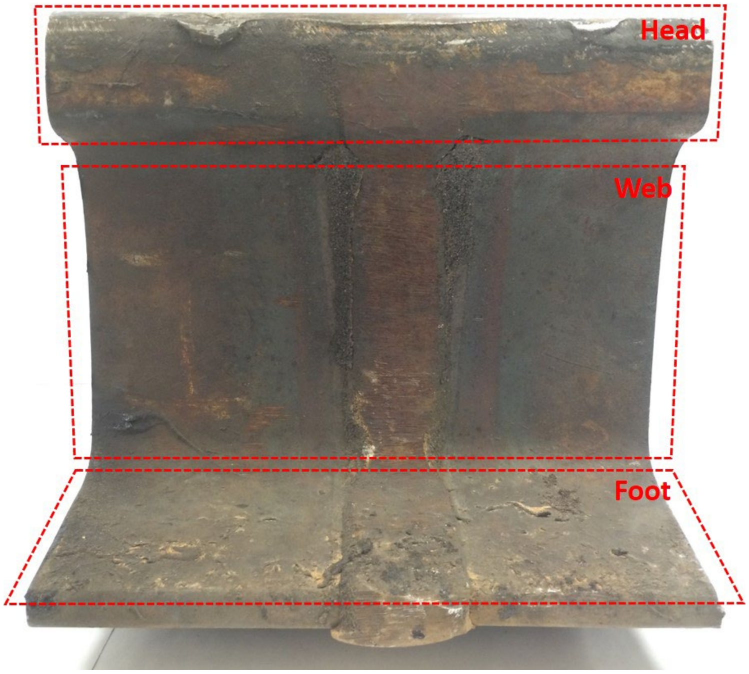

Figure 64. 136 RE rail.

Figure 65. 2D intensity map of α-Al_2O_3 on the rail head (top view)

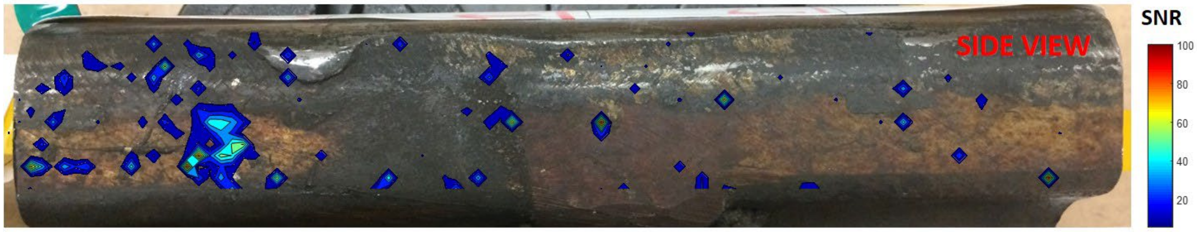

Figure 66. 2D intensity map of α-Al_2O_3 on the rail head (side view).

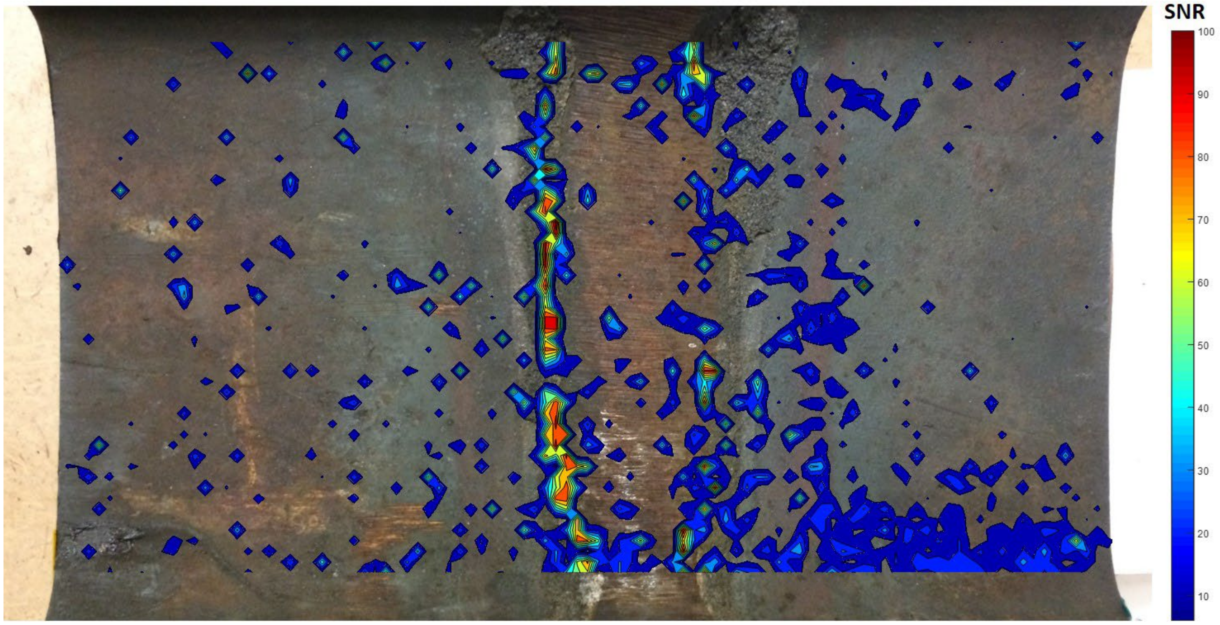

Figure 67. 2D intensity map of α-Al_2O_3 on the rail web.

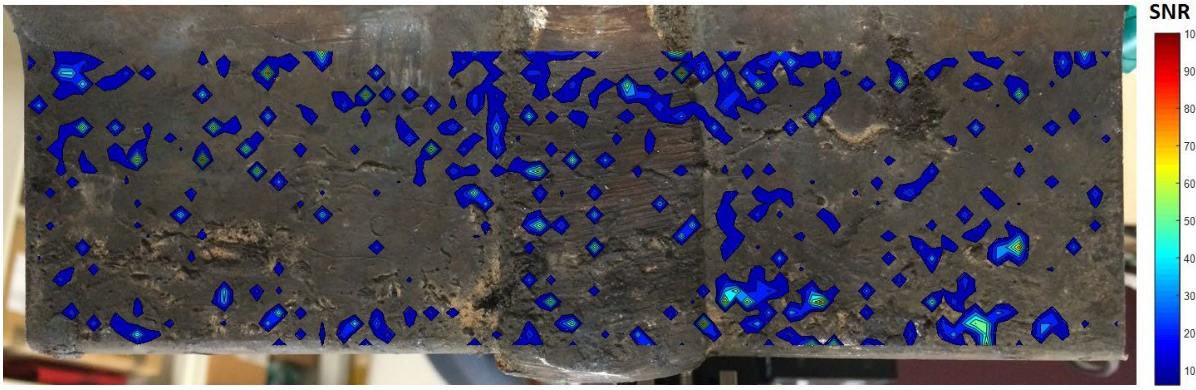

Figure 68. 2D intensity map of α-Al_2O_3 on the rail foot.

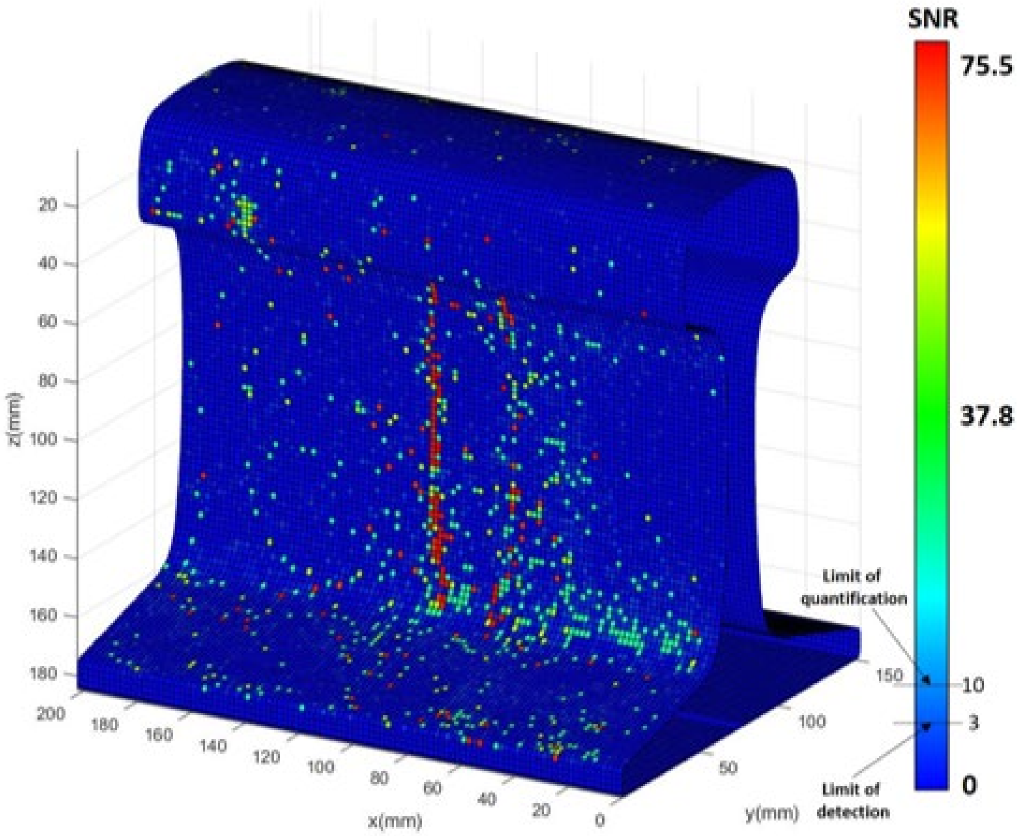

(a) 3D map of α-Al_2O_3

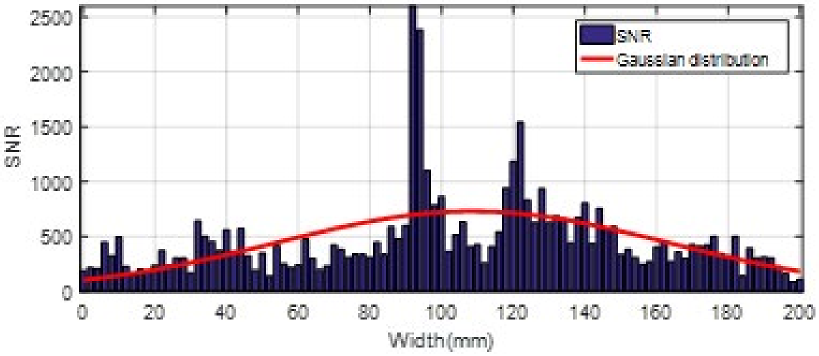

(b) Gaussian distribution of α-Al_2O_3

Figure 69. 3D intensity map of α-Al_2O_3 on the surface.

Based on the piezo-spectroscopic phenomena of α-Alumina, the stress levels were roughly calculated as shown in the Figure 70. The color is determined by the signal-to-noise ratio of α-Alumina. In the maps, red color and blue color show the compressive and tensile stress of α-Alumina near the spot respectively. Gray color shows no α-Alumina on the spot.

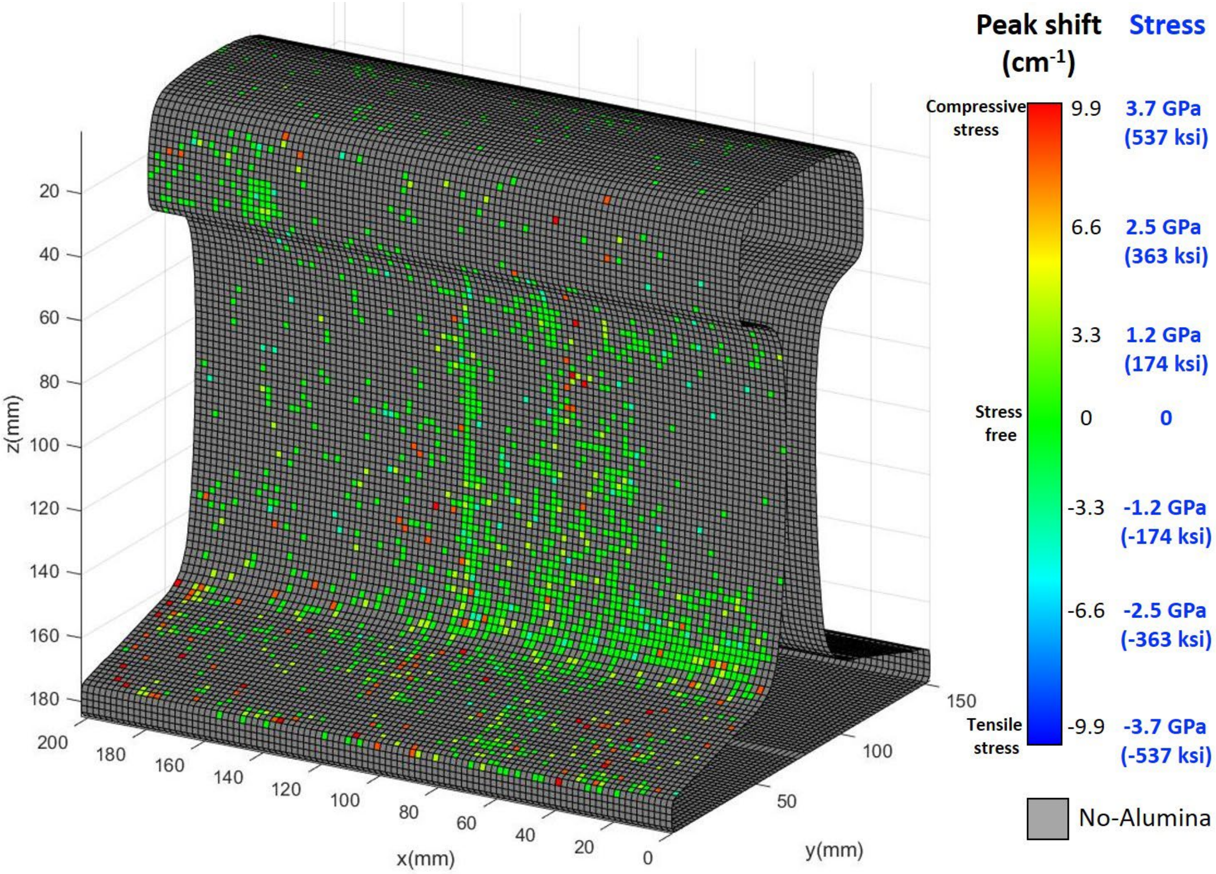

Figure 70. 3D stress map of α-Al_2O_3 on the surface.

4.3.4 2D and 3D maps- Inside surface of rail

To observe the distribution of α-Alumina inside the thermite welded rail, fluorescence spectra were collected using the developed automation system, and α-Alumina 2D map is drawn on the photo of the cutting plane of 141 RE rail (Figure 71). The color is determined by the signal-to-noise ratio of α-Alumina. In the maps, red color and blue color show the high and low-concentration of α-Alumina near the spot respectively. No-color shows no α-Alumina on the spot.

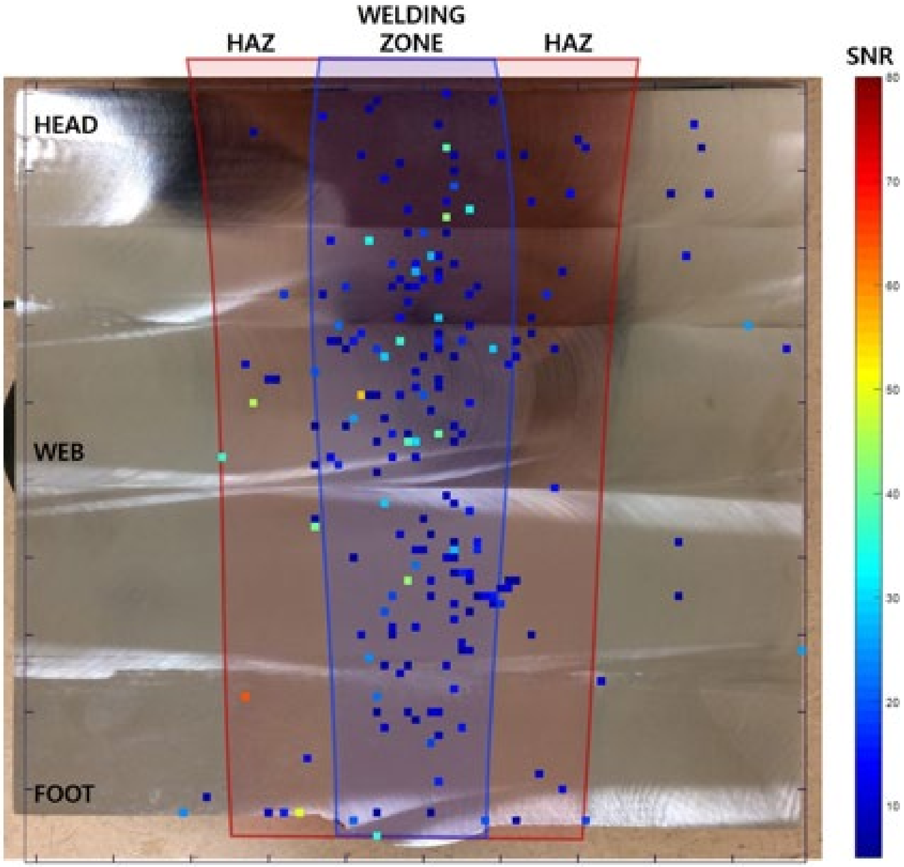

(a) 2D map of α-Al_2O_3

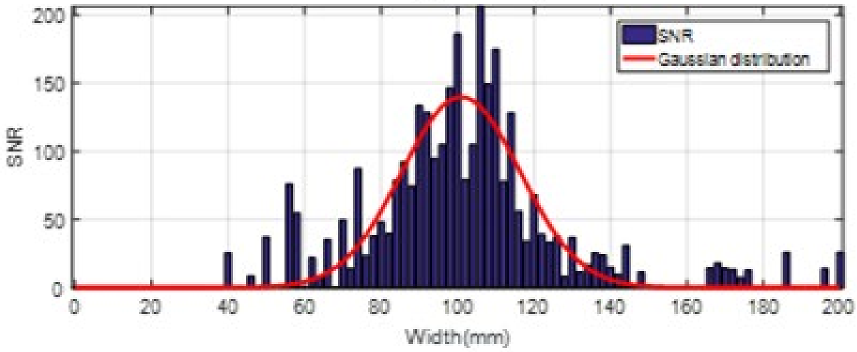

(b) Gaussian distribution of α-Al_2O_3

Figure 71. 2D map and ratio of α-Al_2O_3 inside the exothermic weld portion of the rail.

4.4 Determination of the Stress-Free State

One of the advantages of the proposed method is that the absolute stress in the target material can be measured. the stress-free spectrum can be obtained from the powder form of the target material. The stress-free fluorescence spectrum was obtained from the powder of α-Al_2O_3 in the slag layer of the thermite weld. Figure 72 shows the photographs of the slag layer on the thermite weld joint and the powder form of the layer, which is prepared by grinding the slag layer.

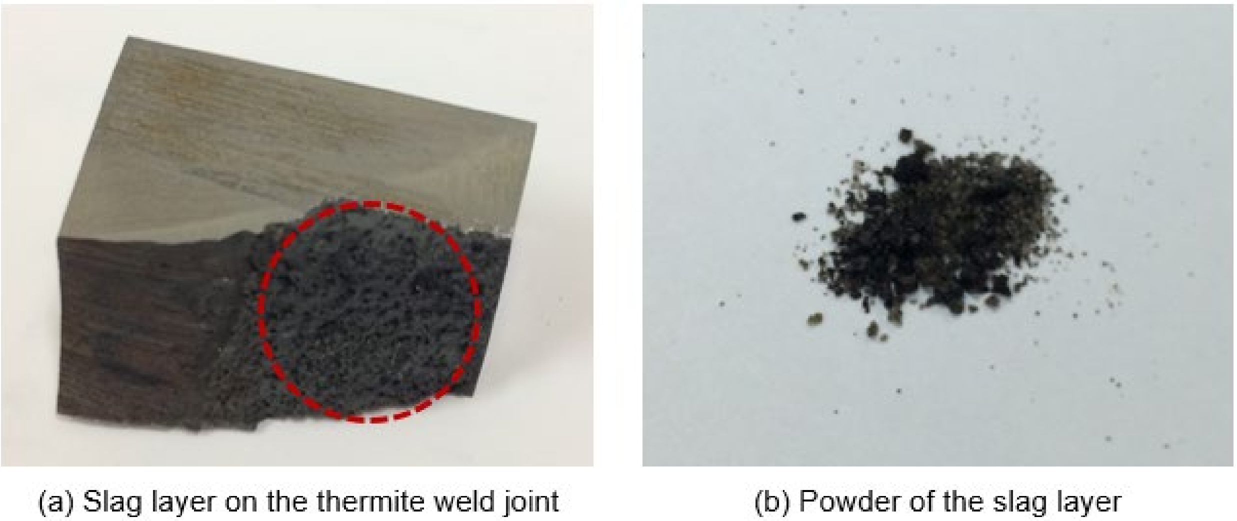
(a) Slag layer on the thermite weld joint (b) Powder of the slag layer

Figure 72. Prepared sample for determination of the stress-free state of α-Al_2O_3 in thermite weld zone

4.4.1 Stress-free fluorescence spectrum of α-Al_2O_3 in the slag layer

To obtain the stress-free spectrum of α-Al2O3 in thermite weld zone, Ocean optics QE Pro was used with 785 nm laser. The laser was focused on the powder of the slag layer for 10 seconds to obtain clear peaks.

Figure 73 shows the raw fluorescence and de-convoluted spectra of α-Al2O3 in thermite weld zone. To see the peak locations precisely, a curve fitting method was applied to the raw fluorescence spectrum using Lorentzian curves as shown in Figure 73(c)-(d). The background level was corrected, and the R1 and R2 peaks of α-Al2O3 were fit using two Lorentzian curves. Table 25 shows the peak locations calculated by using pick peaking and curve fitting methods. It is found that the stress-free fluorescence spectrum of α-Al2O3 in thermite weld zone has two clear peaks at 14405.4 and 14435.4 cm-1. The stress-free spectrum was used for identifying the α-Al2O3 and measuring the absolute stress levels in thermite weld zone.

Table 25. Peak locations of fluorescence spectra for α-Al_2O_3 in the slag powder

Method	R_1	R_2
Pick peaking	14407.0140 cm^{-1}	14436.9350 cm^{-1}
Curve fitting	14405.4036 cm^{-1}	14435.3748 cm^{-1}

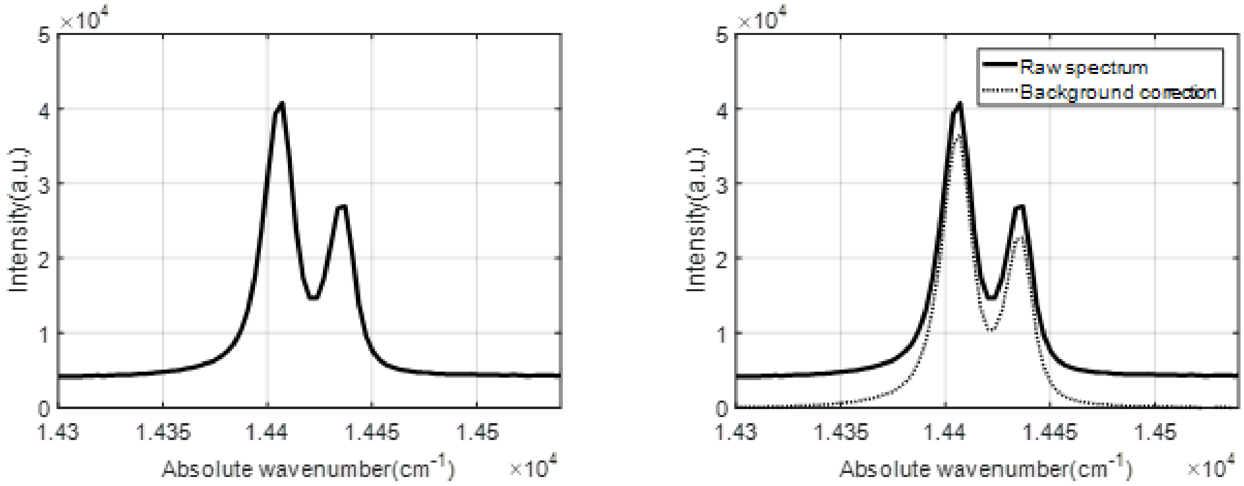

(a) Raw fluorescence spectrum of Al_2O_3 (b) Background correction

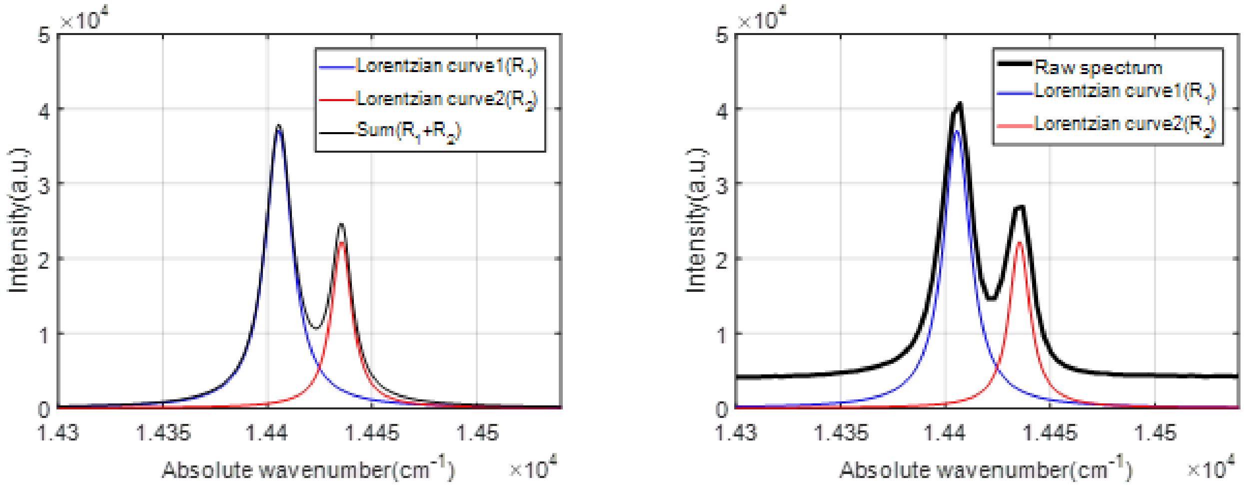

(c) Convolution curve fitting (d) Curve fitted fluorescence spectrum

Figure 73. Raw and deconvoluted fluorescence spectra of α-Al_2O_3 in the slag powder

4.5 Compression test

Uniaxial compression tests were applied using a universal testing machine (UTM) at UCF as shown in Figure 74. To hold the probe and adjust the focal length, a manual translation stage manufactured by Thorlabs was used during the tests. Figure 75 shows the schematic design of the uniaxial compression test.

Most of the α-Al_2O_3 are distributed inside the thermite weld zone as shown in Figure 71. Figure 76(b)-(c) show the prepared sample 1 and 2 cut from the thermite weld zone. Using those samples, two compression tests were performed to verify whether the thermite weld zone can be used as a stress sensor or not.

The stress-peak shift curves obtained from compression tests were compared to each other, and the piezo-spectroscopic coefficient were calculated based on the compression test results.

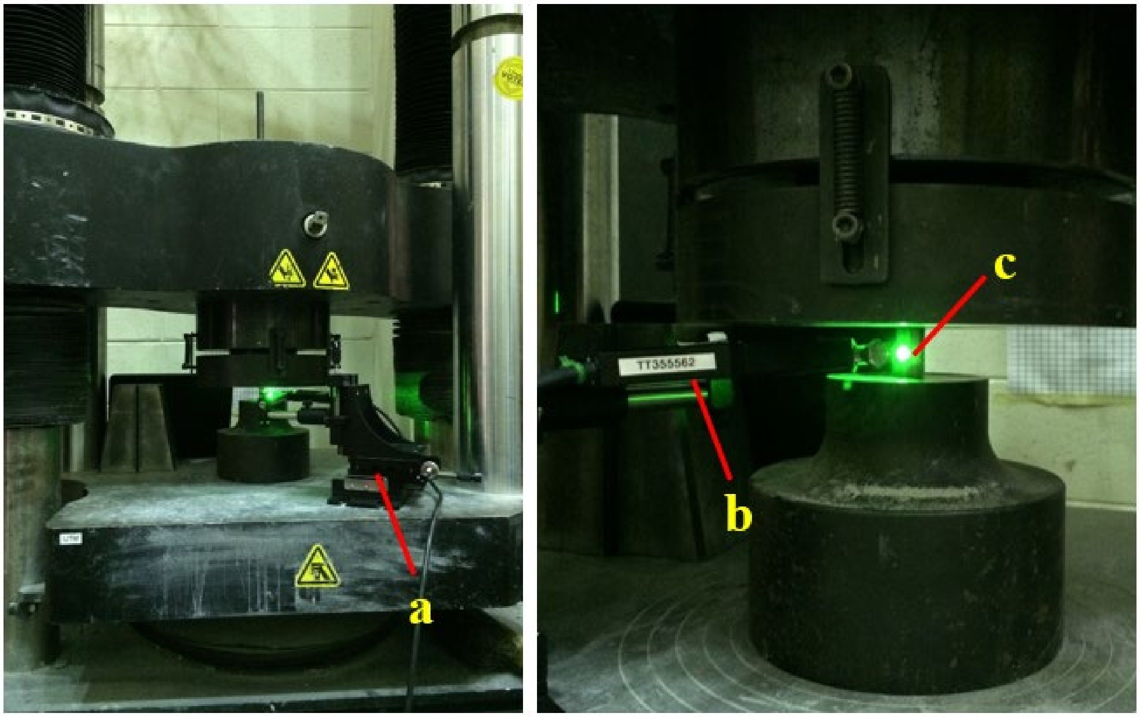

Figure 74. Loading frame at UCF (a) Translation stage; (b) Probe; (c) Weld sample.

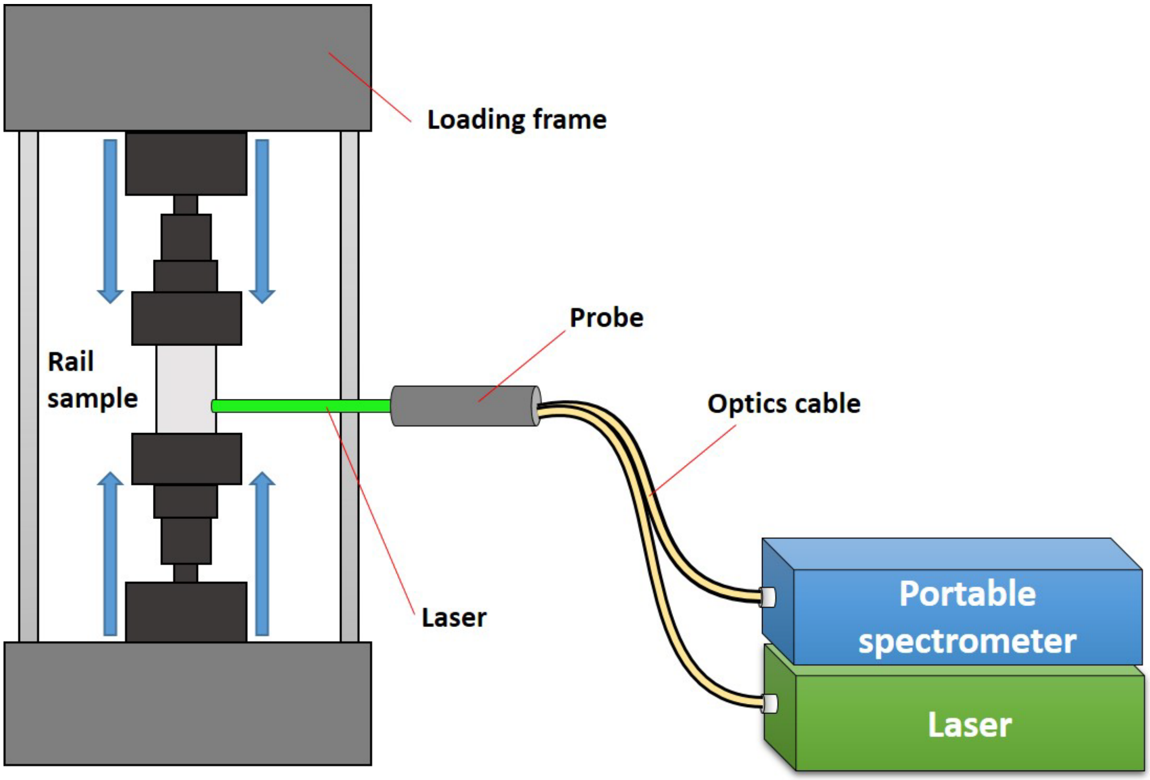

Figure 75. Schematic design of uniaxial compression test.

(a) Sample for mechanical test

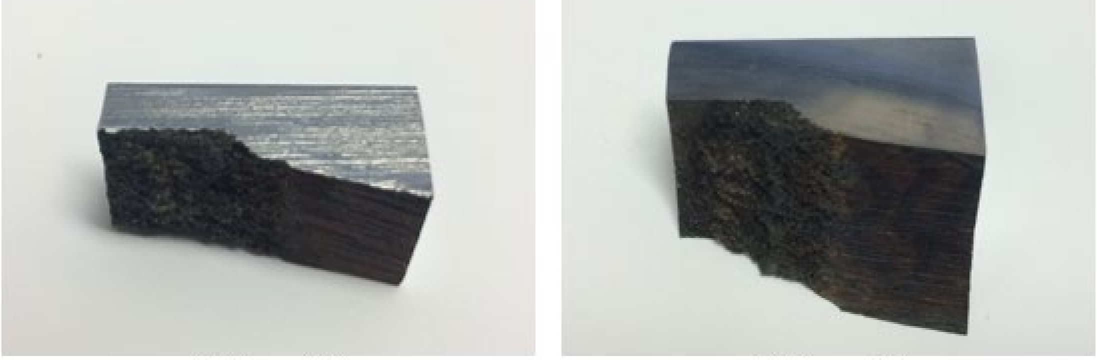

(b) Sample 1

(c) Sample 2

Figure 76. Test samples for uniaxial compression test.

4.5.1 Compression Test 1

A uniaxial compression test was performed to verify whether the thermite weld zone can be used as a passive in-situ stress sensor.

Table 26 shows the loading conditions and the estimated peak shifts under the different loading conditions. The compression test was stopped when the sample yielded.

Table 26. Applied forces and estimated peak shifts for compression test 1.

#	Force (kips)	Estimated stress (ksi)	Estimated stress (MPa)	Estimated peak shift (cm-1)
1	0	0	0	0
2	1	5.5	38.0	0.1
3	2	11.0	76.0	0.2
4	3	16.5	114.0	0.3
5	4	22.1	152.0	0.4
6	5	27.6	190.0	0.5
7	6	33.1	228.1	0.6
8	7	38.6	266.1	0.7
9	8	44.1	304.1	0.8
10	9	49.6	342.1	0.9
11	10	55.1	380.1	1.0
12	11	60.6	418.1	1.1
13	12	66.2	456.1	1.2
14	13	71.7	494.1	1.3
15	14	77.2	532.1	1.4
16	15	82.7	570.1	1.5
17	16	88.2	608.1	1.6
18	17	93.7	646.1	1.7
19	18	99.2	684.2	1.8
20	19	104.7	722.2	1.9
21	20	110.3	760.2	2.0

Pure α-Al_2O_3 and α-Al_2O_3 in a composite material have different piezo-spectroscopic coefficients. The thermite welding steel is a composite material formed by combining iron, aluminum oxide and others. Therefore, the piezo-spectroscopic coefficient of α-Al_2O_3 in thermite welding needs to be measured experimentally. In this research, the piezo-spectroscopic coefficient of 2.65 cm^{-1}/GPa was used to calculate the stress using the peak shifts under different loading condition. The average cross-sectional area of 117mm^2 (0.18 in^2) was used to calculate the stresses as well. It was expected that the peak shift of 1.8 cm^{-1} was induced under the 100 ksi.

Figure 77 shows the photographs of sample 2 under different loading conditions. As shown in figure, the upper plate of UTM came down at 100 ksi, as the sample 1 yielded. Figure 78 shows the obtained raw fluorescence spectra under different loading conditions. The black and red line show the fluorescence spectra under 0 and 78 ksi respectively. Although the pick shifts of R_1 and R_2 were measured using pick peaking method, it is hard to measure the accurate peak shifts using peak-picking method because of the limited spectral resolution of the spectrometer. To see the peak shift precisely, a curve fitting method was applied to the raw fluorescence spectra using Lorentzian curves as shown in Figure 73. First, the background correction was carried out, and then the R_1 and R_2 peaks were fitted using Lorentzian curves. After that, the peak shifts were measured based on the location of the Lorentzian curves as shown in Figure 79.

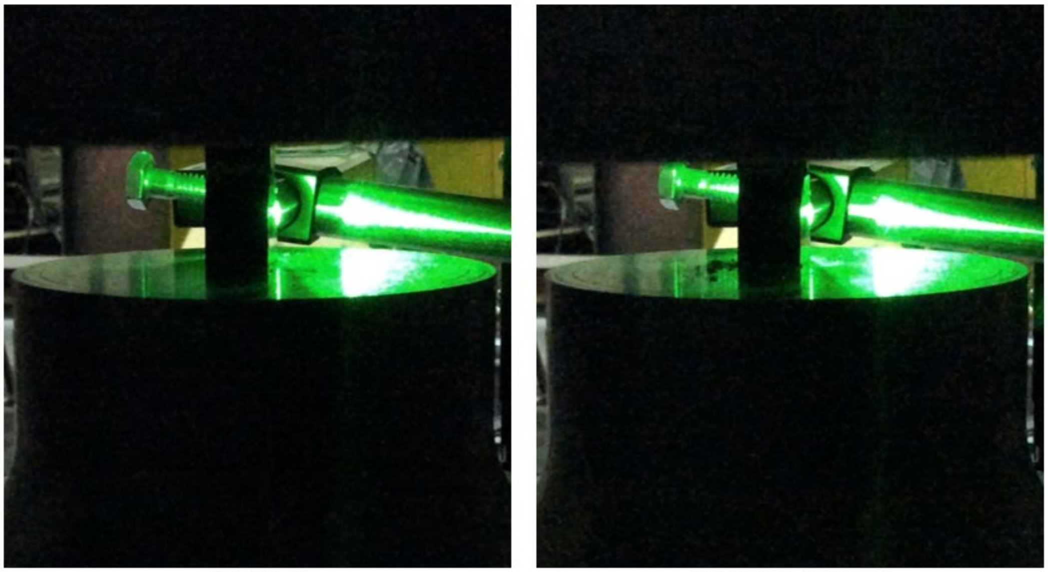

(a) 0 ksi (b) 100 ksi (yield)

Figure 77. Photographs under different loading conditions for test 1.

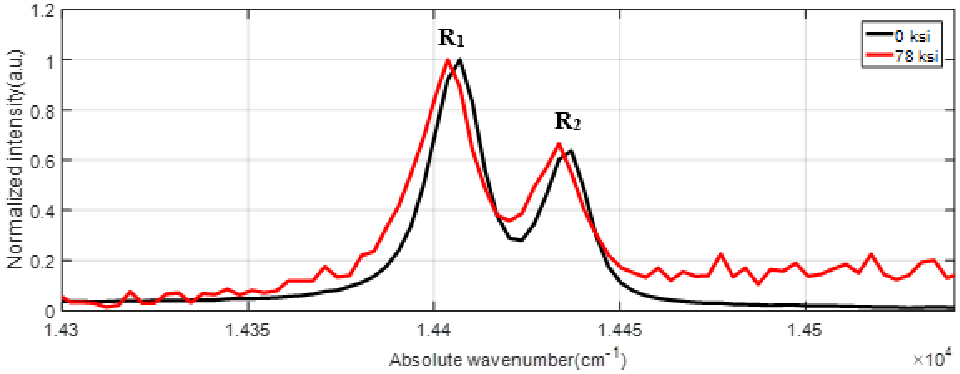

(a) Peak shifts of α-Al_2O_3 fluorescence spectra

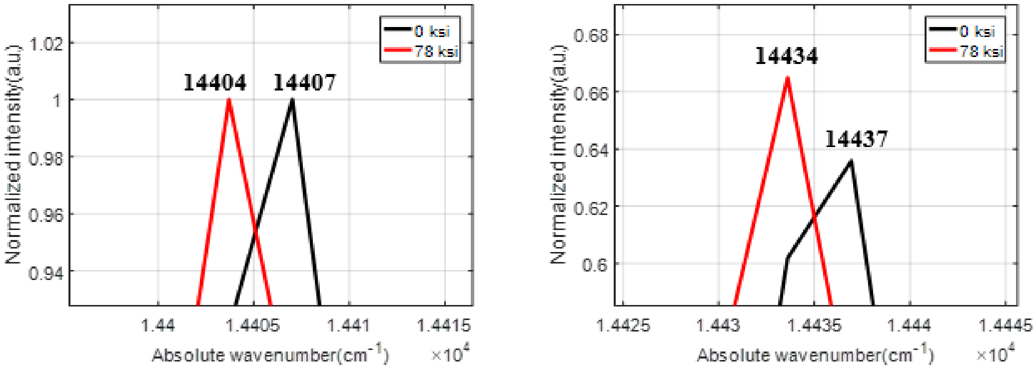

(b) Peak shift of R_1 line (c) Peak shift of R_2 line

Figure 78. Peak shift measurement of α-Al_2O_3 in thermite weld using pick peaking method.

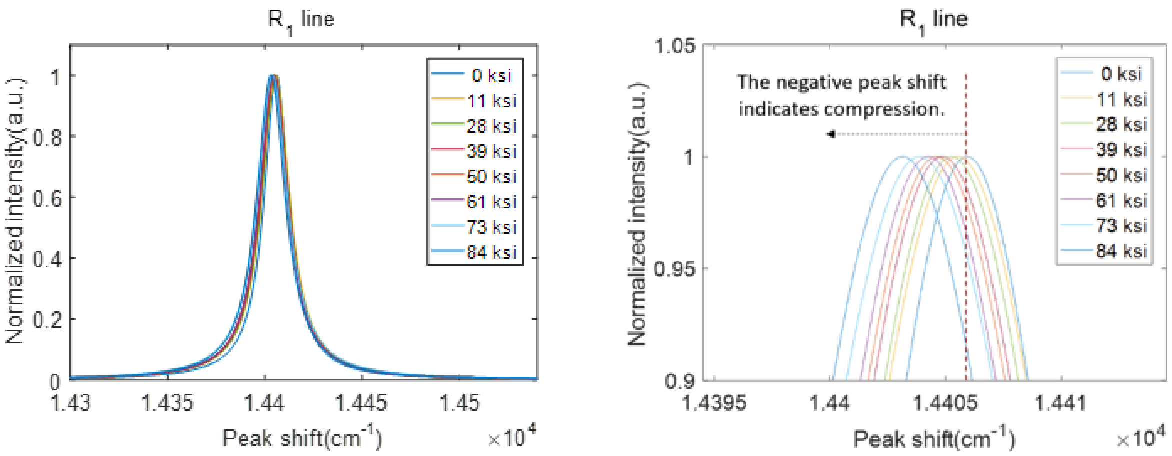

(a) Deconvoluted spectra of R_1 line (b) Zoomed in spectra of R_1 line

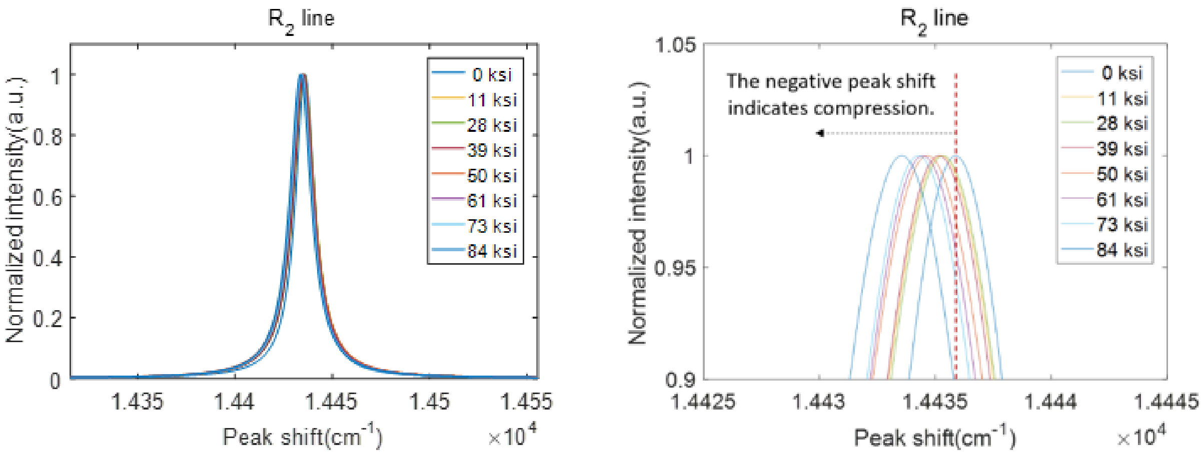

(c) Deconvoluted spectra of R_2 line (d) Zoomed in spectra of R_2 line

Figure 79. Peak shift measurement of α-Al_2O_3 in thermite weld using curve fitting method.

Figure 80 shows the results of the compression test 1. The blue curve shows the stress-deformation curve in Figure 80(a). In the stress-deformation curve, it is found that the sample 1 started to yield around 80 kips. Figure 80(b) shows the stress-peak shift curve. The black and green curves show the peak shift of R_1 and R_2 lines respectively. It is found that there is a downward trend of peak-shifts under 0 kips to 80 kips before the sample yielded. The negative slope indicates that the sample was under compressive stress. However, the peak shifts were not measured well after 80 kips because the laser was out of focus due to the excessive deformation, as the sample yielded.

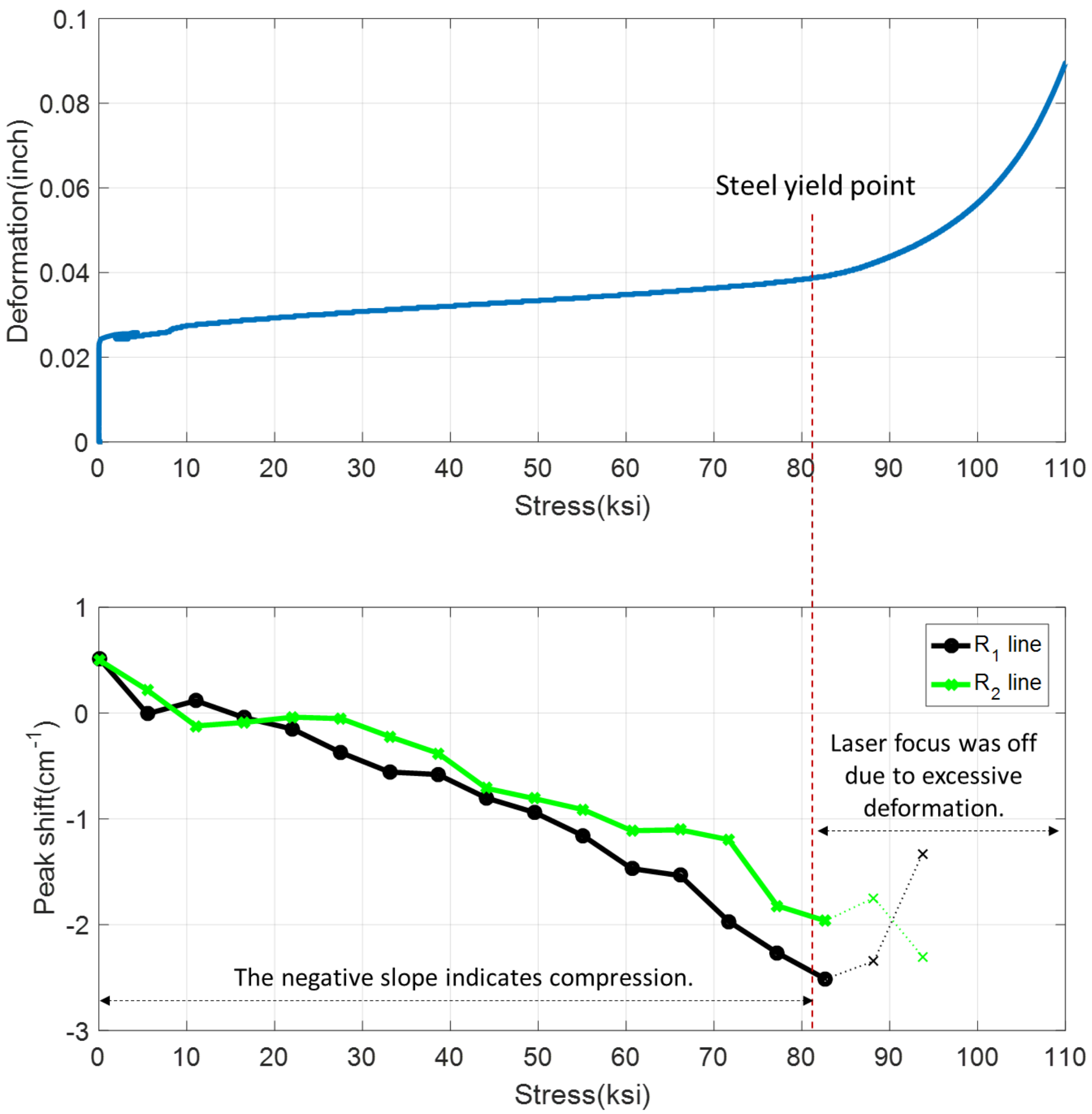

Figure 80. Compression test results (a) stress-deformation curve; (b) stress-peak shift curve of R$_1$ and R$_2$ peaks.

4.5.2 Compression test 2

Table 27 shows the loading conditions and the estimated peak shifts under the different loading conditions. After the sample yielded, the compression test was stopped. The average cross-sectional area of 167mm^2 (0.26 in^2) was used to calculate the stresses. It was expected that the peak shift of 1.8 cm^{-1} was induced under 100 ksi.

Table 27. Applied forces and estimated peak shifts for compression test 1.

#	Force (kips)	Estimated stress (ksi)	Estimated stress (MPa)	Estimated peak shift (cm-1)
1	0	0	0	0
2	1	3.9	26.6	0.07
3	2	7.7	53.3	0.14
4	3	11.6	79.9	0.21
5	4	15.5	106.6	0.28
6	5	19.3	133.2	0.35
7	6	23.2	159.8	0.42
8	7	27.0	186.5	0.49
9	8	30.9	213.1	0.56
10	9	34.8	239.8	0.64
11	10	38.6	266.4	0.71
12	11	42.5	293.1	0.78
13	12	46.4	319.7	0.85
14	13	50.2	346.3	0.92
15	14	54.1	373.0	0.99
16	15	58.0	399.6	1.06
17	16	61.8	426.3	1.13
18	17	65.7	452.9	1.20
19	18	69.6	479.5	1.27
20	19	73.4	506.2	1.34
21	20	77.3	532.8	1.42
22	21	81.1	559.5	1.48
23	22	85.0	586.1	1.55
24	23	88.9	612.7	1.62
25	24	92.7	639.4	1.69
26	25	96.6	666.0	1.77
27	26	100.5	692.7	1.84
28	27	104.3	719.3	1.91
29	28	108.2	746.0	1.98
30	29	112.1	772.6	2.05
31	30	115.9	799.2	2.12
32	31	119.8	825.9	1.19
33	32	123.6	852.5	2.26
34	33	127.5	879.2	2.33
35	34	131.4	905.8	2.40
36	35	135.2	932.4	2.47
37	36	139.1	959.1	2.54
38	37	143.0	985.7	2.61
39	38	146.8	1012.4	2.68

Figure 81 shows the photographs of sample 2 under different loading conditions. As shown in the figure, the upper plate of UTM came down at 100 ksi, as the sample 2 yielded. The obtained raw fluorescence spectra were deconvoluted using Lorentzian curves to see the peak shift precisely. The procedures of spectrum analysis were same with the compression test 1.

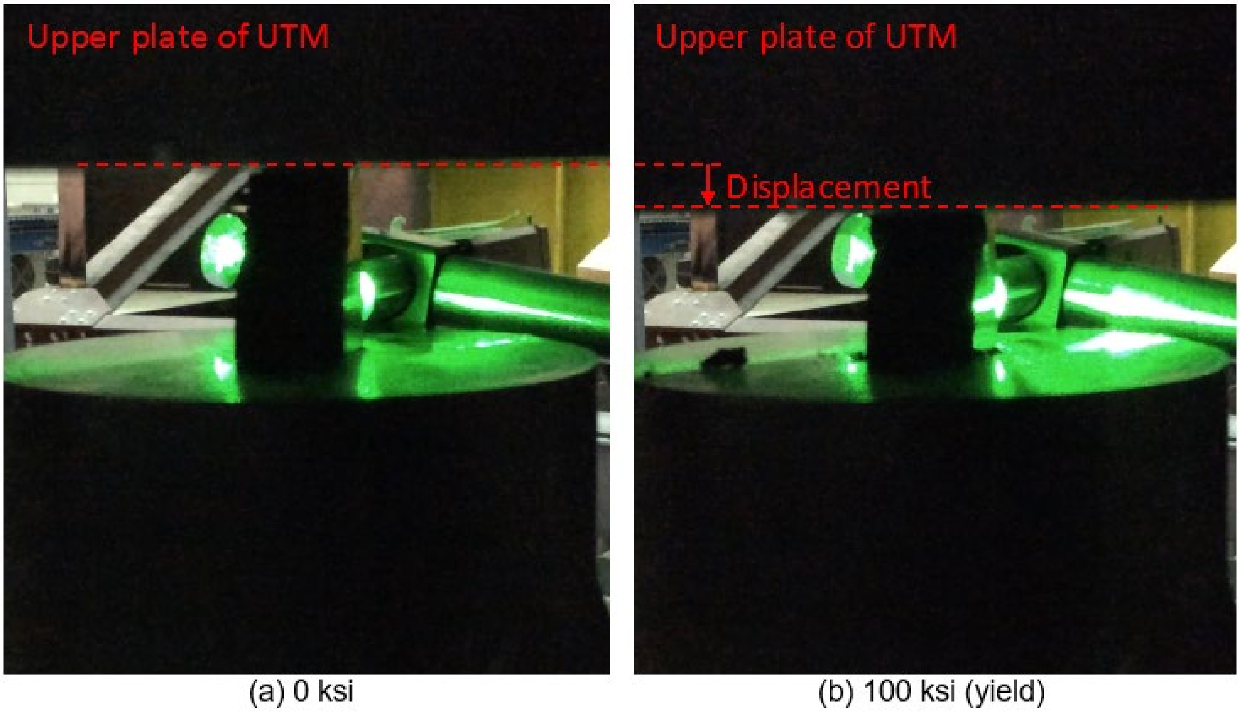

(a) 0 ksi (b) 100 ksi (yield)

Figure 81. Photographs under different loading conditions.

Figure 82 shows the results of the compression test 2. The blue curve which is the stress-deformation curve shows that the sample 2 started to yield around 80 kips as shown in Figure 82(a). The black and green curves show the peak shift of R_1 and R_2 lines respectively. It is found that there is a downward trend of peak-shifts under 0 kips to 80 kips before the sample yielded. The negative slope indicates that the sample was under compressive stress. However, the peak shifts were not measured well after 80 kips because the laser was out of focus due to the excessive deformation as the sample yielded

Although the peak shifts were found, the values were bigger than what we expected. The reason is either the piezo-spectroscopic coefficient is not correct or the local stress was different to global stress in the sample. Therefore, additional compression tests are required to calculate the piezo-spectroscopic coefficient precisely.

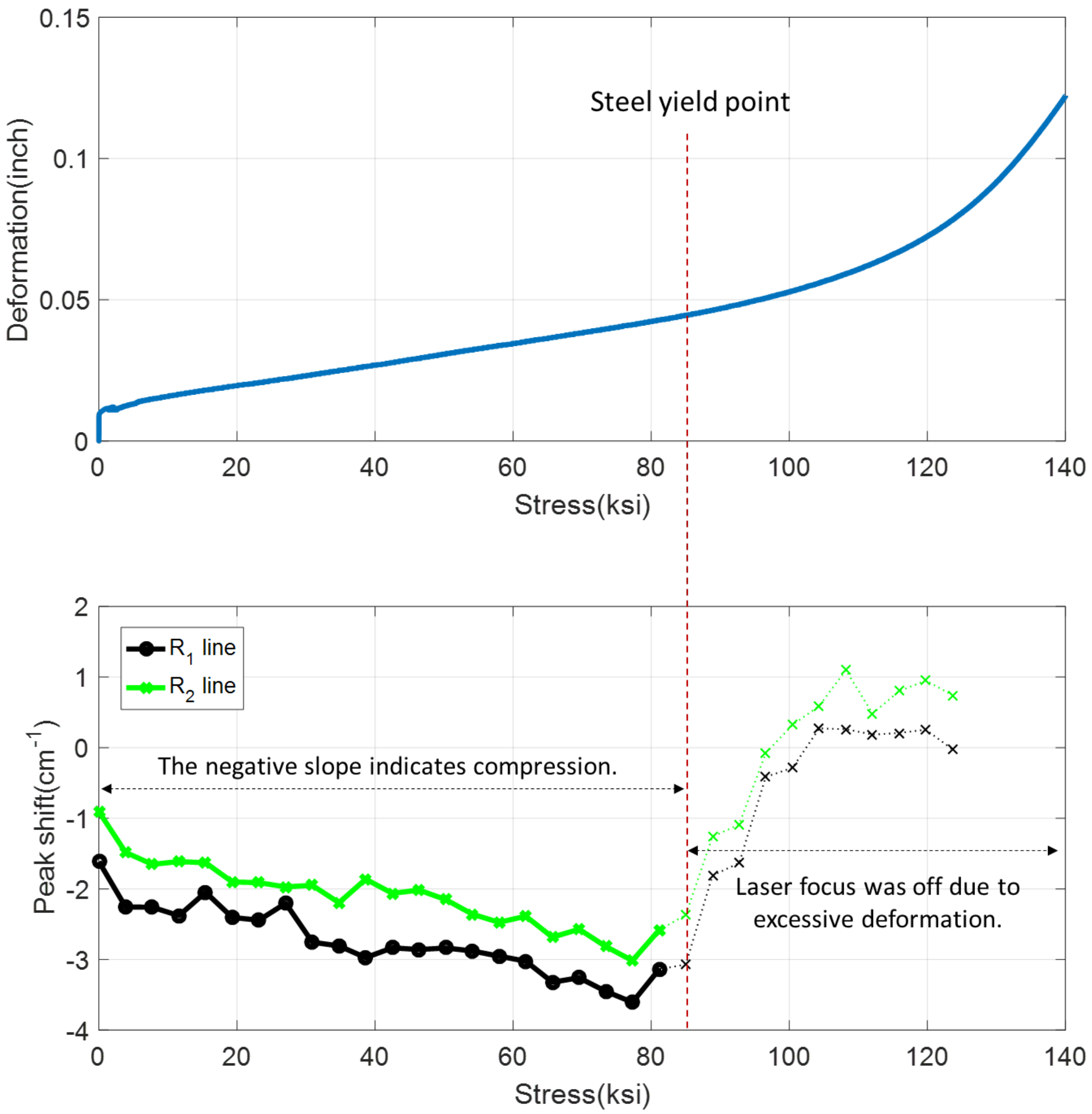

Figure 82. Compression test results (a) time-displacement and load curve; (b) load-peak shift curve of R_1 and R_2 peaks.

4.5.3 Calculation of piezo-spectroscopic coefficients

The absolute peak shifts, y-axis in Figure 83, were calculated using the stress-free fluorescence spectrum of α-Al_2O_3 in thermite weld to calculate the piezo-spectroscopic coefficients (PSC) of R_1 and R_2 lines. The PSCs of R1 and R2 lines were calculated respectively based on the results of the two compression tests measured under yield point by applying a linear regression model as shown in Figure 83. Black and red lines indicate the stress-peak shift curves of compression test 1 and 2 respectively. The blue lines show the fitted lines for each stress-peak shift curve. The linear relationship is described in figures and confirmed by the high R-squared values of about 90 percent.

The calculated PSCs of R_1 lines are 4.66 and 2.81 cm^{-1}/GPa for test 1 and 2 respectively, and the PSCs of R_2 lines are 3.61 and 2.81 cm^{-1}/GPa for test 1 and 2 respectively. The reason why the

PSCs are different from each other is that the stresses were not exactly controlled in the compression tests, since the sample shapes were irregular, and the top and bottom surfaces of samples were not exactly parallel. Due to the reasons mentioned above, the induced stresses at the tiny spot where laser focused were different from the stresses in the other regions. Therefore, additional compressive and tensile tests are required to calculated accurate PSC values of R_1 and R_2 lines for α-Al_2O_3 in thermite weld under perfectly controlled stress condition.

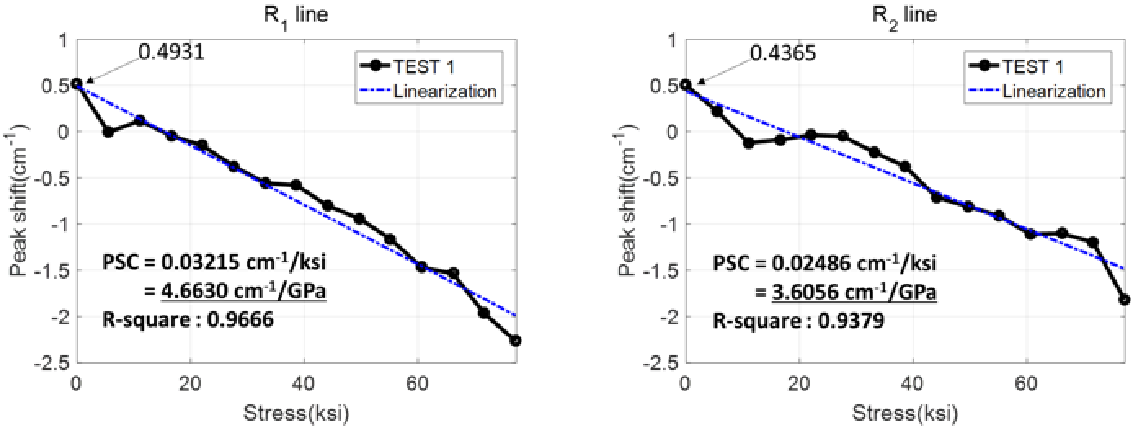

(a) R_1 line of compression test 1

(b) R_2 line of compression test 1

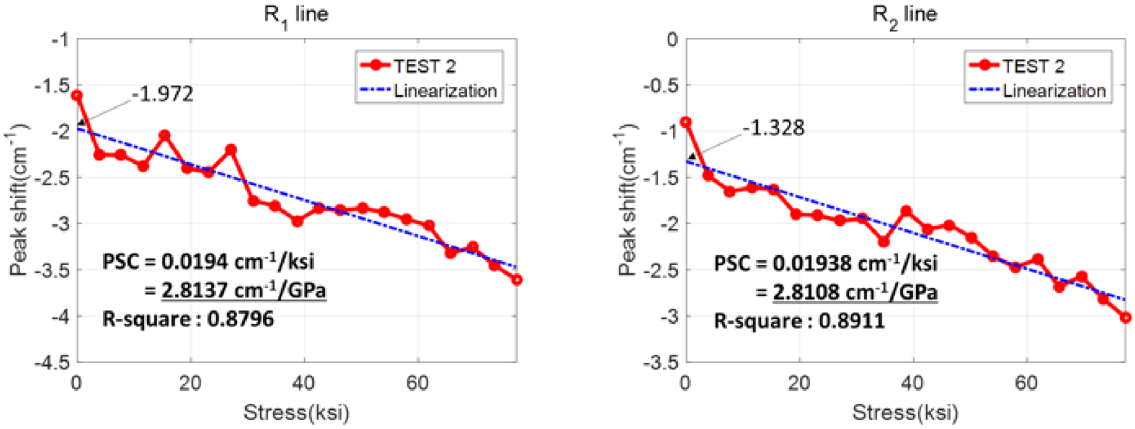

(c) R_1 line of compression test 2

(d) R_2 line of compression test 2

Figure 83. Fluorescence piezo-spectroscopic coefficients of R_1 and R_2 lines.

4.6 Key findings

Distribution of α-Al_2O_3 in thermite weld zone

The distribution of α-Al_2O_3 in thermite weld zone was investigated by drawing 2 and 3 dimensional maps of a thermite weld zone. There is significant concentrations of α-Al_2O_3 inside and outside the thermite weld zone using fluorescence spectroscopy which is non-contact and non-destructive technique.

Absolute stress measurement

To measure the absolute stress in rail, the stress-free state was determined by measuring the fluorescence spectrum of the α-Al_2O_3 powder in thermite weld zone. Using the stress-free fluorescence spectrum of α-Al_2O_3 powder in thermite weld zone, the absolute stress in rail can be measured.

Piezo-spectroscopic coefficient

To understand the relationship between stress and peak shift of R_1 and R_2 lines of the α-Al_2O_3, compression tests were performed to two blocks of thermite weld zone, and the piezo-spectroscopic coefficients were calculated using a linear regression model. The calculated piezo-spectroscopic coefficients were 2.8-4.6 cm-1/GPa and indicate that the R_1(or R_2) line will be shifted for 2.8-4.6 cm^{-1} under the stress of 1 GPa. Although the piezo-spectroscopic coefficients are not accurate, it is found that the R_1 and R_2 lines are shifted under different stress level, and it has linear relationship between stress and peak shift. The piezo-spectroscopic coefficients were calculated using a linear regression model: 3.7388 cm-1/GPa (0.025775 cm-1/ksi) for R1 and 3.2082 cm-1/GPa (0.02212 cm-1/ksi).

Table 28. Fluorescence piezo-spectroscopic coefficients for α-Al_2O_3 in thermite weld

	R_1	R_2
Averaged piezo-spectroscopic coefficients	3.7388 cm^{-1}/GPa (0.025775 cm^{-1}/ksi)	3.2082 cm^{-1}/GPa (0.02212 cm^{-1}/ksi)

5. Conclusion

The objectives of this project were to identify Raman/Fluorescence-sensitive oxides in the rail, which can be used as an in-situ sensor for absolute stress measurement. The conclusions of this research are as follows:

Iron oxide and hydroxide layers on the surface of rail: It was observed that the existence of the iron oxides and hydroxides on rail surface in a series of material characterization tests, including scanning electron microscopy (SEM), Raman spectroscopy, X-ray diffraction (XRD) and energy-dispersive X-ray spectroscopy (EDS) and nano-indentation for three rail samples manufactured in 1948, 1999, and 2012. Different iron oxides and hydroxides were observed in different colors on rail surface. Important findings of the iron oxides and hydroxides, which were made in material characterization tests, include the followings:

Gray-colored layer

- The surface of the gray-colored layer is a mixture of hematite and magnetite.
- The hematite is known to have Raman piezo-spectroscopic characteristics, which was also confirmed in our Raman piezo-spectroscopy tests.
- The layer developed in a furnace has a uniform thickness of 49 μm.
- However, the layer scales off over time. This layer does not exist in older rails.
- The elastic modulus of gray-colored layer is 107 GPa (15519 ksi).
- The nano-hardness of gray-colored layer is 7.1 GPa (1030 ksi), t similar to the parent material.

Brown-colored layer

- The surface of the brown-colored layer is a mixture of goethite and lepidocrocite.
- This layer grew in an uncontrolled environment, and has an irregular thickness of 43 μm.
- The brown-colored layer sometimes grows on the iron oxide(s) layer.
- The top layer of oxide changes over time to a non-detectable material for Raman spectroscopy and XRD.
- The elastic modulus of brown-colored layer is 46 GPa (6671 ksi).

Raman piezo-spectroscopy tests were conducted to measure residual stress in the iron oxides and hydroxides layers. The following conclusions are made in reference to using iron oxides and hydroxides on rail surface:

- Hematite formed on rail surface during air quenching after milling can be used to measure residual thermal stress. However, the hematite layer is gradually scaled off over time and is not present on older rails. We do not recommend using Hematite as a passive stress sensor.
- The detectability of goethite and lepidocrocite on rail surface decreased for older rail. Also, the goethite and lepidocrocite layers are not mechanically stable due to scaling off

(i.e., rusting). In addition, their growth is largely dependent on environmental conditions. Thus, it is not feasible to use goethite and lepidocrocite as a passive sensor.

Aluminum oxide in thermite weld: A series of fluorescence spectroscopy tests were conducted to detect aluminum oxides in thermite welds. 2D and 3D mapping tests were conducted to understand the distribution of aluminum oxide in the weld. A compression test using a hydraulic loading frame to verify that the aluminum oxide's fingerprint peaks shift as compression load increases. The key observations from these tests are as follows:

- From 2D and 3D mapping tests, it was found that the aluminum oxides are concentrated in the heat-affected zone (HAZ) at the interface of the weld and the parent rail on the surface, while the aluminum oxides are distributed uniformly inside the rail.
- The zero-stress state was determined by measuring the fluorescence fingerprint peaks of the aluminum oxide in a stress-free, fine powder form. The fingerprint peaks of the aluminum oxide were measured at 14405.4036 cm-1 for R1 and 14435.3748 cm-1 for R2.
- Once determining the zero-stress state, we conducted the compression test using a hydraulic loading frame. It was observed that the R1 and R2 peaks shifted to the left as the compressive force increased. The piezo-spectroscopic coefficients were calculated using a linear regression model: 3.7388 cm-1/GPa (0.025775 cm-1/ksi) for R1 and 3.2082 cm-1/GPa (0.02212 cm-1/ksi).

From the above findings, the followings can be concluded in terms of the feasibility of using aluminum oxide in thermite weld:

- The aluminum oxide that is abundantly contained in weld as a byproduct of thermite welding, can be used to measure absolute stress in rail in a non-contact manner.
- Our test results show that the aluminum oxide has an excellent signal-to-noise ratio to measure rail stress without additional surface treatment.
- Since it is well established that high concentrations of aluminum oxides in steel makes the thermite weld brittle, Raman and fluorescence spectrometry could be used as a non-contact quality assurance method to inspect chemical (Al_2O_3 and iron oxides) and mechanical (residual stress) conditions of thermite welds in field.
- The spectrometer used in this study has the maximum resolution of 3~4 cm-1, and a commonly used curve fitting method was adopted as a post-processing technique to increase the resolution of stress measurement. Without post-processing technique, it is recommended to have 0.01 cm-1 resolution that is equivalent to 4 MPa (0.58 ksi) in stress and 1.6 °C (2.88 °F) in temperature.

6. References

[1] Y. Sone, J. Suzumura, T. Ban, F. Aoki, and M. Ishida, “Possibility of in situ spectroscopic analysis for iron rust on the running band of rail,” *Wear*, vol. 265, no. 9–10, pp. 1396–1401, Oct. 2008.

[2] S.-H. Shim and T. S. Duffy, “Raman spectroscopy of Fe2O3 to 62 GPa,” *Am. Mineral.*, vol. 87, pp. 318–326, 2001.

[3] H. E. McGannon, *The Making, Shaping and Treating of Steel*. 1985.

[4] D. Chicot, J. Mendoza, a. Zaoui, G. Louis, V. Lepingle, F. Roudet, and J. Lesage, “Mechanical properties of magnetite (Fe3O4), hematite (α-Fe2O3) and goethite (α-FeO·OH) by instrumented indentation and molecular dynamics analysis,” *Mater. Chem. Phys.*, vol. 129, no. 3, pp. 862–870, Oct. 2011.

[5] A. Ouglova, Y. Berthaud, and F. Foct, “Mechanical properties of an iron oxide formed by corrosion in reinforced concrete structures,” vol. 48, pp. 3988–4000, 2006.

[6] K. G. Dassios and C. Galiotis, “Fluorescence studies of polycrystalline Al2O3 composite constituents: piezo-spectroscopic calibration and applications,” *Appl. Phys. A Mater. Sci. Process.*, vol. 79, no. 3, pp. 647–659, Aug. 2004.

[7] D. M. Lipkin and D. R. Clarke, “Measurement of the stress in oxide scales formed by oxidation of alumina-forming alloys,” *Oxid. Met.*, vol. 45, no. 3–4, pp. 267–280, Apr. 1996.

Appendix A.
Scanning Electron Microscopy Images (SEM)

A.1 Gray-colored layer in 2012 rail

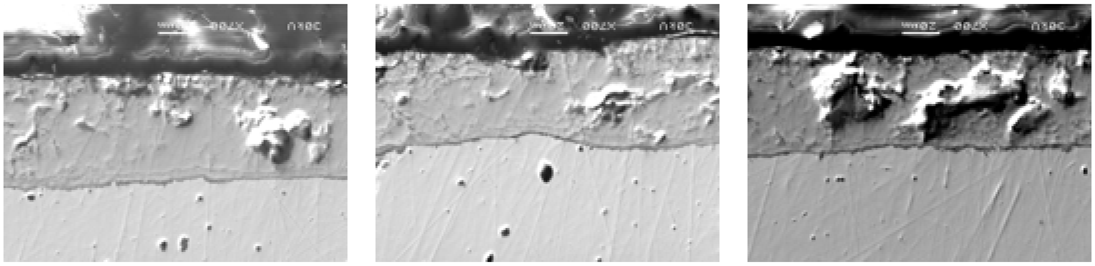

(a) Location 1 (x700, 30kV) (b) Location 2 (x700, 30kV) (c) Location 3 (x700, 30kV)

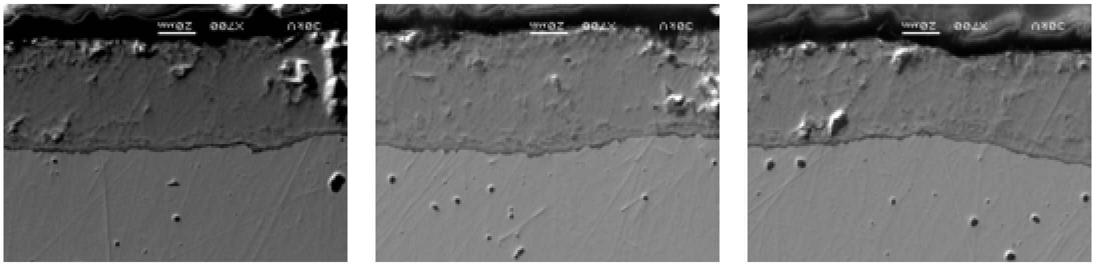

(d) Location 4 (x700, 30kV) (e) Location 5 (x700, 30kV) (f) Location 6 (x700, 30kV)

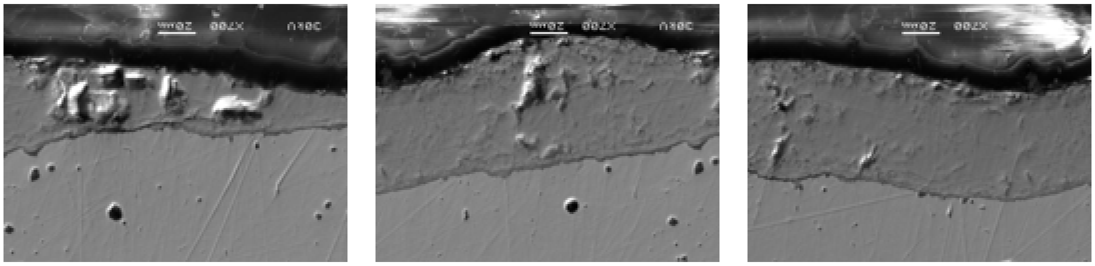

(g) Location 7 (x700, 30kV) (h) Location 8 (x700, 30kV) (i) Location 9 (x700, 30kV)

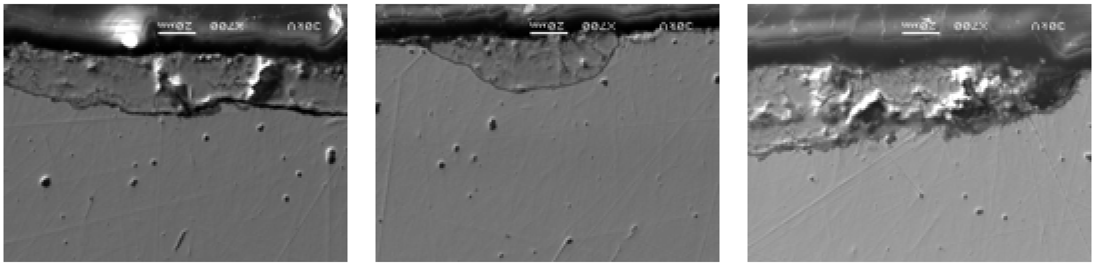

(j) Location 13 (x700, 30kV) (k) Location 14 (x700, 30kV) (l) Location 15 (x700, 30kV)

Figure 84. SEM cross section images for gray-colored layer on 2012 rail (1).

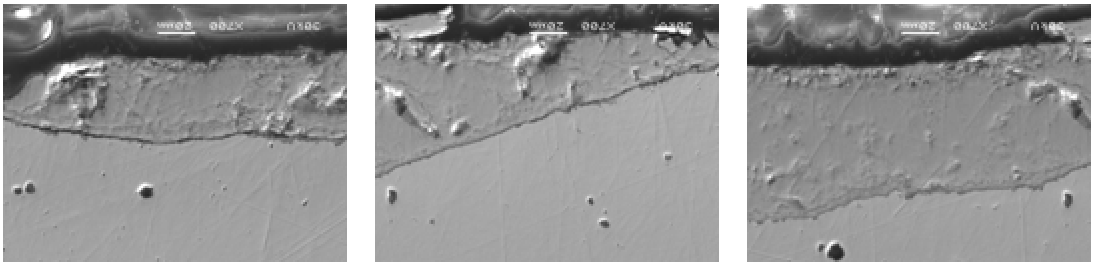

(a) Location 16 (x700, 30kV) (b) Location 17 (x700, 30kV) (c) Location 18 (x700, 30kV)

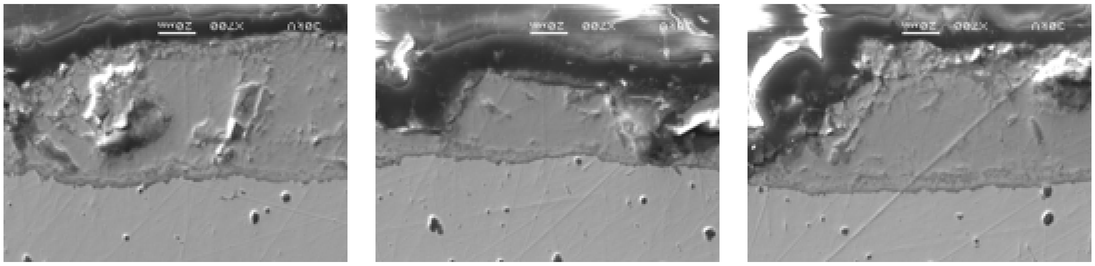

(d) Location 19 (x700, 30kV) (e) Location 20 (x700, 30kV) (f) Location 21 (x700, 30kV)

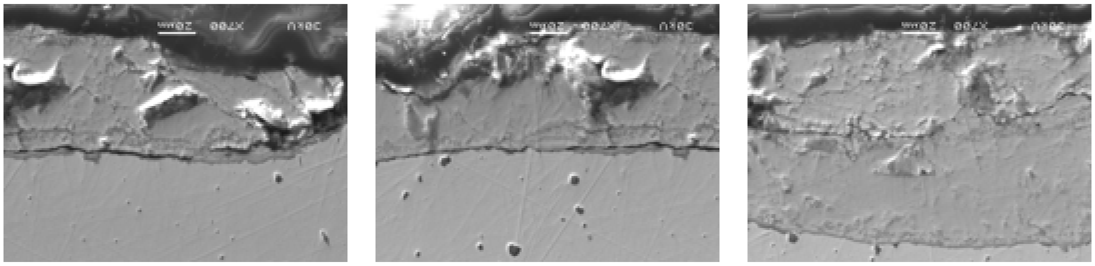

(g) Location 22 (x700, 30kV) (h) Location 23 (x700, 30kV) (i) Location 30 (x700, 30kV)

Figure 85. SEM cross section images for gray-colored layer on 2012 rail (2).

A.2 Brown-colored layer in 2012 rail

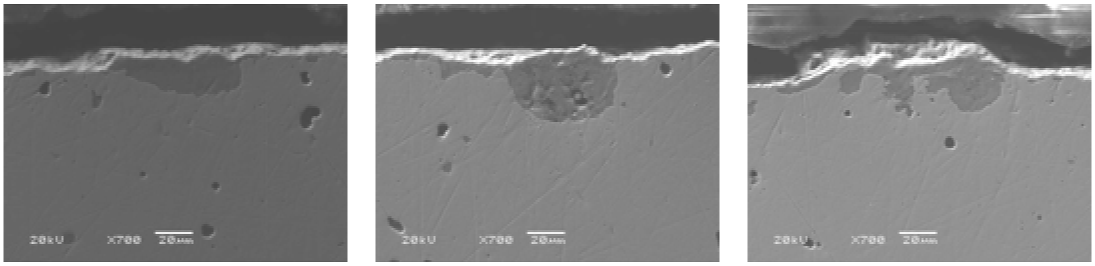

(a) Location 1 (x700, 20kV) (b) Location 2 (x700, 20kV) (c) Location 3 (x700, 20kV)

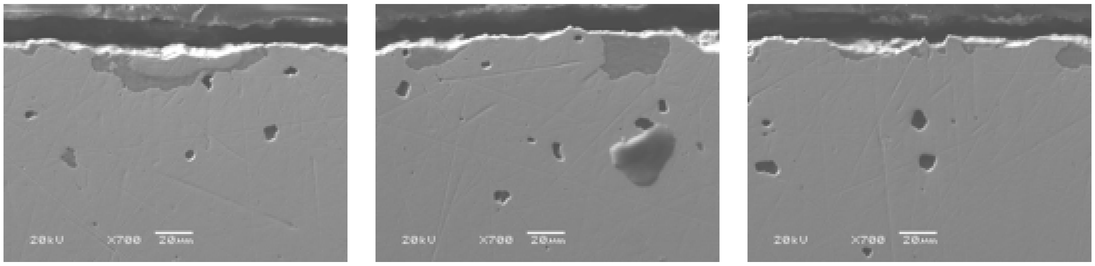

(d) Location 4 (x700, 20kV) (e) Location 5 (x700, 20kV) (f) Location 6 (x700, 20kV)

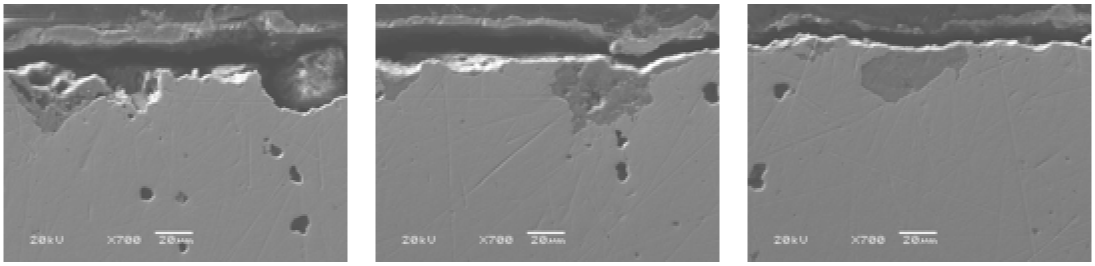

(g) Location 7 (x700, 20kV) (h) Location 8 (x700, 20kV) (i) Location 9 (x700, 20kV)

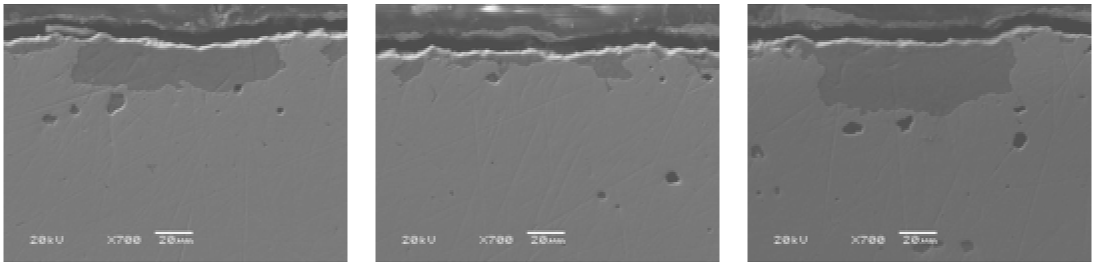

(a) Location 13 (x700, 20kV) (b) Location 14 (x700, 20kV) (c) Location 15 (x700, 20kV)

Figure 86. SEM cross section images for the brown-colored layer on 2012 rail (1).

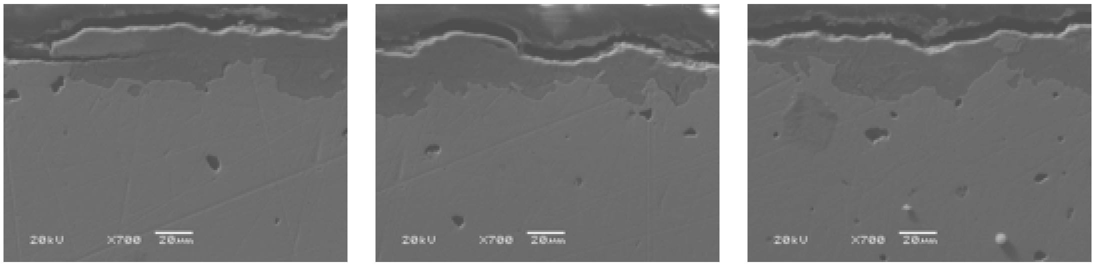

(a) Location 16 (x700, 20kV) (b) Location 17 (x700, 20kV) (c) Location 18 (x700, 20kV)

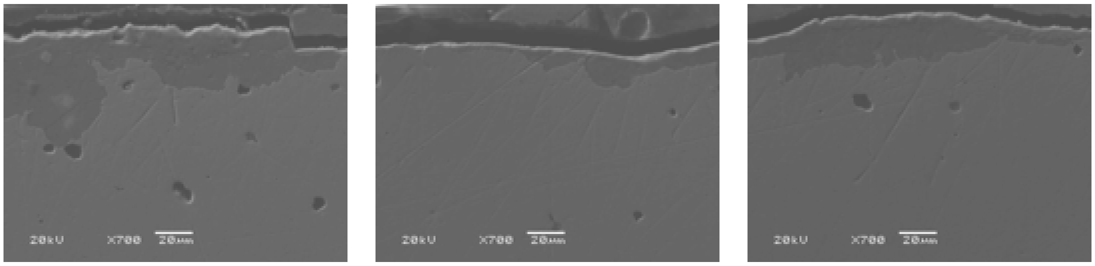

(d) Location 19 (x700, 20kV) (e) Location 20 (x700, 20kV) (f) Location 21 (x700, 20kV)

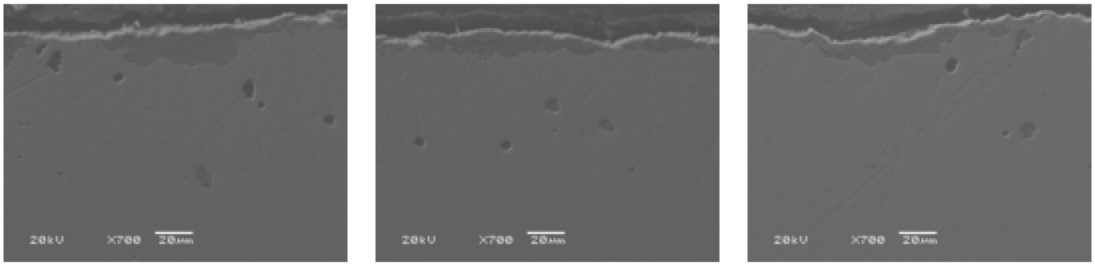

(g) Location 22 (x700, 20kV) (h) Location 23 (x700, 20kV) (i) Location 24 (x700, 20kV)

Figure 87. SEM cross section images for the brown-colored layer on 2012 rail (2).

A.3 Brown-colored layer in 1999 rail

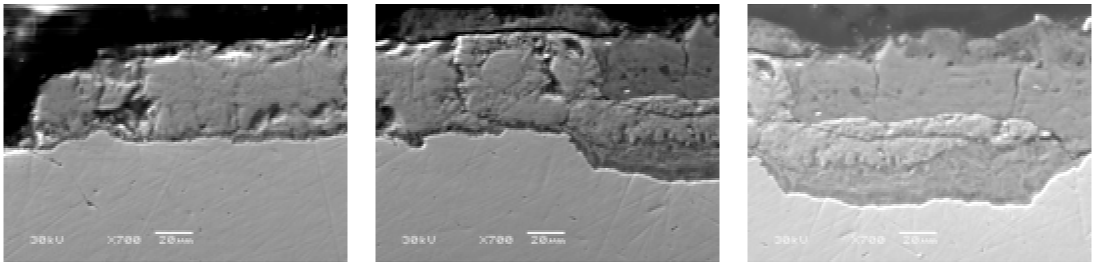

(a) Location 1 (x700, 30kV) (b) Location 2 (x700, 30kV) (c) Location 3 (x700, 30kV)

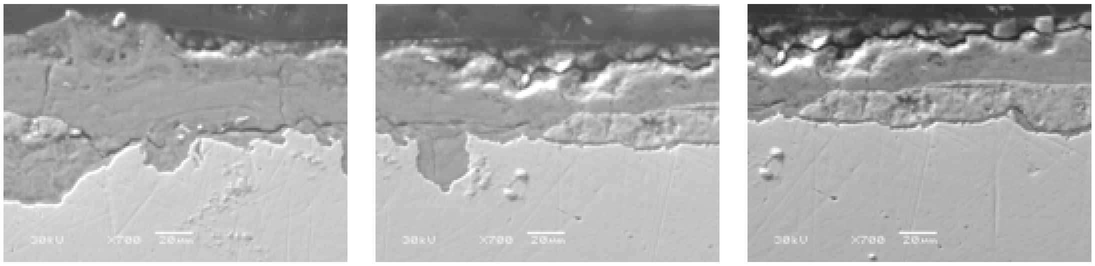

(d) Location 4 (x700, 30kV) (e) Location 5 (x700, 30kV) (f) Location 6 (x700, 30kV)

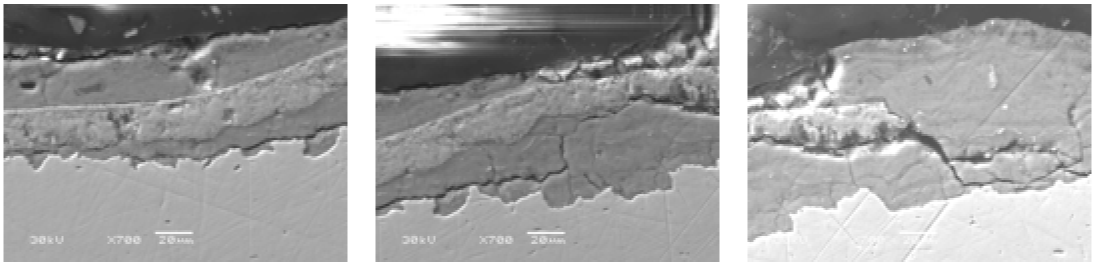

(g) Location 7 (x700, 30kV) (h) Location 8 (x700, 30kV) (i) Location 9 (x700, 30kV)

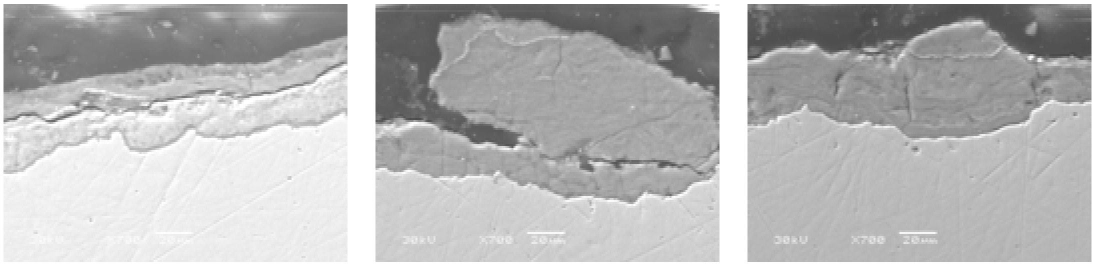

(a) Location 13 (x700, 30kV) (b) Location 14 (x700, 30kV) (c) Location 15 (x700, 30kV)

Figure 88. SEM cross section images for brown-colored layer on 1999 rail (1).

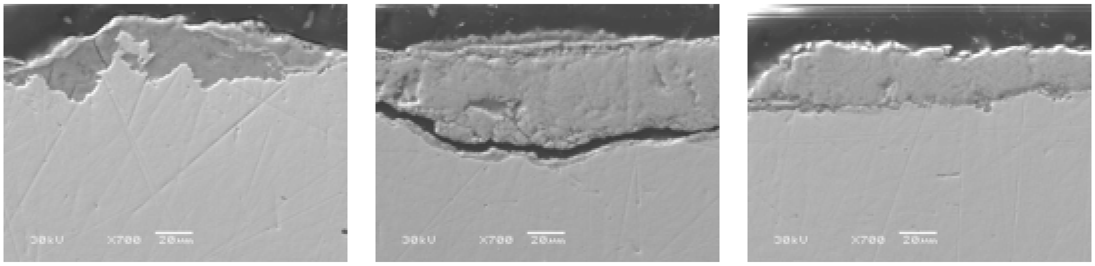

(a) Location 16 (x700, 30kV) (b) Location 17 (x700, 30kV) (c) Location 18 (x700, 30kV)

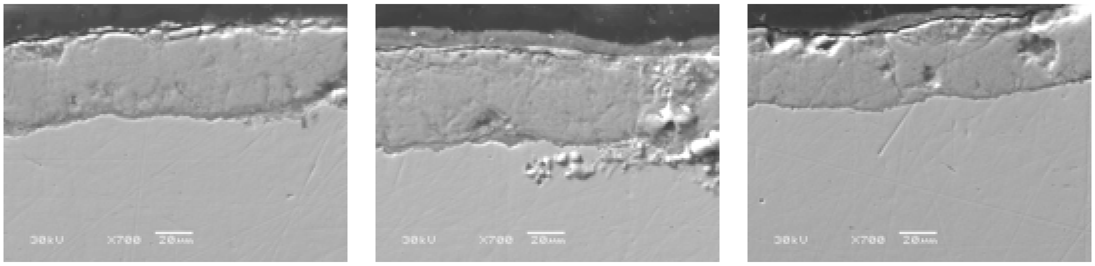

(d) Location 19 (x700, 30kV) (e) Location 20 (x700, 30kV) (f) Location 21 (x700, 30kV)

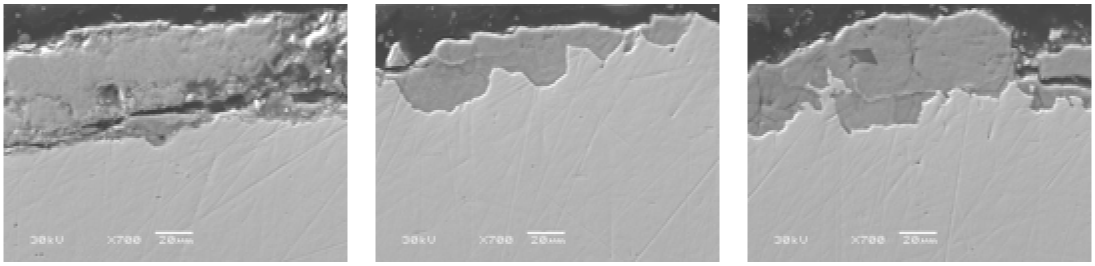

(g) Location 22 (x700, 30kV) (h) Location 23 (x700, 30kV) (i) Location 24 (x700, 30kV)

Figure 89. SEM cross section images for brown-colored layer on 1999 rail (2).

A.4 Brown-colored layer in 1948 rail

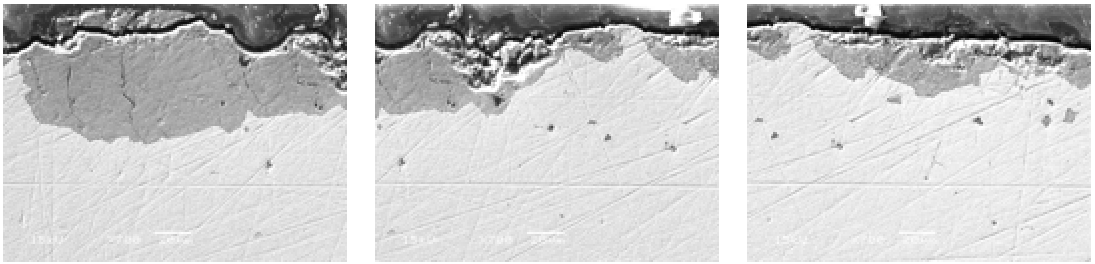

(a) Location 1 (x700, 30kV) (b) Location 2 (x700, 30kV) (c) Location 3 (x700, 30kV)

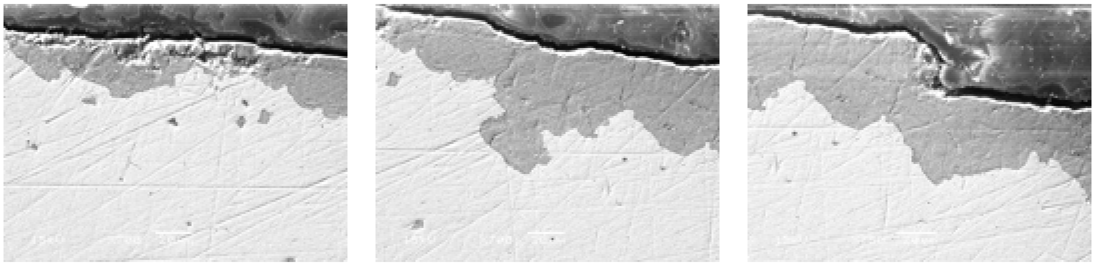

(d) Location 4 (x700, 30kV) (e) Location 5 (x700, 30kV) (f) Location 6 (x700, 30kV)

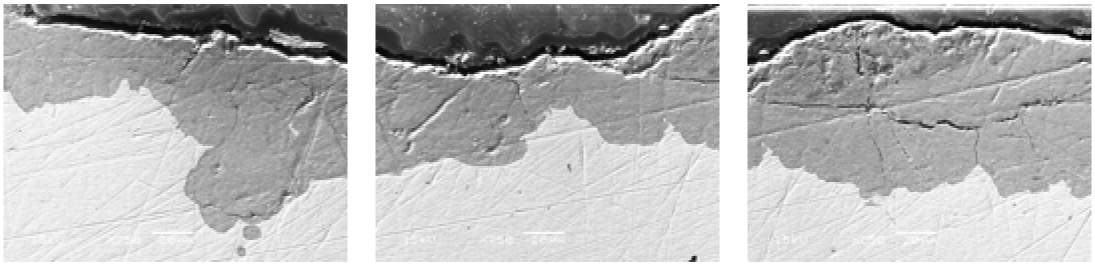

(g) Location 7 (x700, 30kV) (h) Location 8 (x700, 30kV) (i) Location 9 (x700, 30kV)

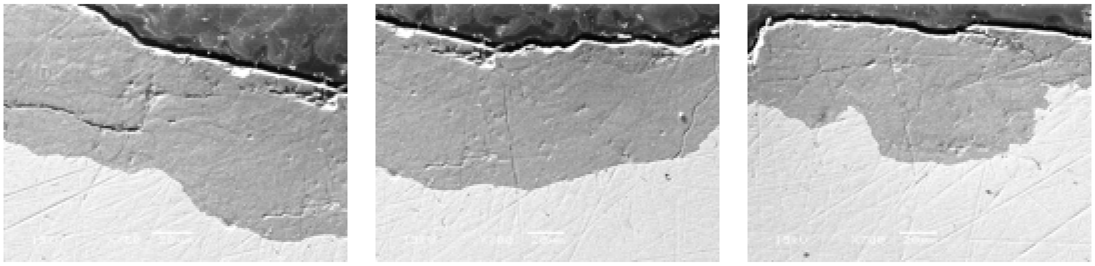

(a) Location 13 (x700, 30kV) (b) Location 14 (x700, 30kV) (c) Location 15 (x700, 30kV)

Figure 90. SEM cross section images for brown-colored layer on 1948 rail (1).

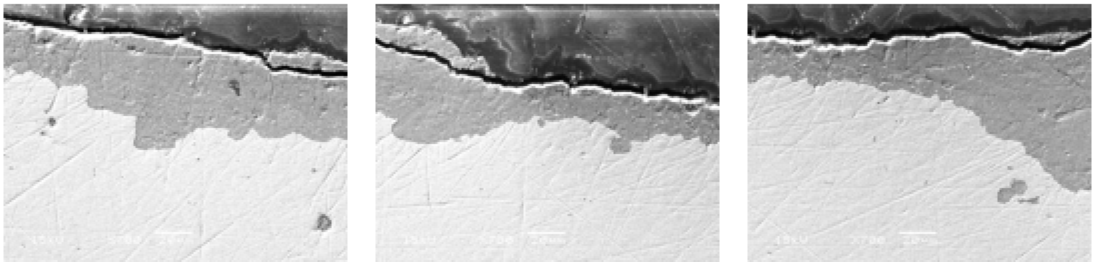

(a) Location 16 (x700, 30kV) (b) Location 17 (x700, 30kV) (c) Location 18 (x700, 30kV)

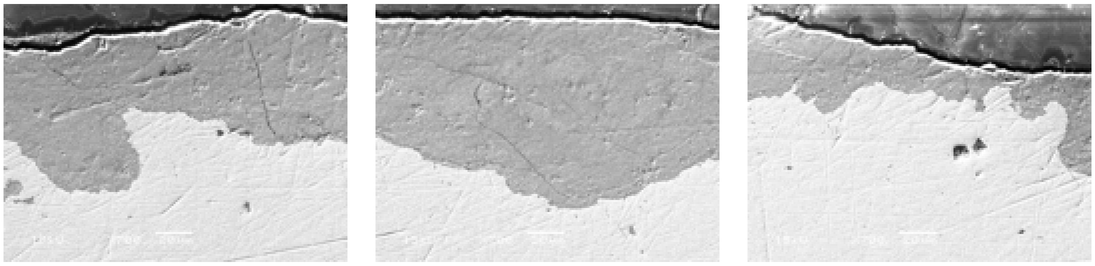

(d) Location 19 (x700, 30kV) (e) Location 20 (x700, 30kV) (f) Location 21 (x700, 30kV)

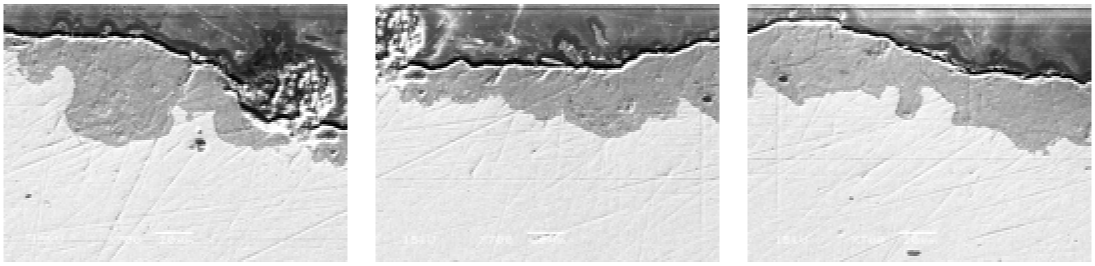

(g) Location 22 (x700, 30kV) (h) Location 23 (x700, 30kV) (i) Location 24 (x700, 30kV)

Figure 91. SEM cross section images for brown-colored layer on 1948 rail (2).

Appendix B.
Raman Spectroscopy

514nm laser – 2012 rail (gray-colored layer)

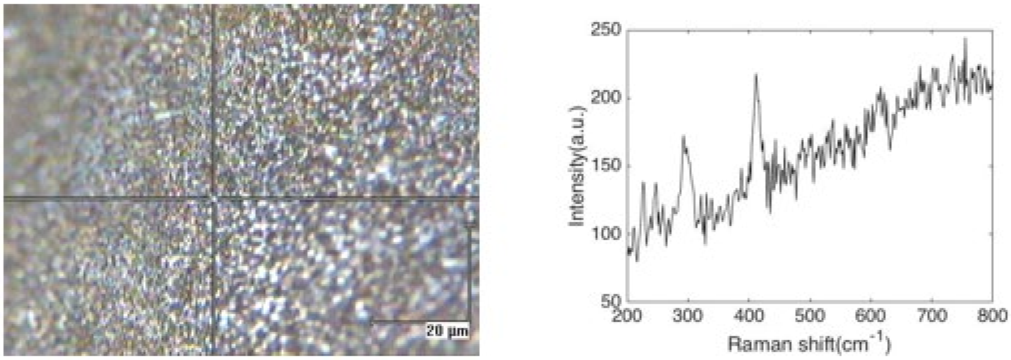

(a) Microscope image of location 1

(b) Raman spectrum of location 1

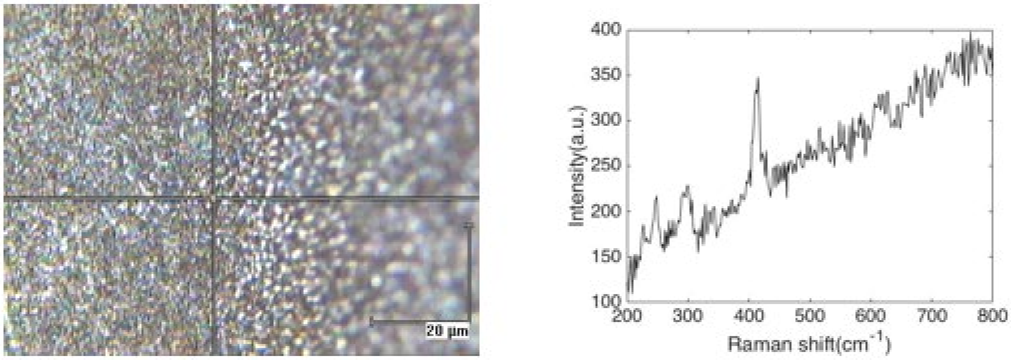

(c) Microscope image of location 2

(d) Raman spectrum of location 2

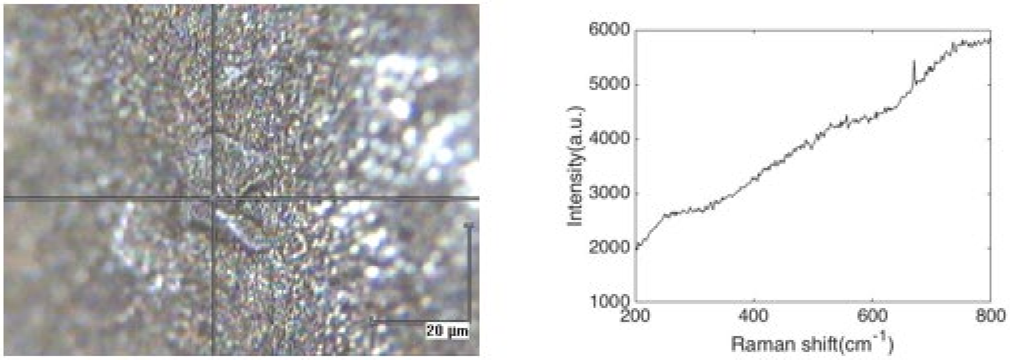

(e) Microscope image of location 3

(f) Raman spectrum of location 3

Figure 92. Microscope surface images and Raman spectra of gray-colored layer on 2012 rail using 514nm laser (1). [120sec, no averaging, x50 objective]

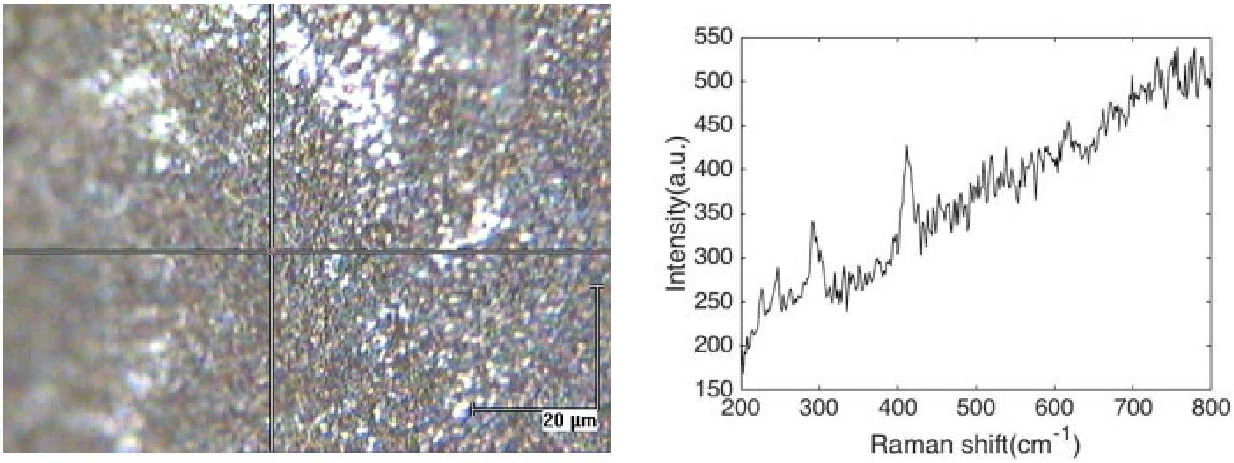

(a) Microscope image of location 4 (b) Raman spectrum of location 4

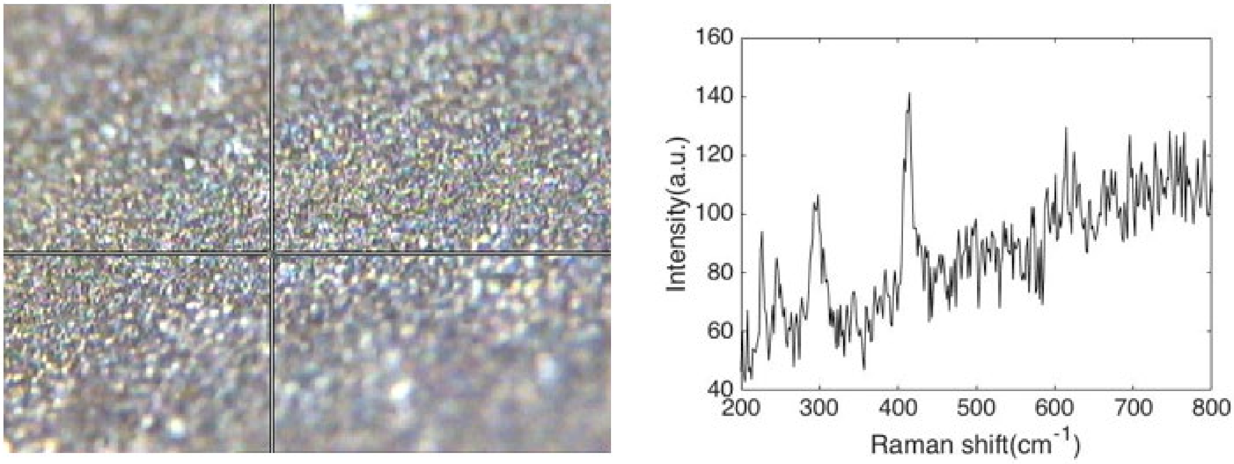

(c) Microscope image of location 5 (d) Raman spectrum of location 5

Figure 93. Microscope surface images and Raman spectra of gray-colored layer on 2012 rail using 514nm laser (2). [120sec, no averaging, x50 objective]

Table 29. Peak locations of Raman spectra collected from gray-colored layer on 2012 rail using 514nm laser

Samples	Peak wavenumbers					
Location 1	226.9	247.2	292.2	297.9	411.4	416.4
Location 2	226.9	248.9	292.9	299.6	411.4	414.8
Location 3	No peaks					
Location 4	226.9	247.2	291.2		411.4	
Location 5	226.9	245.5	292.9	297.9	408.0	414.8

785nm laser – 2012 rail (gray-colored layer)

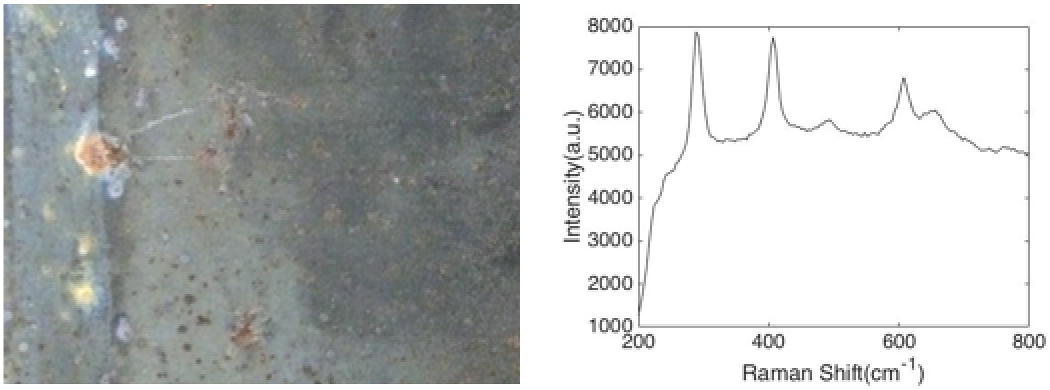

(a) Surface photograph

(b) Location 1 (10sec, 1times)

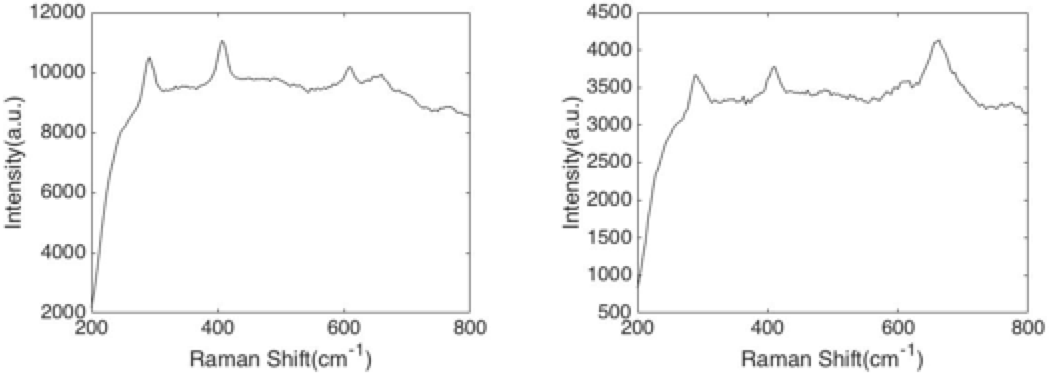

(c) Location 2 (10sec, 1times)

(d) Location 3 (10sec, 1times)

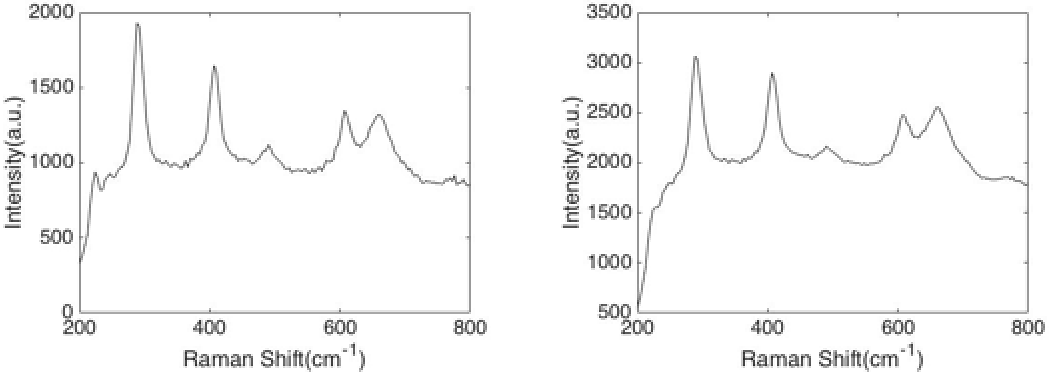

(e) Location 4 (10sec, 6times)

(f) Location 5 (10sec, 6times)

Figure 94. Surface photograph and Raman spectra of gray-colored layer on 2012 rail using 785nm laser.

Table 30. Peak locations of Raman spectra collected from gray-colored layer on 2012 rail using 785nm laser

Samples	Peak wavenumbers					
Location 1		288.2	406.8	493.8	607.4	659.7
Location 2		291.9	406.8		610.9	659.7
Location 3		288.2	410.4		617.9	663.1
Location 4	224	288.2	406.8	490.2	607.4	659.7
Location 5		288.2	406.8	490.2	607.4	659.7

514nm laser – 2012 rail (brown-colored layer)

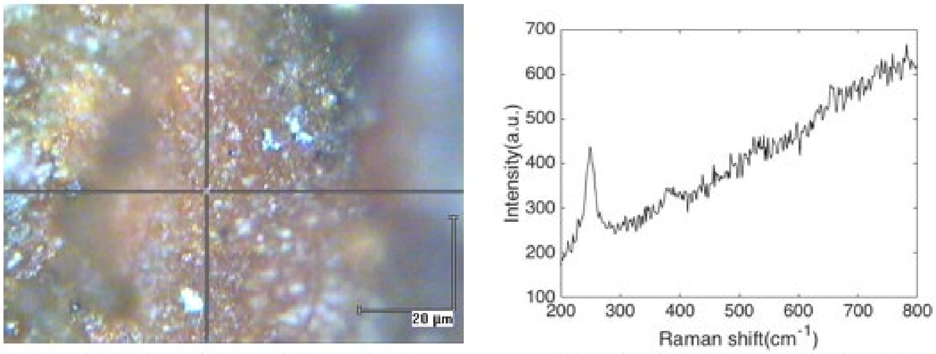

(a) Microscope image of location 1 (b) Raman spectrum of location 1

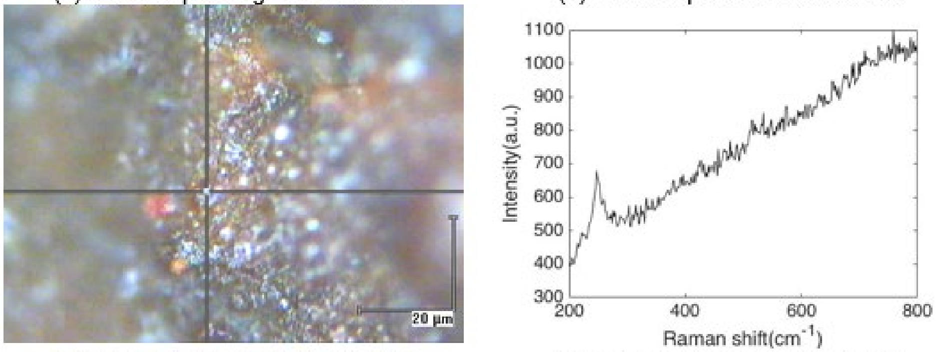

(c) Microscope image of location 2 (d) Raman spectrum of location 2

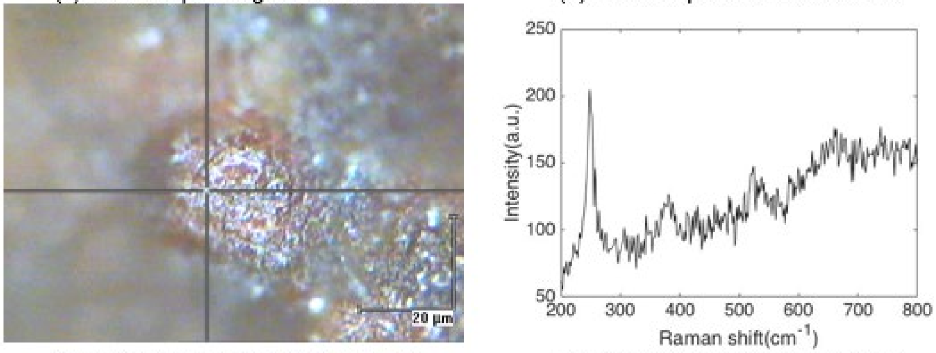

(e) Microscope image of location 3 (f) Raman spectrum of location 3

Figure 95. Microscope surface images and Raman spectra of brown-colored layer on 2012 rail using 514nm laser (1). [60sec, 2 averaging, x50 objective]

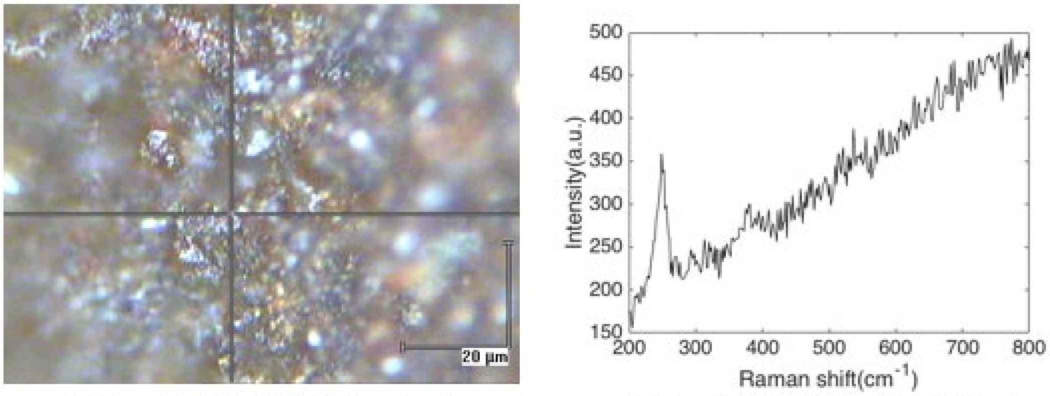

(a) Microscope image of location 4 (b) Raman spectrum of location 4

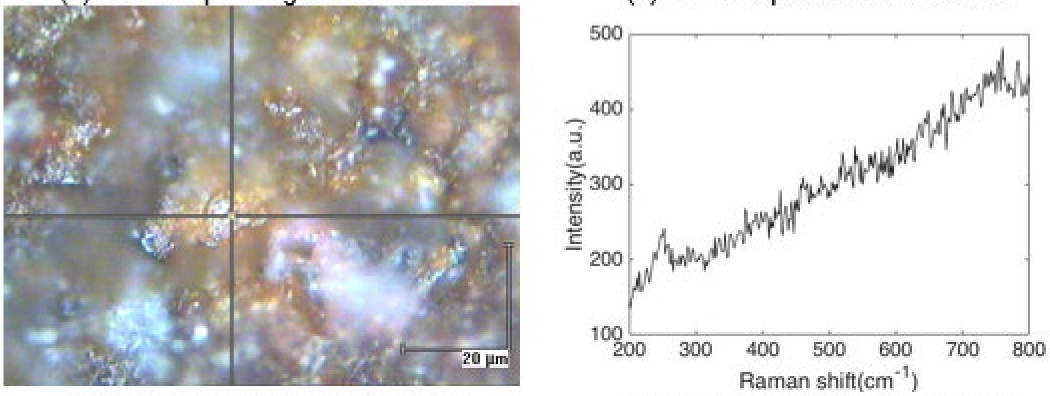

(c) Microscope image of location 5 (d) Raman spectrum of location 5

Figure 96. Microscope surface images and Raman spectra of brown-colored layer on 2012 rail using 514nm laser (2). [60sec, 2 averaging, x50 objective]

Table 31. Peak locations of Raman spectra collected from brown-colored layer on 2012 rail using 514nm laser

Samples	Peak wavenumbers					
Location 1	248.9		377.5			
Location 2	247.2			514.6		
Location 3	248.9	257.3	380.9		524.8	660.0
Location 4	248.9		380.9		536.6	660.0
Location 5	252.2					

785nm laser – 2012 rail (brown-colored layer)

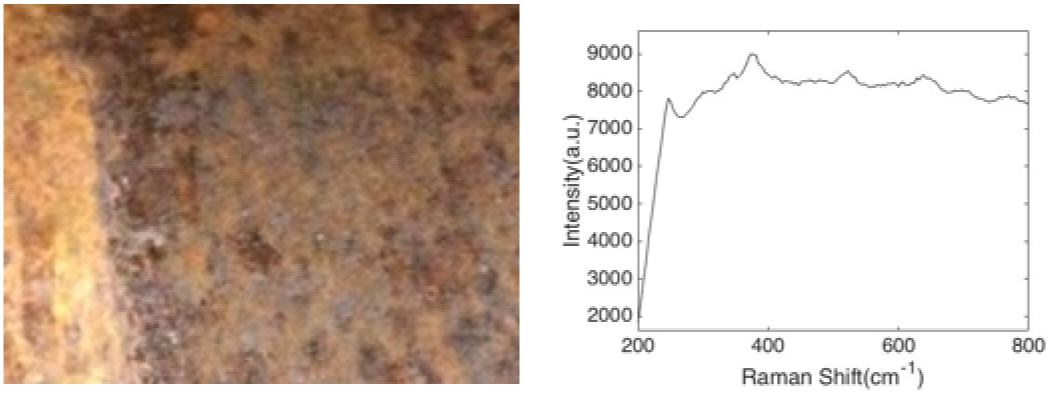

(a) Surface photograph

(b) Location 1 (10sec, 1times)

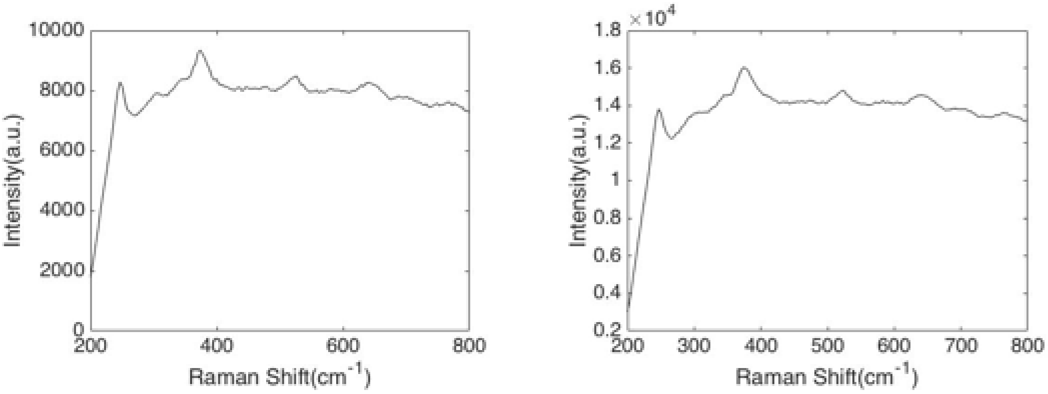

(c) Location 2 (10sec, 1times)

(d) Location 3 (10sec, 1times)

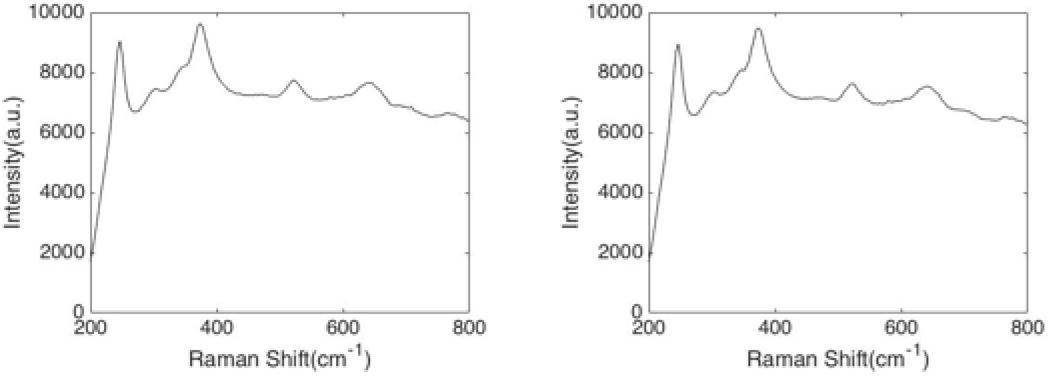

(e) Location 4 (10sec, 6times)

(f) Location 5 (10sec, 6times)

Figure 97. Surface photograph and Raman spectra of brown-colored layer on 2012 rail using 785nm laser.

Table 32. Peak locations of Raman spectra collected from brown-colored layer on 2012 rail using 785nm laser

Samples	Peak wavenumbers					
Location 1	246.8		347.9	373.7	522.5	638.8
Location 2	246.8	303.2	344.1	373.7	525.0	642.3
Location 3	246.8		344.1	373.7	522.5	642.3
Location 4	246.8	303.2		373.7	522.5	638.8
Location 5	246.8	303.2	344.1	373.7	522.5	642.3

514nm laser – 1999 rail (brown-colored layer)

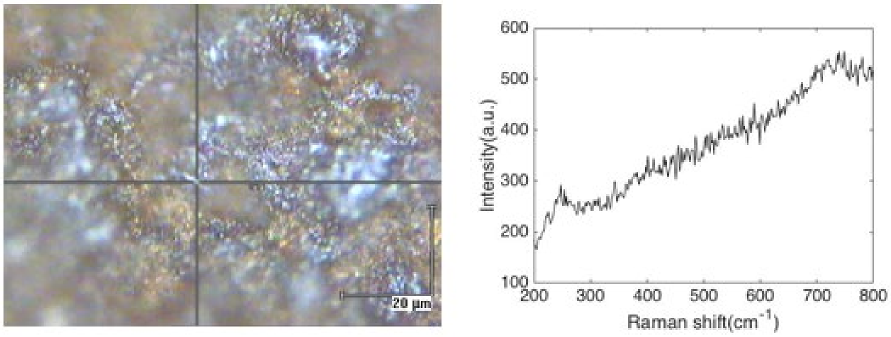

(a) Microscope image of location 1 (b) Raman spectrum of location 1

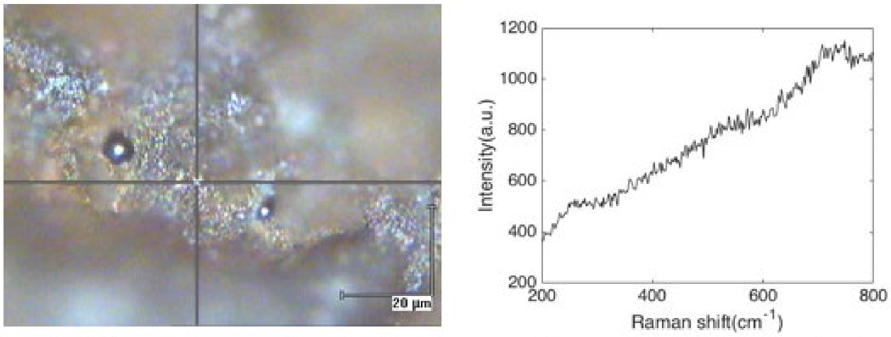

(c) Microscope image of location 2 (d) Raman spectrum of location 2

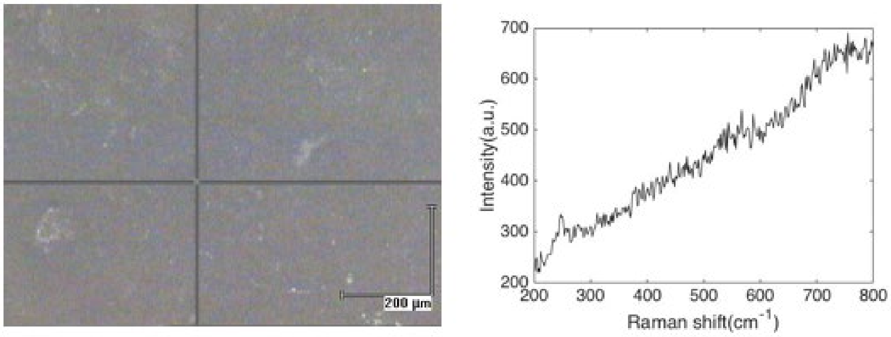

(e) Microscope image of location 3 (f) Raman spectrum of location 3

Figure 98. Microscope surface images and Raman spectra of brown-colored layer on 1999 rail using 514nm laser (1). [120sec, no averaging, x50 objective]

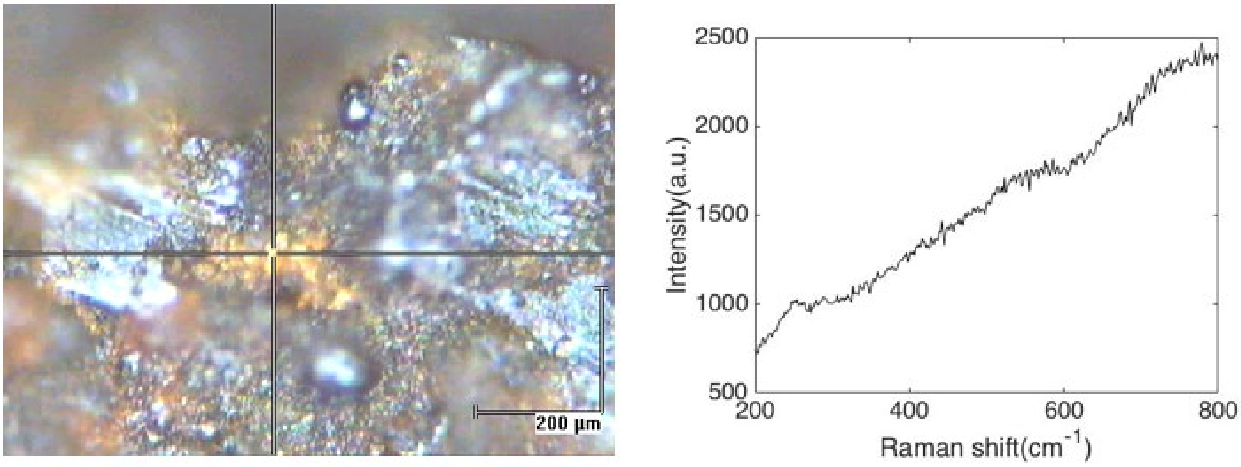

(a) Microscope image of location 4

(b) Raman spectrum of location 4

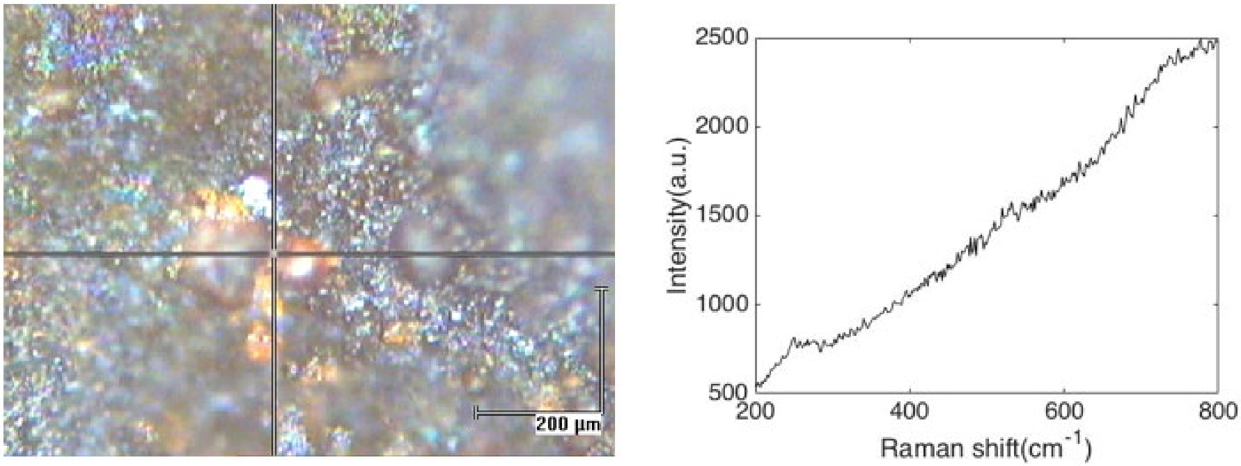

(c) Microscope image of location 5

(d) Raman spectrum of location 5

Figure 99 Microscope surface images and Raman spectra of brown-colored layer on 1999 rail using 514nm laser (2). [120sec, no averaging, x50 objective]

Table 33. Peak locations of Raman spectra collected from brown-colored layer on 1999 rail using 514nm laser

Samples	Peak wavenumbers
Location 1	247.2
Location 2	252.2
Location 3	247.2
Location 4	253.9
Location 5	250.6

785nm laser – 1999 rail (brown-colored layer)

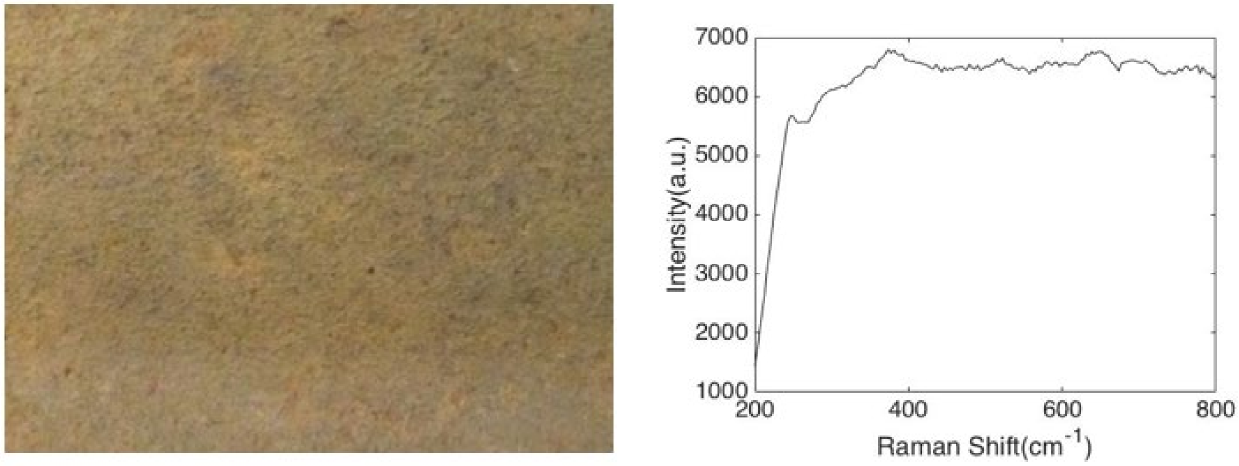

(a) Surface photograph

(b) Location 1 (10sec, 1times)

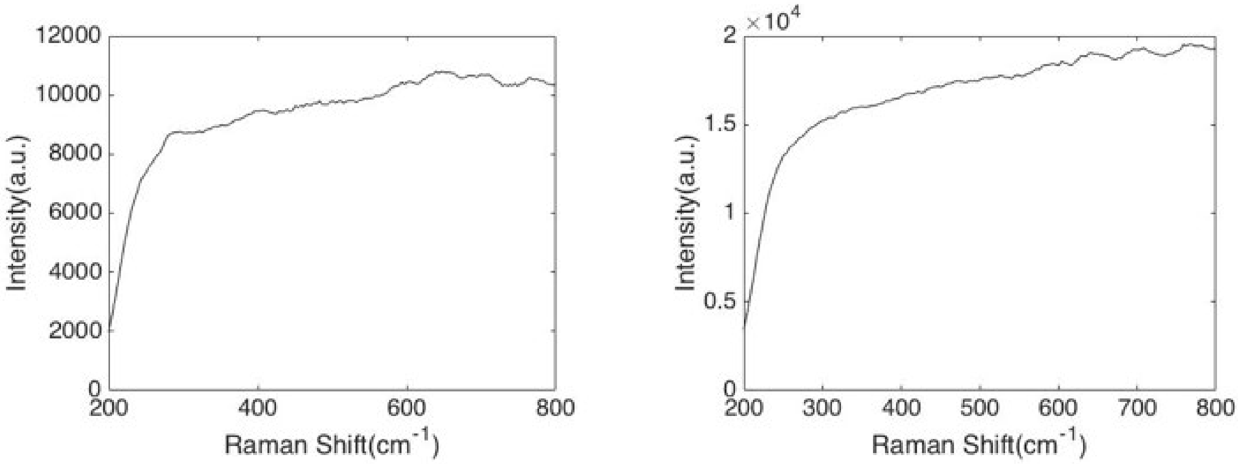

(c) Location 2 (10sec, 1times)

(d) Location 3 (10sec, 1times)

Figure 100. Surface photograph and Raman spectra of brown-colored layer on 1999 rail using 785nm laser.

Table 34. Peak locations of Raman spectra collected from brown-colored layer on 1999 rail using 785nm laser

Samples	Peak wavenumbers	
Location 1	246.8	373.7
Location 2	No peaks	
Location 3	No peaks	

514nm laser – 1948 rail (brown-colored layer)

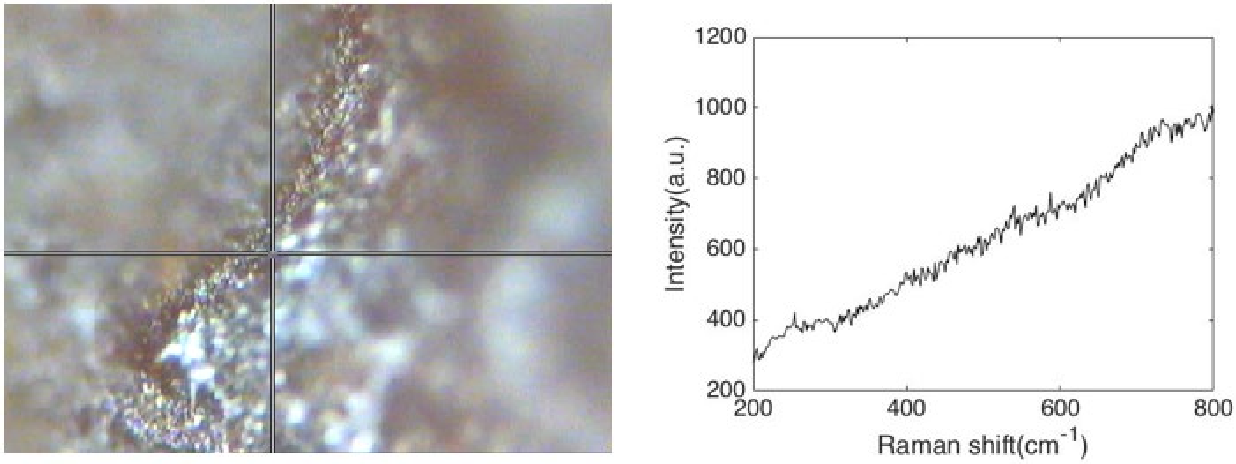

(a) Microscope image of location 1 (b) Raman spectrum of location 1

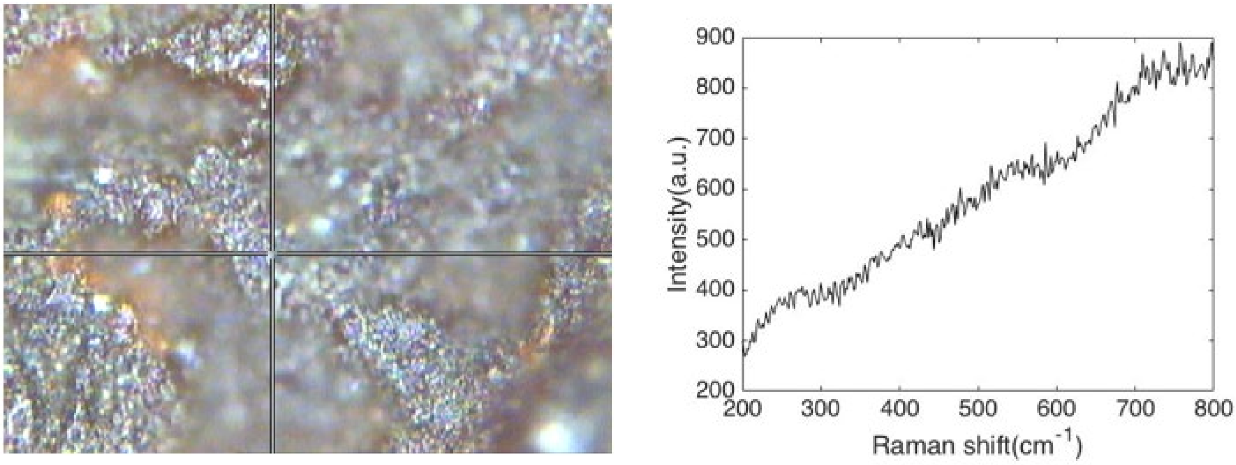

(c) Microscope image of location 2 (d) Raman spectrum of location 2

Figure 101. Microscope surface images and Raman spectra of brown-colored layer on 1948 rail using 514nm laser. [120sec, no averaging, x50 objective]

Table 35. Peak locations of Raman spectra collected from brown-colored layer on 1948 rail using 514nm laser

Samples	Peak wavenumbers
Location 1	253.9
Location 2	No peaks

785nm laser – 1948 rail (brown-colored layer)

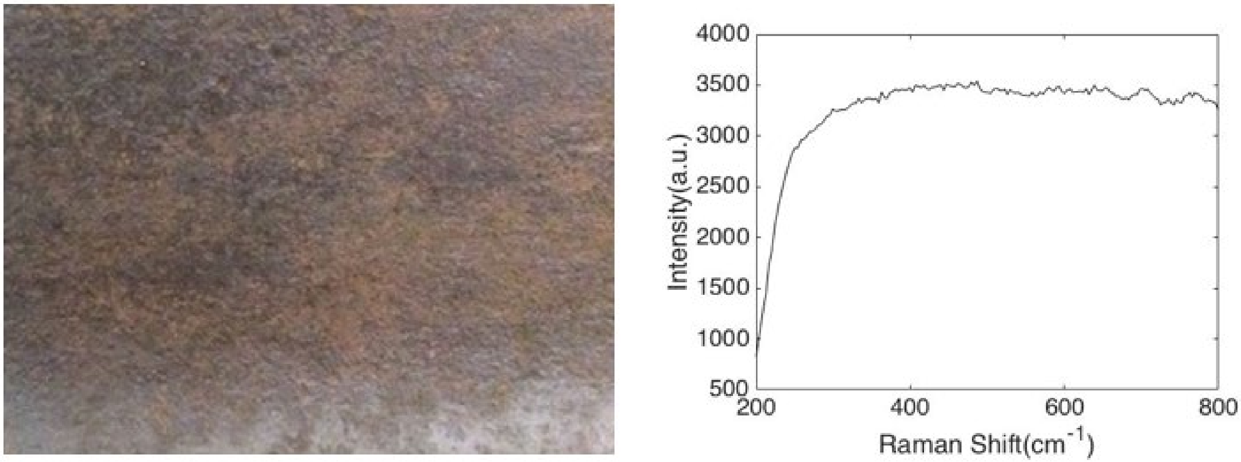

(a) Surface photograph (b) Raman spectrum (10sec, 1times)

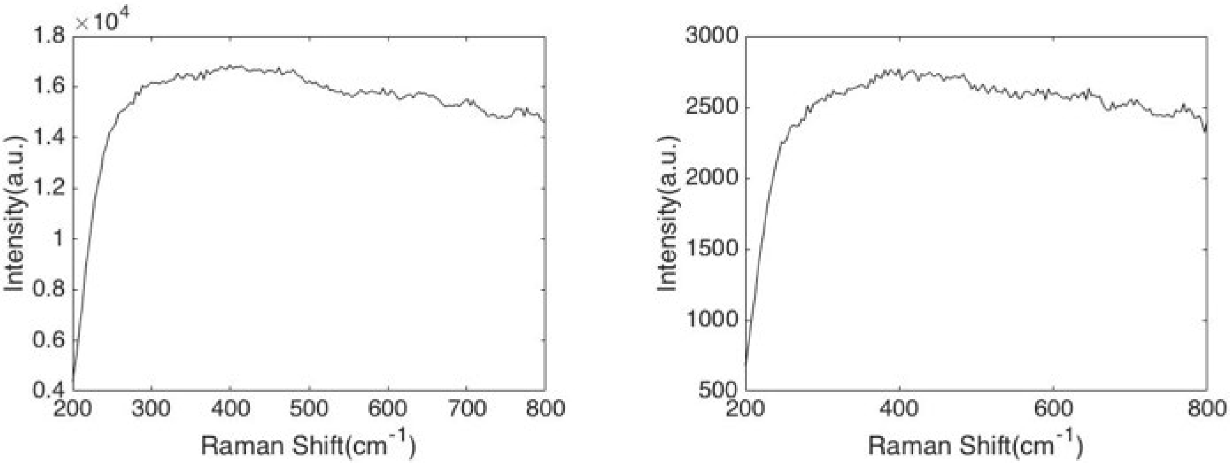

(c) Raman spectrum (10sec, 1times) (d) Raman spectrum (10sec, 1times)

Figure 102. Surface photograph and Raman spectra of brown-colored layer on 1948 rail using 785nm laser.

Table 36. Peak locations of Raman spectra collected from brown-colored layer on 1948 rail using 785nm laser

Samples	Peak wavenumbers
Location 1	No peaks
Location 2	No peaks
Location 3	No peaks

Appendix C.
Energy Dispersive X-Ray Spectroscopy (EDX or EDS)

Gray-colored layer on the 2012 Rail

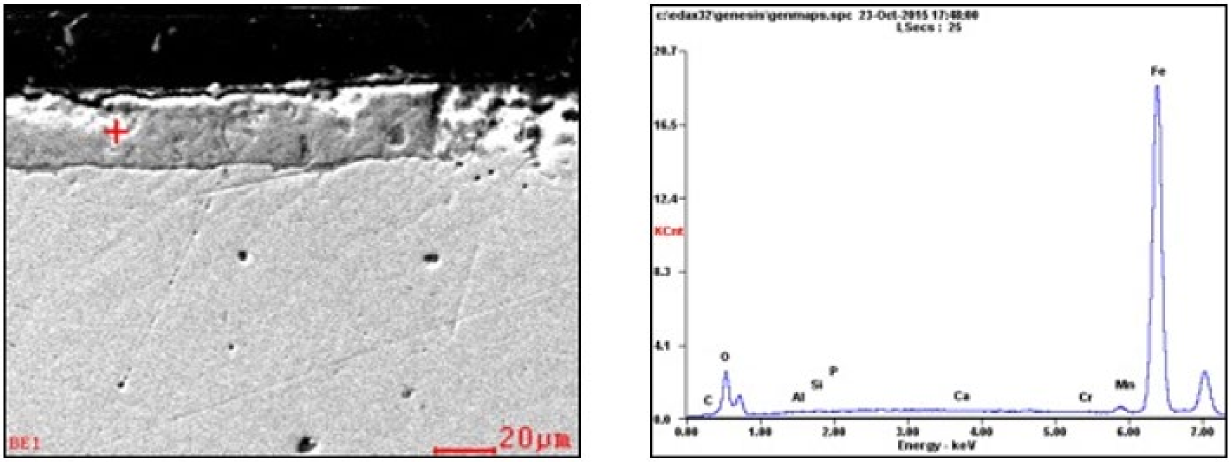

(a) SEM image of gray-colored layer (b) EDX spectrum of gray-colored layer

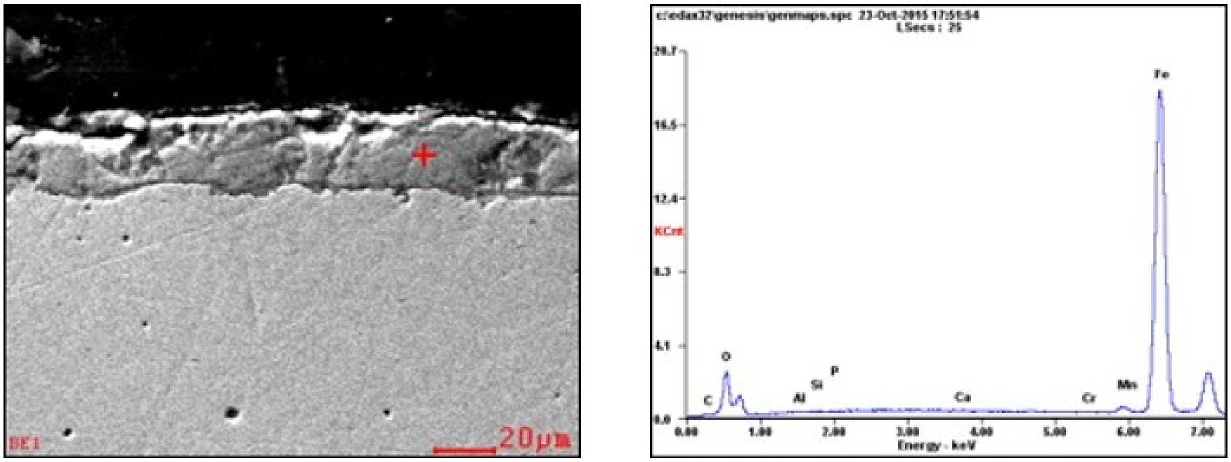

(c) SEM image of gray-colored layer (d) EDX spectrum of gray-colored layer

Figure 103. SEM images and EDX spectra for gray-colored layer on 2012 rail (1).

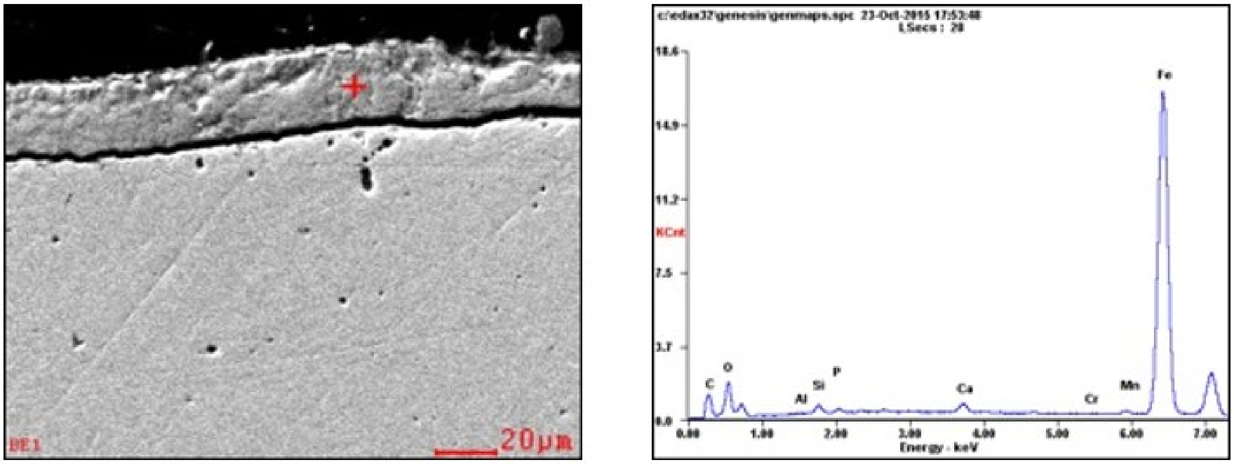

(a) SEM image of gray-colored layer (b) EDX spectrum of gray-colored layer

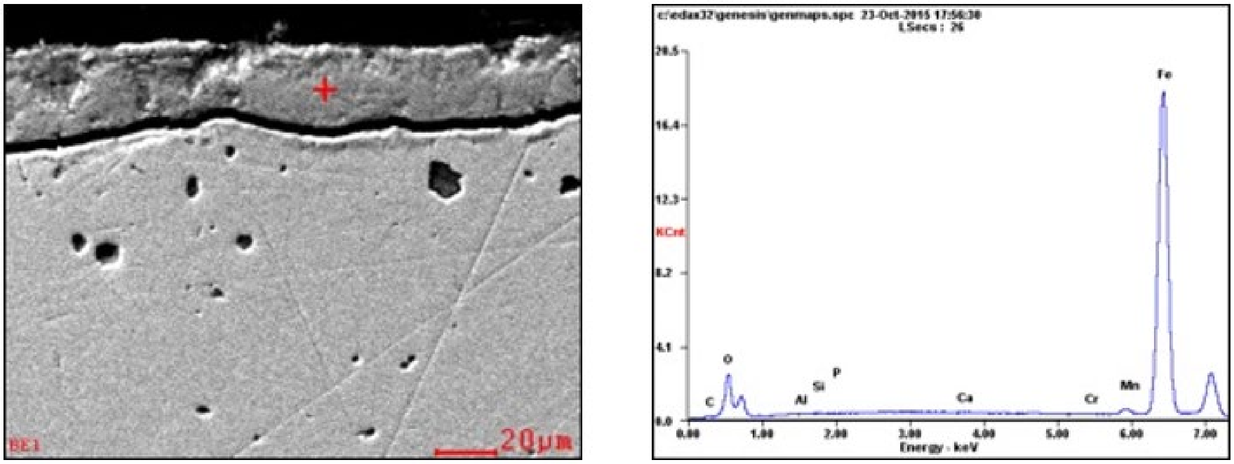

(c) SEM image of gray-colored layer (d) EDX spectrum of gray-colored layer

Figure 104. SEM images and EDX spectra for gray-colored layer on 2012 rail (2).

Table 37. Average weight and atomic percentages of gray-colored layer on 2012 rail

Element	Weight percentage (%)	Atomic percentage (%)
Fe	77.7 % (84.1 %)	50.6 %
O	14.6 % (15.9 %)	33.2 %
C	4.4 %	13.0 %

Brown-colored layer on the 2012 Rail

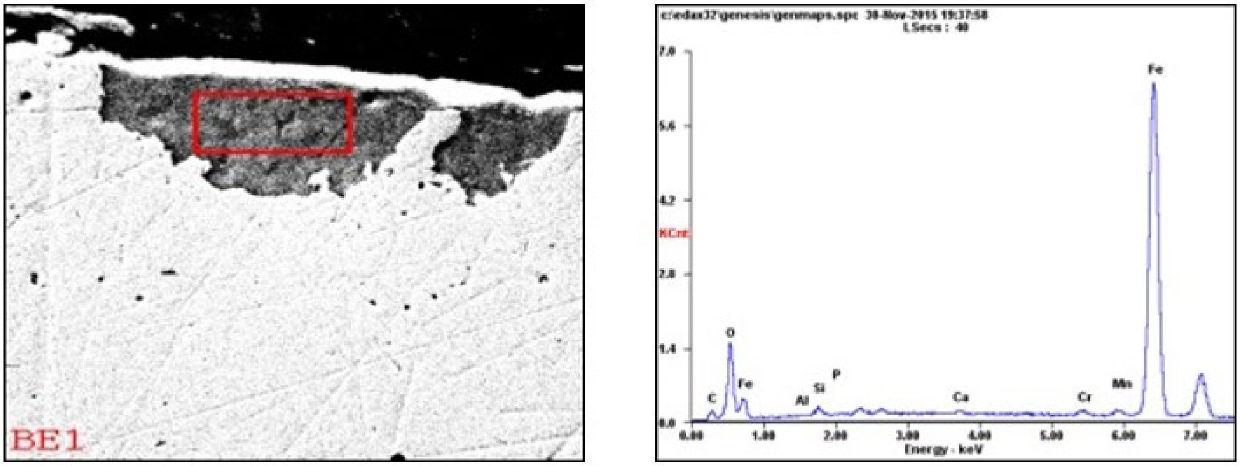

(a) SEM image of brown-colored layer (b) EDX spectrum of brown-colored layer

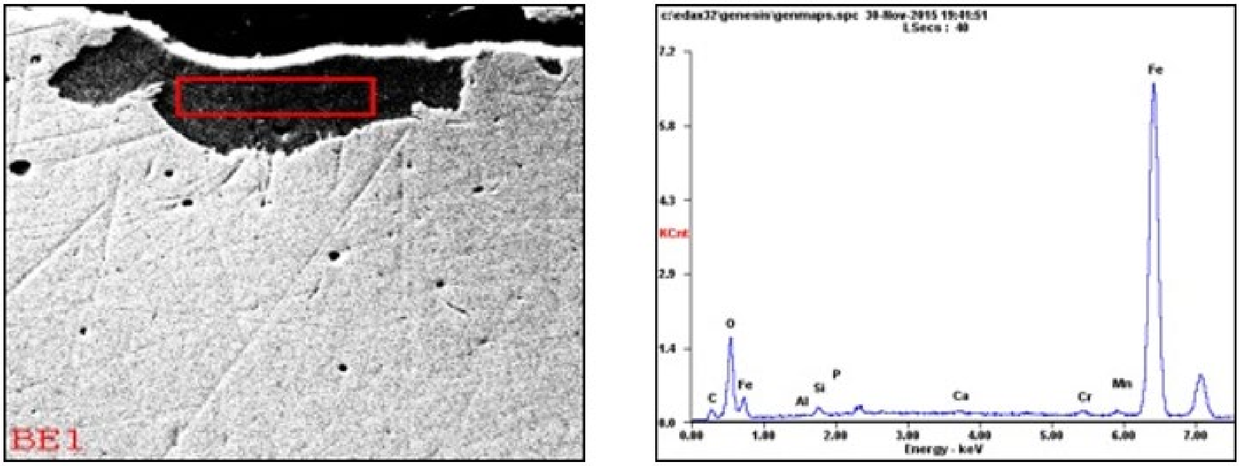

(c) SEM image of brown-colored layer (d) EDX spectrum of brown-colored layer

Figure 105. SEM images and EDX spectra for brown-colored layer on 2012 rail (1).

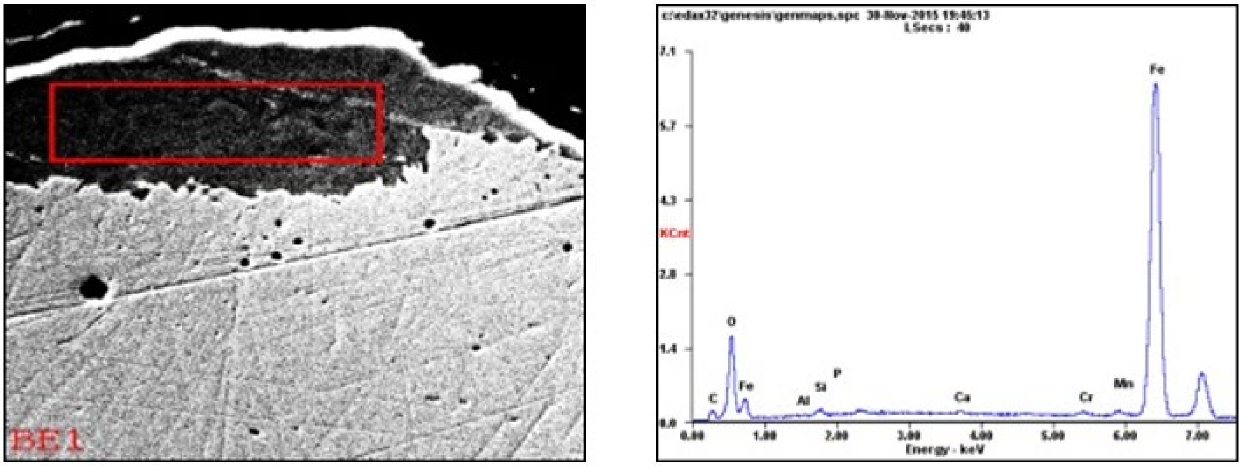

(a) SEM image of brown-colored layer (b) EDX spectrum of brown-colored layer

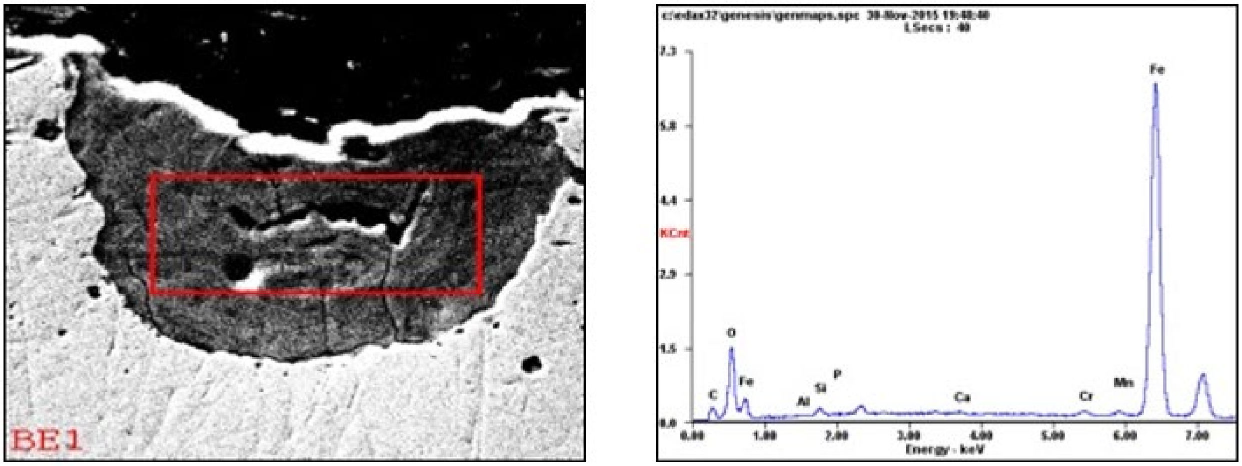

(c) SEM image of brown-colored layer (d) EDX spectrum of brown-colored layer

Figure 106. SEM images and EDX spectra for brown-colored layer on 2012 rail (2).

Table 38. Average weight and atomic percentages of brown-colored layer on 2012 rail

Element	Weight percentage(%)	Atomic percentage(%)
Fe	59.9 % (71.9 %)	28.7 %
O	23.4 % (28.1 %)	39.1 %
C	13.3 %	29.6 %

Brown-colored layer on the 1999 Rail

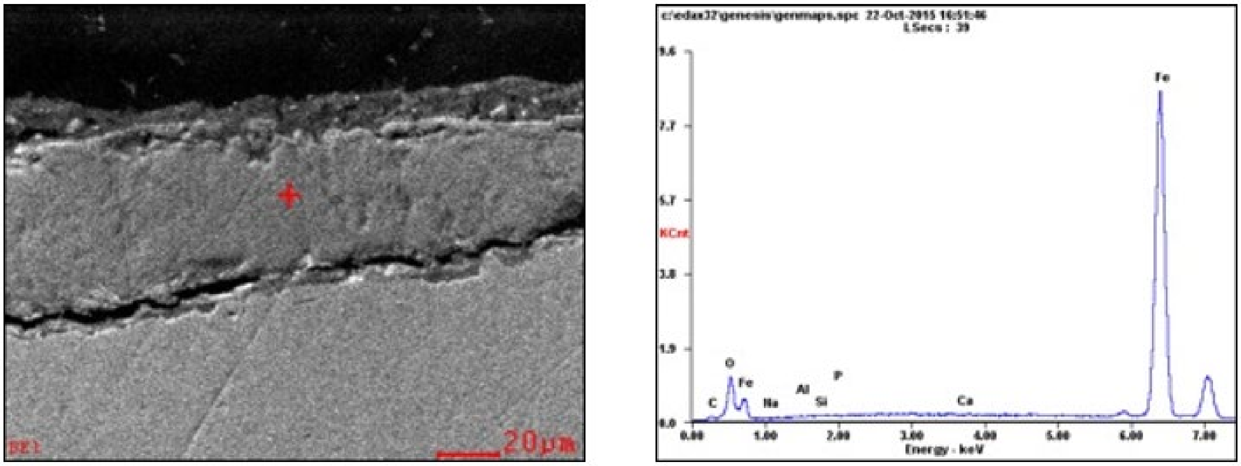

(a) SEM image of brown-colored layer

(b) EDX spectrum of brown-colored layer

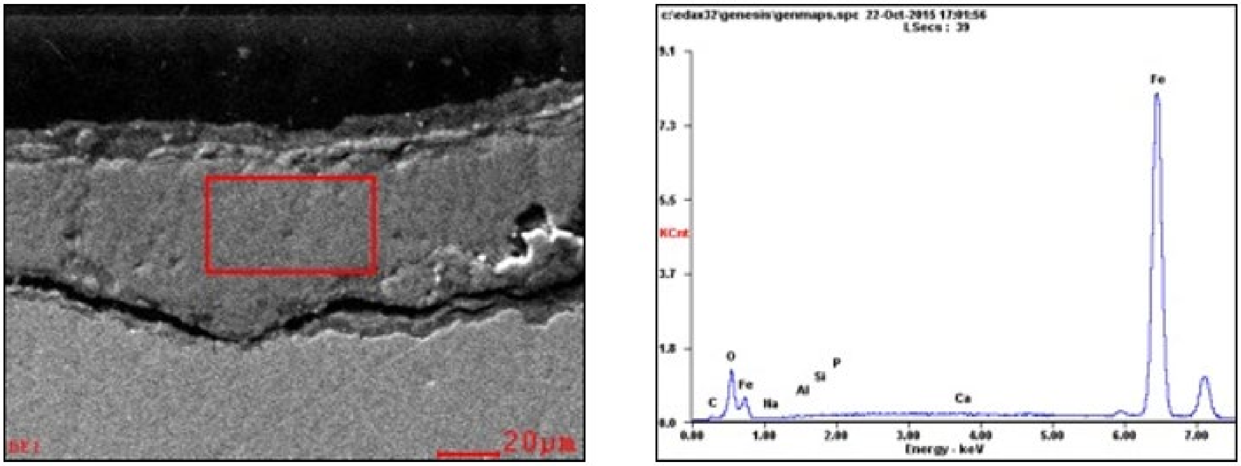

(c) SEM image of brown-colored layer

(d) EDX spectrum of brown-colored layer

Figure 107. SEM images and EDX spectra for brown-colored layer on 1999 rail (1).

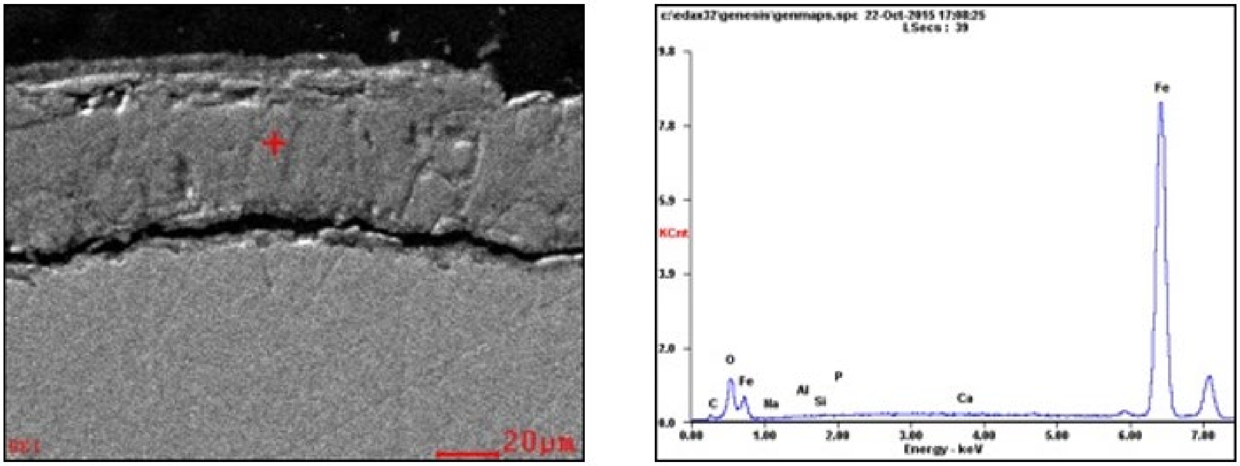

(a) SEM image of brown-colored layer

(b) EDX spectrum of brown-colored layer

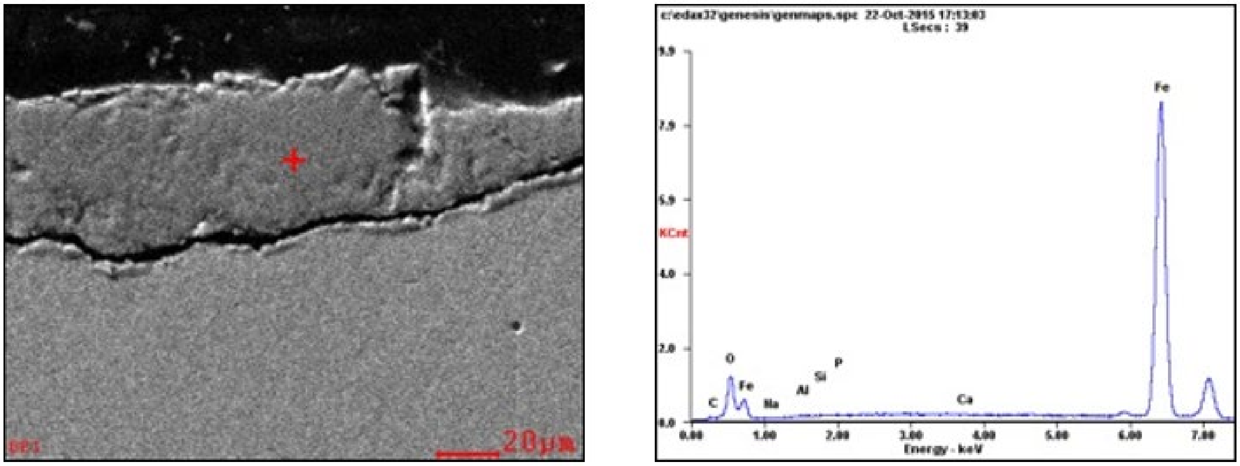

(c) SEM image of brown-colored layer

(d) EDX spectrum of brown-colored layer

Figure 108. SEM images and EDX spectra for brown-colored layer on 1999 rail (2).

Table 39. Average weight and atomic percentages of brown-colored layer on 1999 rail

Element	Weight percentage (%)	Atomic percentage (%)
Fe	78.2 % (84.1 %)	49.4 %
O	14.8 % (15.9 %)	32.7 %
C	5.41 %	15.9 %

Brown-colored layer on the 1948 Rail

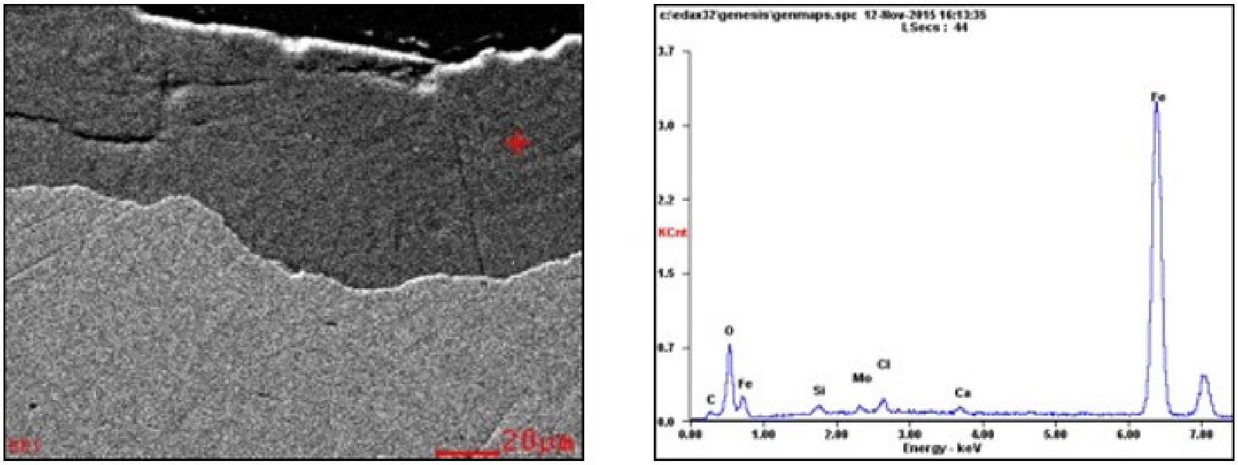

(a) SEM image of brown-colored layer (b) EDX spectrum of brown-colored layer

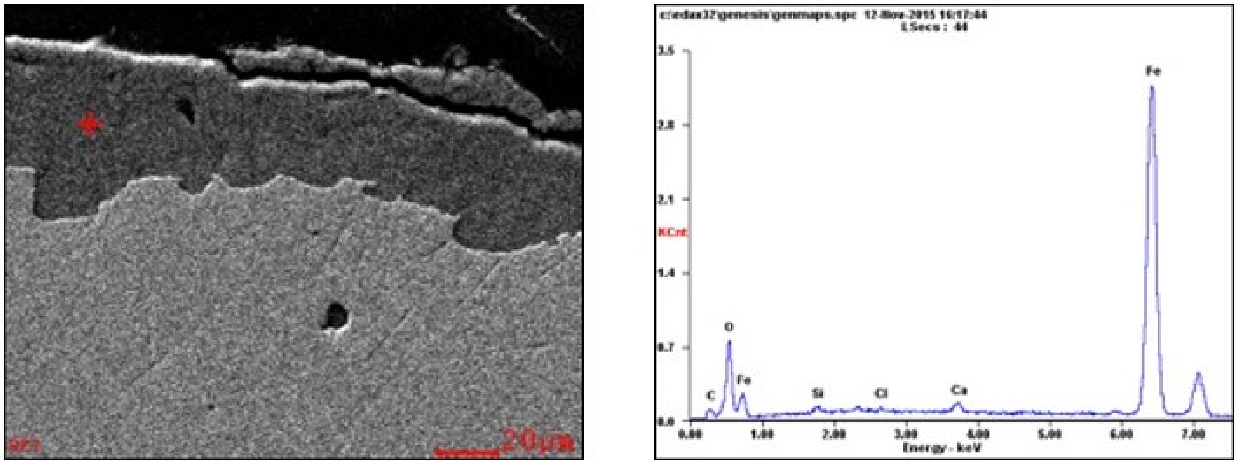

(c) SEM image of brown-colored layer (d) EDX spectrum of brown-colored layer

Figure 109. SEM images and EDX spectra for brown-colored layer on 1948 rail (1).

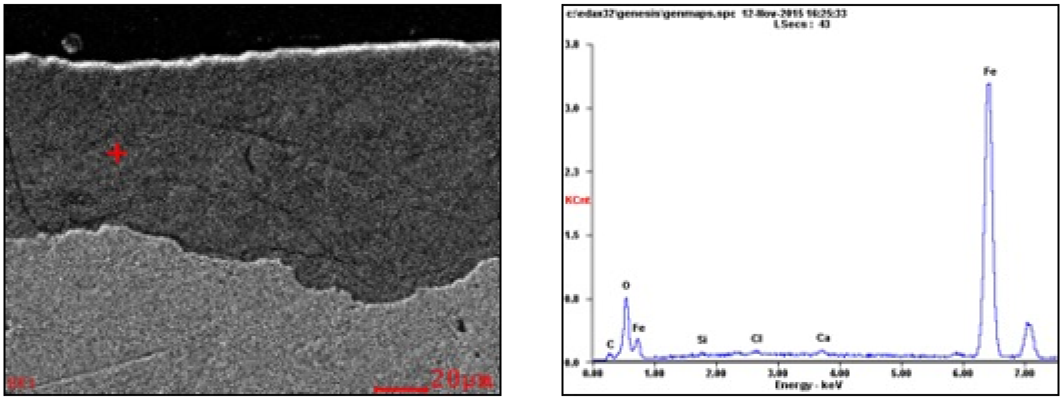

(a) SEM image of brown-colored layer (b) EDX spectrum of brown-colored layer

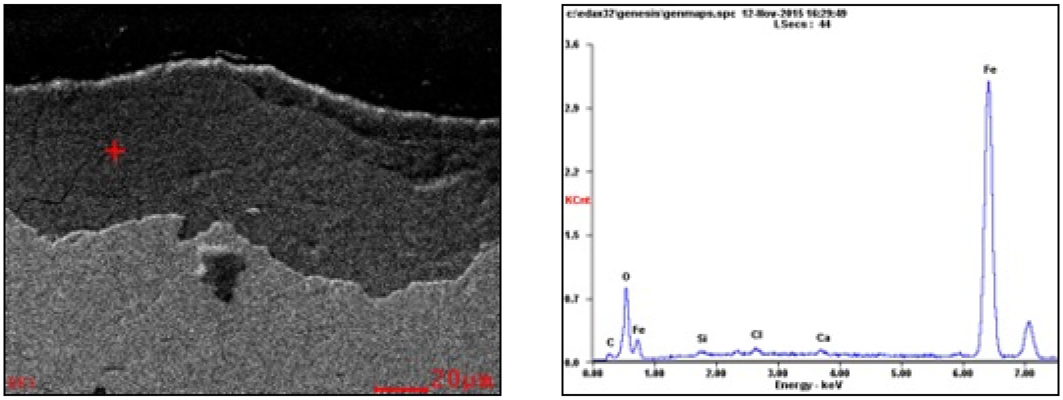

(c) SEM image of brown-colored layer (d) EDX spectrum of brown-colored layer

Figure 110. SEM images and EDX spectra for brown-colored layer on 1948 rail (2).

Table 40. Average weight and atomic percentages of brown-colored layer on 1948 rail.

Element	Weight percentage(%)	Atomic percentage(%)
Fe	63.7 % (73.7 %)	32.4 %
O	22.8 % (26.3 %)	40.4 %
C	10.5 %	24.8 %

Abbreviations and Acronyms

ACRONYM	DEFINITION
CWR	Continuous Welded Rail
EDX	Energy-Dispersive X-ray spectroscopy
FPS	Fluorescence Piezo Spectroscopy
HAZ	Heat Affected Zone
PSC	Piezo-Spectroscopic Coefficient
RPS	Raman Piezo Spectroscopy
SEM	Scanning Electron Microscopy
XRD	X-Ray Diffraction spectroscopy